THE UNIVERSITY OF CHICAGO

MINERAL PHYSICS OF HYDROGEN-BEARING PHASES IN THE DEEP EARTH

A DISSERTATION SUBMITTED TO
THE FACULTY OF THE DIVISION OF THE PHYSICAL SCIENCES
IN CANDIDACY FOR THE DEGREE OF
DOCTOR OF PHILOSOPHY

DEPARTMENT OF THE GEOPHYSICAL SCIENCES

BY
ELIZABETH COLETTE THOMPSON

CHICAGO, ILLINOIS
MARCH 2018

ACKNOWLEDGMENTS

I would like to thank my committee members for their support, insight, and assistance in producing this dissertation: Andrew J. Campbell (the University of Chicago), Dion L. Heinz (the University of Chicago), Frank M. Richter (the University of Chicago), Nicolas Dauphas (the University of Chicago), and Jun Tsuchiya (Ehime University). I would also like to acknowledge the faculty, graduate students, and staff in the Department of the Geophysical Sciences. Special thanks are owed to my family for their support over the years. Last but not least, I must thank my husband, José Iriarte-Diaz, for his patience and sass in equal measure.

TABLE OF CONTENTS

LIST OF FIGURES

LIST OF TABLES

ABSTRACT

Water (OH^-) within the Earth's interior is known to influences a wide range of processes inside the Earth including melting temperatures (e.g., Inoue 1994), rheology (Karato et al., 1986), electrical conductivity (Wang et al., 1991), atomic diffusivity (Karato, 1990) and trace element partitioning during partial melting (e.g., Tiepolo et al. 2000). Yet there remains a substantial gap in our understanding of which mantle phases host water (OH^-) and what the geophysical properties of these phases are. Refining our understanding of which phases host water is a critical step in determining the hydrogen carrying capacity of the Earth's mantle, while determining the geophysical properties of these phases (e.g. density and sound velocities) provides important parameters that allow geophysicists and geodynamicists to constrain the distribution of these phases in the Earth.

This thesis traces a potential path of hydrogen transport through the Earth's lower mantle to the outer core. Specifically, I explore the stability and properties of hydrous lower mantle phases including Al-bearing phase D [$(Mg,Al)(Si,Al)_2O_4(OH)_2$], ε-FeOOH, and pyrite type $(Al,Fe)O_2H$, as well as potential core constituent phase *fcc* FeH_X. While stable at the pressure-temperature (P-T) conditions of a subducting slab in the Earth's uppermost lower mantle (i.e., approximately 660-1200 km depth), at more extreme P-T conditions phase D transforms into phase H [$MgSiO_2(OH)_2$], which forms a solid solution with ε-FeOOH and δ-AlOOH (Nishi et al., 2014). At even higher pressures (>60 and >190, respectively), ε-FeOOH and δ-AlOOH transform to a pyrite structure, with intermediate solid solution compositions [$(Al,Fe)O_2H$] potentially stable at core-mantle boundary conditions (Nishi et al., 2017; Tsuchiya and Tsuchiya, 2011). The high-pressure, high-temperature reaction of hydrous phases and iron have been shown to result in the formation of iron hydrides (Yagi and Hishinuma, 1995), a means by which hydrogen may be incorporated into the Earth's outer core. This thesis concludes by investigating the geophysical properties of *fcc* FeH_X, concluding the subduction path of our hypothetical parcel of hydrogen-bearing material. In addition to probing the properties of idealized endmember compositions, this

research aims to probe the influence of solid-solutions on the stability and properties of the hydrous deep Earth phases, allowing a more realistic assessment of hydrogen accommodation in the Earth's interior.

CHAPTER 1

HYDROGEN IN THE DEEP EARTH

We recognize the importance of water in the biosphere, but what role does water play in the deep Earth? Forty years of scientific literature on the topic has produced wildly variable estimates of the water content within the deep Earth, with values ranging from a quarter to four times the volume of water found in the Earth's oceans (Ringwood, 1975; Ahrens, 1989; Jambon and Zimmerman, 1990; Bolfan-Casanova et al., 2003; Hirschmann, 2006; Hirschmann and Kohlstedt, 2012). This water, however much there is, influences a wide range of processes inside the Earth. Water (OH^-) within the crystalline structure of deep Earth minerals impacts melting temperatures (Lambert and Wyllie, 1968; Mysen and Boettcher, 1975; Inoue, 1994), rheology (Karato et al., 1986), electrical conductivity (Wang et al., 1991), atomic diffusivity (Karato, 1990) and trace element partitioning during partial melting (Adam et al., 1993; Ionov and Hofmann, 1995; LaTourrette et al., 1995; Tiepolo et al., 2000). Additionally, the dehydration of hydrous minerals in subducting plates influences macro-scale phenomena; controlling the production of island arc magmatism (Tatsumi et al., 1986; Kushiro, 1987; Ulmer, 2001) and influencing subduction zone seismicity to depths up to ∼700 km (Omori et al., 2004). Yet despite water's obvious importance, the quantity, distribution, and accommodation of hydrogen in the deep Earth remains largely unknown.

The idea of a truly global water cycle, an intrinsic connection between Earth's internal water cycle and the water cycle of the hydrosphere, is supported by the relative stability of ocean levels over the past 600 million years (Smyth, 2006; McGovern and Schubert, 1989; Rüpke et al., 2004). If hydrous oceanic plates subducted without water being recycled back to Earth's surface, Earth's oceans would have been drained within 1 to 2 billion years (Ito et al. 1983). Yet this is far from evidence Earth's oceans are a surficial hydrous layer enveloping a desiccated inner planet. Evidence of a wet inner Earth exists in the form of hydrous phases found in mantle xenoliths and peridotite massifs (e.g., Frost 2006). The interconnectedness of these water reservoirs is bolstered by recent seismology, geochemistry

and mineral physics findings. Seismic tomography shows that subducting lithospheric slabs can pierce the transition zone, potentially ushering hydrous phases through the transition zone and into the lower mantle (van der Hilst et al., 1997; Davies, 1995). An ocean plate subducting at the rate of 150 mm per year could pierce the 660 km discontinuity in roughly 5 my (Stern, 2002). The partial dehydration of subducting plates influences the D/H ratio of Earth's inner water reservoirs, acting as a forensic tracer of recycled plate material and geochemically linking D-depleted ocean island basalts to the lower mantle (Shaw et al., 2008). Lastly, mineral physicists have identified several potential mechanisms for water storage inside the Earth, including both nominally anhydrous and hydrous phases, a few of which may persist along a cold-slab geotherm to pressure and temperature conditions of the lower mantle.

Oceanic plates contain hydrous phases including serpentine and amphibole. As these plates subduct and sink along the cold slab geotherm through the upper mantle, these hydrous minerals are exposed to higher pressures and temperatures and decompose into a series of dense hydrous magnesium silicates (DHMSs). These DHMSs have been shown to sequentially decompose from phase A, to phase B or superhydrous phase B, eventually forming a DHMS known as phase D [$MgSi_2O_4(OH)_2$] (Yang et al., 1997). Phase D contains $\sim$10 wt% H_2O, orders of magnitude above the parts per million found in nominally anhydrous minerals. Due to its reported stability up to $\sim$45 GPa (Shieh et al., 1998), phase D has been considered the leading contender for ushering water through the transition zone and into the upper portion of the lower mantle (Komabayashi and Omori, 2006). Recent studies indicate aluminum substitution into DHMSs increases the thermodynamic stability of these phases (Sano et al., 2008; Ohira et al., 2014; Pamato et al., 2015). Additionally, the near Al-endmember of phase D, referred to as 'super-aluminous phase D' may host more water than its magnesium counterpart (e.g., Boffa Ballaran et al. 2003). Chapter 2 of this thesis examines the influence that aluminum substitution has on the structure, equation of state, and elasticity of phase D.

Recently a computational study by Tsuchiya (2013) predicted the phase transition of phase D into a new higher-pressure DHMS at the pressures of the lower mantle. This phase has the highest reported P-T stability of any of the so-called 'alphabet' phases of dense hydrous magnesium silicates. Shortly after the publication of this *ab initio* prediction, Nishi et al. (2014) used powder X-ray diffraction to confirm the decomposition of phase D into a newly identified hydrous phase dubbed 'phase H' [$MgSiO_2(OH)_2$]. Soon after, Bindi et al. (2014) used single crystal diffraction to refine the structure of phase H, which they identified as forming in the rutile structure, in the *Pnnm* space group. Their findings suggest that phase H could form a solid solution with the hydrous high-pressure phase δ-AlOOH, which undergoes a symmetry transition from $P2_1nm$ to *Pnnm* when pressure exceeds ∼9 GPa (Tsuchiya et al., 2002; Sano-Furukawa et al., 2009; Kuribayashi et al., 2014). As δ-AlOOH has a pressure-temperature (P-T) stability that extends to the Earth's core-mantle boundary (CMB) (Sano et al., 2008), it is probable that Al-substitution in phase H would stabilize the structure to increased P-T conditions analogous to the influence of Al-substitution on the stability of phase D.

At ambient pressure goethite (α-FeOOH) is isomorphous with the low-pressure aluminum oxide hydroxide diaspore (α-AlOOH). As with diaspore, goethite undergoes a pressure induced phase change, transforming into the high-pressure phase ε-FeOOH, which is isostructural with high-pressure δ-AlOOH (Suzuki, 2010). Both ε-FeOOH and δ-AlOOH are reported to undergo second-order phase transitions due to hydrogen bond symmetrization (Gleason et al., 2013; Kuribayashi et al., 2014), and it is presumable that the post-hydrogen bond symmeterized structures of these compositions form a solid solution. As phase H also belongs to the *Pnnm* space group (Bindi et al., 2014), there likely exists a solid solution between phase H, δ-AlOOH, and ε-FeOOH. Although the influence of Al-substitution on phase H has been explored to some degree, the influence of iron on this system remains poorly understood. The third chapter of this thesis describes the elasticity, sound velocities, and seismic anisotropy of low-spin hydrogen-symmetric ε-FeOOH, comparing these results to the elasticities of δ-

AlOOH and phase H, in order to determine the influence of iron substitution on the material properties of this hydrogen-bearing lower mantle solid solution. This chapter reproduces, in part, material previously published as Thompson et al. (2017).

In addition to the previously described $P2_1nm \rightarrow Pnnm$ transition, ε-FeOOH is also reported to undergo a high spin (HS) to low spin (LS) transition, determined on the basis of X-ray diffraction (XRD) and X-raw emission spectroscopy (XES) experiments (Gleason et al., 2008). The XES results from this earlier study indicate initiation of the spin transition at ∼40 GPa and its completion at ∼60 GPa. Using XRD, the authors determined a coincident volume collapse (11%) at ∼54 GPa, which they attribute to hydrogen bond symmetrization occurring coincident to the spin transition. Yet, previous studies have reported similar volume reductions due to HS → LS transitions without invoking hydrogen bond symmetrization (Speziale et al., 2005; Lin et al., 2005a). In this Chapter 4 of this thesis I present experimental findings indicative of two independent transitions in ε-FeOOH in the explored pressure range (∼0-70 GPa): a lower pressure (17.5±1) structural transition, possibly connected to hydrogen bond symmetrization, and a higher pressure electronic transition.

It has recently been discovered that at sufficiently high pressure (>60 GPa), α-FeOOH transforms into a cubic, pyrite structure but the stability of this newly identified phase remains contested (Nishi et al., 2017; Hu et al., 2016, 2017). In the literature this phase is referred to as pyrite-type FeO_2H, as unlike lower pressure FeO(OH) polymorphs this structure exists only in a symmetric hydrogen bond structure, in which there are not distinct hydroxyl units. While some studies suggest FeO_2H dehydrates in the Earth's mantle (Hu et al., 2016, 2017), a more recent experiment suggests FeO_2H persists to the core-mantle boundary (Nishi et al., 2017), where its reaction with the Earth's core could produce iron hydride. Additionally, the stability of FeO_2H may be enhanced by the formation of a solid solution with pyrite-type AlO_2H, as δ-AlOOH undergoes an analogous phase transition to pyrite-type AlO_2H, albeit at a higher pressure (>130 GPa) (Tsuchiya and Tsuchiya, 2011).

In Chapter 5 of this thesis I report on the structure, equation of state, and elastic properties of pyrite-type FeO_2H using density functional theory calculations—properties I then compare to the previously reported characteristics of pyrite-type AlO_2H.

The Earth's liquid outer core is roughly 2,300 kilometers thick, approximately equal to the distance between Chicago, IL and Phoenix, AZ. Yet although the inner and outer cores contain 30 % of Earth's mass, the composition of these regions of the interior remain uncertain. It is accepted by the scientific community that the Earth's cores are predominantly iron-nickel alloy, but with one or more lighter elements needed to compensate for the fact that the outer core is ∼10% less dense (Birch, 1952) and with a bulk modulus ∼12% lower (Jeanloz, 1979) than pure iron under appropriate P-T conditions. The solid inner core is composed of iron with the presumed inclusion of light elements to compensate for the 2-5% density difference between seismically obtained densities and experimental densities for pure Fe at relevant P-T conditions. Several potential light elements have been proposed to account for these differences, such as silicon, carbon, oxygen, sulfur, and hydrogen, many of which depleted in the Earth's crust relative to cosmochemical abundances (Poirier, 1994; Stevenson, 1981).

Water within the upper- and likely lower-mantle is likely part of the larger water cycle driven by plate tectonics, but does hydrogen also reside in Earth's core? Might hydrogen contribute to the light element budget of the inner core, and if so, does that influence prevailing opinions concerning Earth's origin? Understanding the behavior of volatile elements such as hydrogen during accretion and differentiation is the first step to evaluating the subsequent evolution of volatile cycles in the terrestrial planets (e.g., Chi et al. 2014). Hydrogen, the most abundant and lightest element in the solar system, is often overlooked as a viable contributor to the Earth's core density deficit because of its volatile nature and low solubility in iron at atmospheric conditions. Yet recent work suggests the solubility of hydrogen into iron rapidly increases as pressures approach those of the core-mantle boundary (Fukai et al., 2003). Additionally, nearly stoichiometric iron hydride (FeH_X, X∼1) has been shown

to result from either the reaction of Fe and hydrous silicates (Yagi and Hishinuma, 1995) or the reaction of Fe and water at lower mantle conditions (Ohtani et al., 2005). Chapter 6 of this dissertation focuses on evaluating the the geophysical properties of face-centered cubic (*fcc*) FeH_X in order to constrain the degree to which hydrogen contributes to the observed density deficit, and sound velocities, of the Earth's core. This chapter reproduces, in part, material previously published as Thompson et al. (2018).

Lastly, this dissertation excludes some work that although completed during my tenure as a PhD candidate in this department, is thematically distant to the primary research thrust put forth here (Thompson et al., 2016a,b).

CHAPTER 2

CALCULATED ELASTICITY OF Al-BEARING PHASE D

2.1 Introduction

Mineral physics experiments and *first principles* calculations have identified several mechanisms for water storage inside the Earth, including both nominally anhydrous and hydrous phases, but few of these phases are stable at the extreme pressure and temperature conditions of the Earth's lower mantle. As serpentine-bearing lithospheric plates subduct, serpentine decomposes into a series of dense hydrous magnesium silicates (DHMSs) that contain wt.% quantities of water (OH^-) and are important carriers of water in subduction zones (Kanzaki, 1991; Ohtani et al., 2001; Poli and Schmidt, 2002; Iwamori, 2004). Of the known DHMSs, Phase D has the second highest pressure-temperature (P-T) stability, rendering phase D capable of ushering hydrogen through the transition zone and into the lower mantle (e.g., Shieh et al. 1998).

Recent studies indicate that aluminum substitution into DHMSs increases the thermodynamic stability of these phases (Sano et al., 2008; Ohira et al., 2014; Pamato et al., 2015), and may host more water than its magnesium counterpart (Boffa Ballaran et al., 2003). Additionally, Al-bearing phase D [$(Mg,Al)(Si,Al)_2O_4(OH)_2$] is a likely precursor to the solid solution formed by phase H and δ-AlOOH—a solid solution with P-T stability that extends to the core-mantle boundary. Owing to the important role that Al-bearing phase D may play in the storage and cycling of hydrogen in the Earth's lower mantle, this study evaluates the influence of Al-substitution on the structure, equation of state, and elasticity of phase D using *first principles* calculations.

Magnesium endmember phase D [$MgSi_2O_4(OH)_2$] has trigonal symmetry and is in the $P\bar{3}1m$ space group (Yang et al., 1997). The rutile-like crystal structure contains alternating layers of SiO_6 and MgO_6 octahedra stacked along the c-axis, with hydroxyl bonds connecting neighboring octahedra in the magnesium layer (Figure 2.1a). Aluminum substitutes into

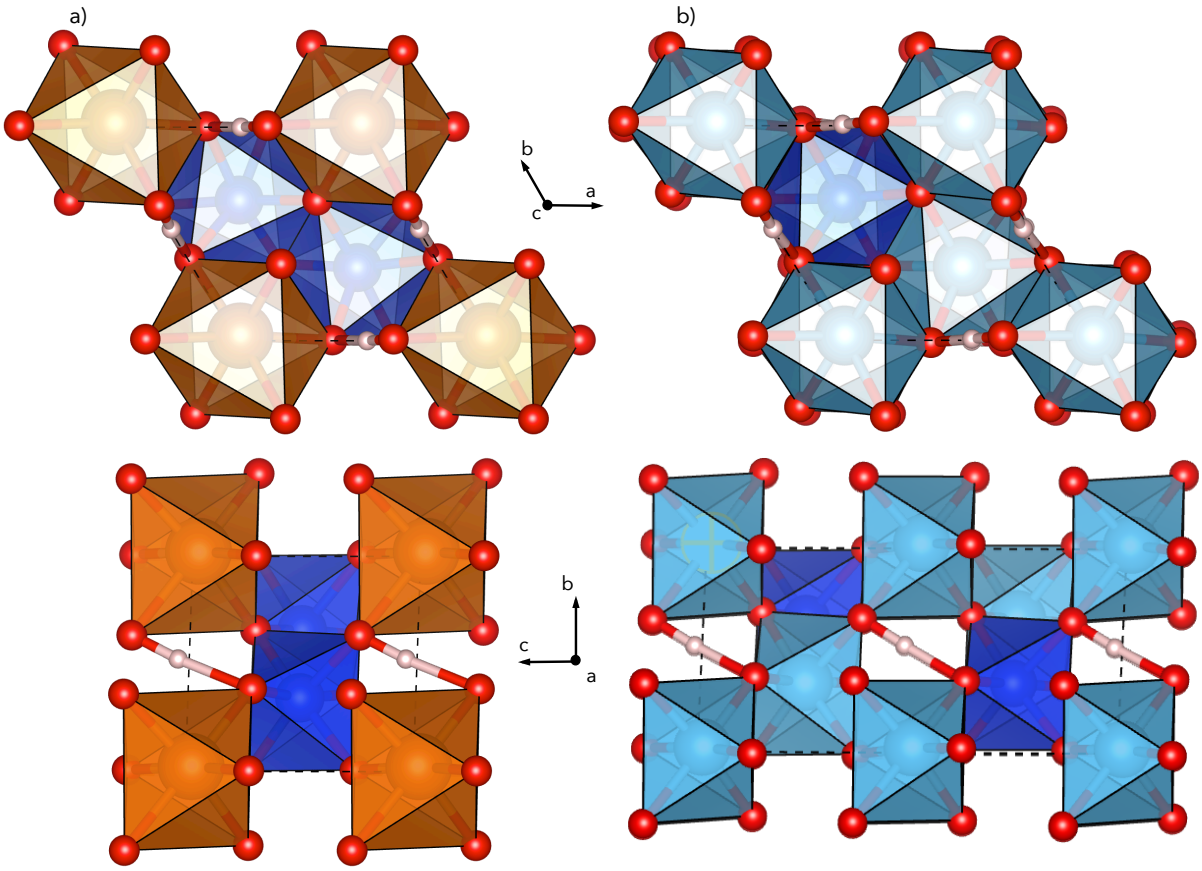

Figure 2.1: Crystal structures of phase D at 0 GPa including (a) the Mg-endmember [$MgSi_2O_4(OH)_2$] (one formula unit) and (b) disordered Al-end-member [$Al_2SiO_4(OH)_2$] (two formula units). Images were generated in VESTA (Momma and Izumi, 2008). Aluminum atoms are aqua spheres, magnesium atoms are orange spheres, silicon atoms are dark blue spheres, oxygen are red spheres, and hydrogen are white spheres.

.

phase D via a Tschermak $Si^{4+} + Mg^{2+} \longleftrightarrow 2Al^{3+}$ substitution, and experiments report a range of compositions, including the near Al-endmember composition referred to as 'super-aluminous' phase D (Boffa Ballaran et al., 2003). Based on single crystal X-ray diffraction structure refinement, this near Al-endmember phase D is also in the $P\bar{3}1m$ space group, with a high degree of Si/Al disordering and decreased octahedral distortion relative to the Mg-endmember (Boffa Ballaran et al., 2003) (Figure 2.1b).

Mg-endmember member phase D undergoes a pressure-induced hydrogen bond sym-

metrization at ∼40 GPa, established on the basis of both *first principles* calculations (Tsuchiya et al., 2005) and subsequent high-pressure X-ray diffraction experiments (Hushur et al., 2011). Hydrogen-bond symmetrization is the phenomenon in which the hydroxyl bonds (O–H) in a material evolve with increased pressure such that they become equal in length to the hydrogen bonds (O···H). Hydrogen-bond symmetrization in the Mg-endmember profoundly impacts its compressibility, increasing the bulk modulus by up to 20% (e.g., Tsuchiya et al. 2005). However, as hydrogen bond symmetrization has yet to be reported in Al-bearing phase D, it is important to probe the influence of Al-substitution on this phenomenon. Using *first principles* calculations, this study evaluates three compositions of phase D: (1) the magnesium endmember [$MgSi_2O_4(OH)_2$], (2) the aluminum endmember [$Al_2SiO_4(OH)_2$], and phase D with 50% Al-substitution [$AlMg_{0.5}Si_{1.5}O_4(OH)_2$], in order to evaluate the influence of Al-substitution on the structure, equation of state, and elasticity of phase D.

2.2 Methods

Density functional theory (DFT) based calculations were used to evaluate the structure and elasticity of three compositions [$MgSi_2O_4(OH)_2$, $AlMg_{0.5}Si_{1.5}O_4(OH)_2$, $Al_2SiO_4(OH)_2$] of phase D as a function of pressure from 0 to 75 GPa. Although previous studies have calculated the structure and elasticity of Mg-endmember phase D (Mainprice et al., 2007; Tsuchiya et al., 2008), these calculations were repeated to enable direct comparison between phase D compositions using the same pseudopotentials for all calculations. Al-endmember composition values reported herein are based on evaluations using a 2-unit cell supercell to introduce a degree of disordering. An ordered structure of the Al-endmember composition was also evaluated (1 unit cell), but exhibited elevated enthalpy relative to the disordered structure across the entire pressure range of this study and is therefore less stable relative to its disordered counterpart. Two different supercells (8-unit cells) of $AlMg_{0.5}Si_{1.5}O_4(OH)_2$ were evaluated to assess the influence of cation disordering on phase stability and material properties. These two $AlMg_{0.5}Si_{1.5}O_4(OH)_2$ supercells are referred to hereafter as '88-1'

and '88-2'. Atomic positions of the fully optimized Mg-endmember, the disordered Al-endmember, and both supercells of phase D with 50% Al-substitution at ∼0 GPa can be found in the supplemental materials (A.1, A.2, A.3, A.4).

First principles simulations were performed using Quantum ESPRESSO (Giannozzi et al., 2009), in which we applied the generalized gradient approximation (GGA) to the exchange-correlation functional (Perdew et al., 1996), as it more accurately describes hydrogen bonding compared to the local density approximation (e.g., Hamann 1997; Umemoto and Wentzcovitch 1991). The effective interaction of core electrons was approximated using previously evaluated norm-conserving pseudopotentials (Troullier and Martins, 1991) and electronic wave functions were expanded in plane-waves with an energy cutoff of 80 Ry. The irreducible Brillouin zone was sampled by Monkhorst-Pack meshes of 5×5×4, 5×5×2, and 3×3×2 for the Mg-endmember, Al-endmember, and tie-line compositions respectively (Monkhorst and Pack, 1976). The effects of larger energy cut-offs and k-point sampling were found to be negligible. Elastic constants were determined by applying strains of 0.005-0.01 to the optimized (0 K) structures, maintaining linear stress-strain relations (Karki et al., 2001).

2.3 Results

2.3.1 Structure

Optimized structures of the Mg- and Al-endmember compositions, as well both structures of the tie-line composition (50% Al-substitution), were evaluated to determine the influence of Al-substitution on the structure and hydrogen-bonding of phase D. The resultant structures of both the endmember and intermediate compositions are consistent with the previously described trigonal phase D structure (Figure 2.1), with minor triclinic distortion (<2%) consistent with previous calculations (Tsuchiya et al., 2008). The Al-endmember structures exhibit the highest degree of distortion (0.8-1.8%) while the 88-2 structures of the tie-line composition exhibit the lowest degree of distortion (0.2-0.4%). Structural parameters

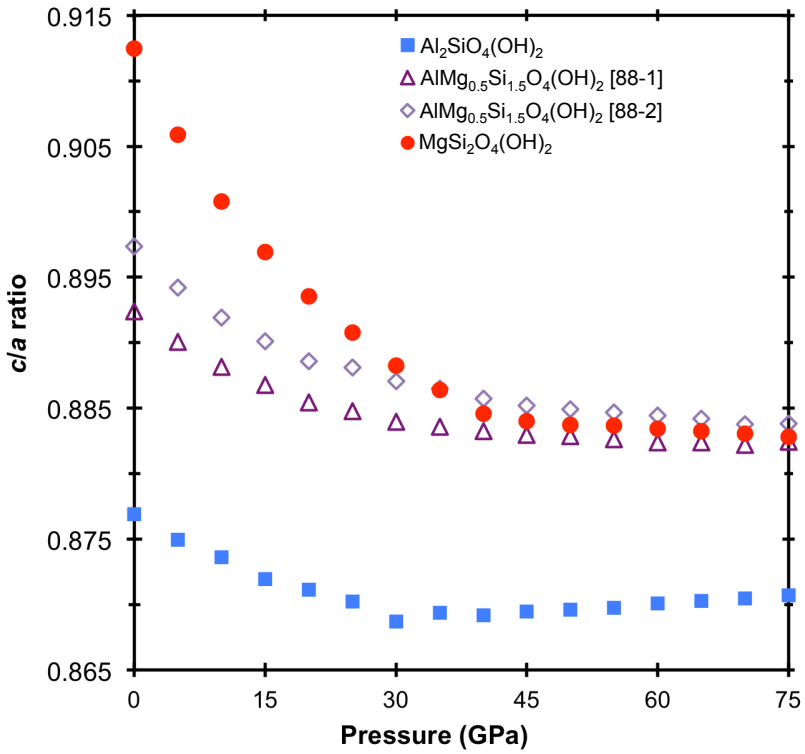

Figure 2.2: The c/a ratio of Mg-endmember phase D (solid red circles), Al-end-member phase D (solid blue squares), tie-line composition in the 88-1 structure (open dark purple triangles), and tie-line composition in the 88-2 structure (open lavender diamonds).

of these phases as a function of pressure from 0 to 75 GPa are reported in Tables A.5, A.6 and A.7. In agreement with previous experimental and theoretical studies (Frost and Fei, 1998; Litasov et al., 2007; Mainprice et al., 2007; Hushur et al., 2011), we find that in Mg-endmember phase D the c-axis is more compressible than the a-axis at low pressures (<40 GPa) and becomes nearly pressure independent above at higher pressures. This disparity in axial compression is also observed in the Al-endmember and tie-line compositions, but the degree of this disparity (i.e., the magnitude of the c/a ratio) is reduced and limited to even lower pressures (<30 GPa) (Figure 2.2, Table A.5).

In reasonable agreement with previous studies (Tsuchiya et al., 2005; Hushur et al., 2011), Mg-endmember phase D undergoes pressure-induced hydrogen bond symmetrization at 45 GPa, a phenomenon in which at elevated pressure the hydroxyl bond length (r_{O-H}) becomes equal to that of the hydrogen bond length ($r_{O\cdots H}$). Al-endmember phase D was also found

to undergo a pressure-induced hydrogen bond symmetrization, albeit at the slightly lower pressure of ∼40 GPa. Conversely, neither configuration of $AlMg_{0.5}Si_{1.5}O_4(OH)_2$ underwent complete pressure-induced hydrogen bond symmetrization in the pressure range of this study, as the more complex cation disordering introduced additional non-degenerate hydrogen sites. The pressure dependence of these sites were found to vary, likely due to differences in nearest-neighbors and next-nearest neighbor cation occupancy (e.g., Thompson et al. 2016a.) Tables containing information regarding the hydrogen ($r_{O\cdots H}$) and hydroxyl ($r_{O—H}$) bond lengths, as well as the H—O···H bond angles for all three compositions are reported in Tables A.6 and A.7, respectively.

Although there is agreement in the literature concerning the existence and magnitude of a pressure-dependent evolution of the c/a ratio in Mg-endmember phase D, as well as its eventual stabilization at high pressures, no such consensus exists regarding the cause. Additionally, the pressure at which the c/a ratio is reported to stabilize varies widely, including reported pressures of 14 GPa (Litasov et al., 2008), 20 GPa (Frost and Fei, 1999), 25 GPa (Litasov et al., 2007), 35 GPa (Shinmei et al., 2008), 40 GPa (Tsuchiya et al., 2005) and 48 GPa (Hushur et al., 2011). In the case of experimental studies, these differences might be partially attributable to variable diavatoric stresses. The larger question is if the low pressure evolution of the phase D lattice parameters is directly tied to hydrogen bond symmetrization (e.g., Hushur et al. 2011) or the result of the layered structure of phase D (e.g., Rosa et al. 2013a). Hydrogen bond symmetrization has been linked to shift in axial compression pre- and post-symmetrization in other phases (e.g., Sano-Furukawa et al. 2009), and has been described as the primary driver of the aforementioned pressure-dependent evolution of c/a ratios in phase D (e.g., Tsuchiya et al. 2005). In this study, all three compositions of phase D have c-axes which are more compressible than the a-axes at low pressure, yet hydrogen bond symmetrization only occurs in the Al- and Mg-endmembers, and occurs at pressures ∼5 GPa higher that the c/a ratio stabilizes. Therefore, it is likely that the low pressure anisotropy is tied to the layered nature of phase D, with differences in the Al- and

Mg-endmembers tied to the relative stiffness of the AlO_6, MgO_6, and SiO_6 units. However, c/a ratio stabilization is seemingly a prerequisite for hydrogen bond symmetrization, such that the two phenomenon can appear coincident. Furthermore, in the case of solid solutions hydrogen bond symmetrization is not expected, but the pressure-dependence of the c/a ratio will likely reflect the compressibilities and configurations of the constituent cation polyhdra.

2.3.2 Equation of state

Optimized (0 K) structures of the endmember and tie-line compositions were used to evaluate the volume-pressure (V-P) relationship of these phases, by fitting them to third-order Birch-Murnaghan equations of state (EOSs) (Birch, 1947):

$$P(V) = \frac{3K_0}{2}\left[\left(\frac{V_0}{V}\right)^{\frac{7}{3}} - \left(\frac{V_0}{V}\right)^{\frac{5}{3}}\right]\left\{1 + \frac{3}{4}\left(K_0' - 4\right)\left[\frac{V_0}{V}^{\frac{2}{3}} - 1\right]\right\} \tag{2.1}$$

in which K_0 is the bulk modulus at ambient pressure, K_0' is the first pressure derivative of the bulk modulus, and V_0 is the reference volume and was treated as a free parameter. The Birch-Murnaghan equation of state parameters (K_0, K_0', V_0) resulting from these fits are shown in Table 2.1. Hydrogen bond symmetrization of Mg-endmember phase D has been previously reported to produce a significant decrease in the compressibility of the hydrogen-symmetric structure (HC) compared to that of the hydrogen off-center (HOC) (e.g., Tsuchiya et al. 2005). In order to more closely evaluate this phenomenon, the Eulerian strain (f) versus normalized pressure (F_E) was plotted (Figure 2.3). This F_E-f plot reveals discontinuities in the compressibility of both Al- and Mg-endmembers, at 35 and 40 GPa respectively. With this in mind, HOC and HC structures of the Mg- and Al-endmember were fit separately, deriving distinct sets of equation of state parameters (Figure A.1). Phase D with 50% Al-substitution did not undergo pressure induced hydrogen bond symmetrization and the F_E-f plot revealed no discontinuities in either the 88-1 or 88-2 configuration, therefore optimized structures spanning the entire pressure range (0-75 GPa) were fit to single equations of state

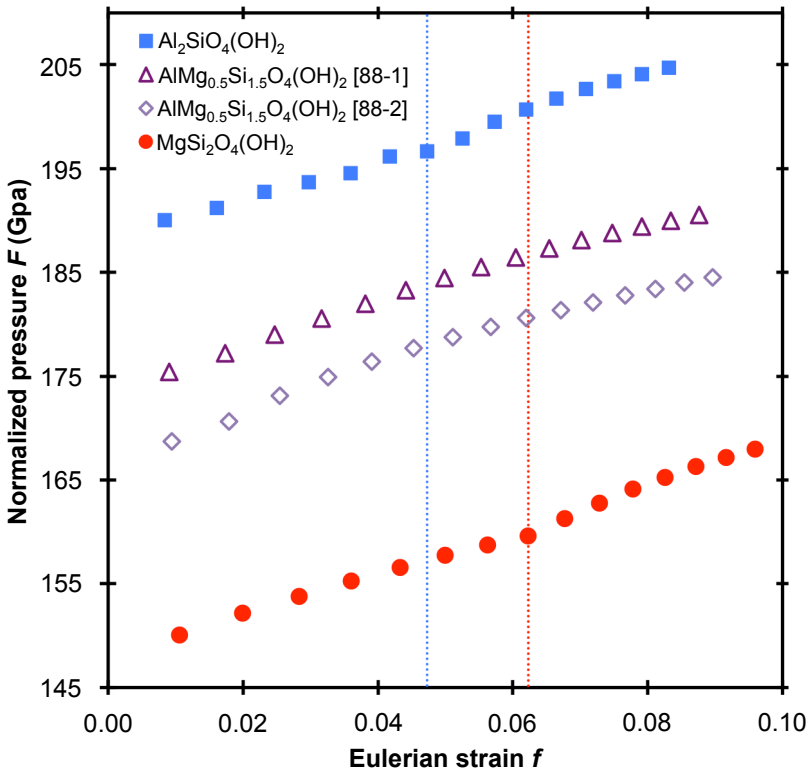

Figure 2.3: Eulerian strain (f) versus normalized pressure (F_E) of $MgSi_2O_4(OH)_2$ (solid red circles), $Al_2SiO_4(OH)_2$ (solid blue squares), $AlMg_{0.5}Si_{1.5}O_4(OH)_2$ in the 88-1 structure (open dark purple triangles), and $AlMg_{0.5}Si_{1.5}O_4(OH)_2$ in the 88-2 structure (open lavender diamonds) Blue and red dotted lines indicates discontinuities due to hydrogen bond symmetrization in the Al- and Mg-endmembers respectively. In this plot the intercept is the value of K_0, the slope reflects the deviation of the first derivative (K_0') from a value of 4, and curvature in the trend reflects the behavior of K_0''.

for each configuration.

Direct comparison to experimentally derived equation of state parameters can be difficult, as even in the case of Mg-endmember phase D a range of compositions have been reported (Table 2.2). Yet despite this compositional variability, our equation of state parameters are in good agreement with previously published values (Figure 2.4). No experimental equations of state for Al-endmember phase D or $AlMg_{0.5}Si_{1.5}O_4(OH)_2$ are known to the author. Our equation of state parameters indicate that Al-endmember phase D is slightly less compressible than the Mg-endmember and that the compressibility of $AlMg_{0.5}Si_{1.5}O_4(OH)_2$ is approximately intermediate to the Mg- and Al-endmember compositions (Figure A.1). As expected, pressure induced hydrogen bond symmetrization resulted in an increase in bulk

Table 2.1: Birch-Murnaghan equations of state parameters for Mg-endmember phase D [$MgSi_2O_4(OH)_2$], Al-endmember [$Al_2SiO_4(OH)_2$], phase D with 50% Al-substitution [$AlMg_{0.5}Si_{1.5}O_4(OH)_2$]. The structure of each intermediate tie-line composition is indicated in brackets. For endmember compositions in which pressure induced hydrogen bond symmetrization occurs, we present parameters fit to the hydrogen off-center (HOC) and hydrogen-centered (HC) structures independently, the structure is indicated in brackets next to the pressure range. Values in parentheses are uncertainties on the last digit.

Composition	Pressure Range (GPa)	V_0 (Å^3)	K_0 (GPa)	K_0'
$MgSi_2O_4(OH)_2$	0-75	86.20(4)	145(1)	5.08(4)
$MgSi_2O_4(OH)_2$	0-75	85.5(2)	173(2)	4(fixed)
$MgSi_2O_4(OH)_2$	0-35 [HOC]	86.14(1)	149.0(3)	4.79(2)
$MgSi_2O_4(OH)_2$	0-35 [HOC]	85.99(4)	160(1)	4(fixed)
$MgSi_2O_4(OH)_2$	40-75 [HC]	84.54(9)	182(2)	4.26(5)
$MgSi_2O_4(OH)_2$	40-75 [HC]	84.05(3)	194.6(5)	4(fixed)
$Al_2SiO_4(OH)_2$	0-75	82.26(2)	186.9(9)	4.77(3)
$Al_2SiO_4(OH)_2$	0-75	81.88(9)	209(2)	4(fixed)
$Al_2SiO_4(OH)_2$	0-30 [HOC]	82.25(1)	188.0(9)	4.67(7)
$Al_2SiO_4(OH)_2$	0-30 [HOC]	82.19(4)	197(1)	4(fixed)
$Al_2SiO_4(OH)_2$	35-75 [HC]	81.47(9)	212.4(3)	4.21(7)
$Al_2SiO_4(OH)_2$	35-75 [HC]	81.20(2)	222.5(5)	4(fixed)
$AlMg_{0.5}Si_{1.5}O_4(OH)_2$ [88-1]	0-75	83.81(2)	177.2(8)	4.61(3)
$AlMg_{0.5}Si_{1.5}O_4(OH)_2$ [88-1]	0-75	83.47(8)	195(1)	4(fixed)
$AlMg_{0.5}Si_{1.5}O_4(OH)_2$ [88-2]	0-75	84.50(2)	172.3(8)	4.57(3)
$AlMg_{0.5}Si_{1.5}O_4(OH)_2$ [88-2]	0-75	84.16(8)	189(1)	4(fixed)

modulus (K_0) for both endmember compositions, accompanied by a modest reduction in (K_0'). Due to the intrinsic trade-off in these parameters, the increase in bulk modulus coincident with hydrogen bond symmetrization was determined using a fixed K_0' value of 4. In the case of $MgSi_2O_4(OH)_2$, the increase in bulk modulus corresponding to hydrogen bond symmetrization is ∼22%, in good agreement with previous calculations (20%, Tsuchiya et al. 2005) and experiments (18%, Hushur et al. 2011), while for $Al_2SiO_4(OH)_2$ the increase is ∼14%.

2.3.3 Elastic constants

The full elastic tensors of the $MgSi_2O_4(OH)_2$, $AlMg_{0.5}Si_{1.5}O_4(OH)_2$, and $Al_2SiO_4(OH)_2$ structures were calculated across the 0 to 75 GPa pressure interval. Although phase D is

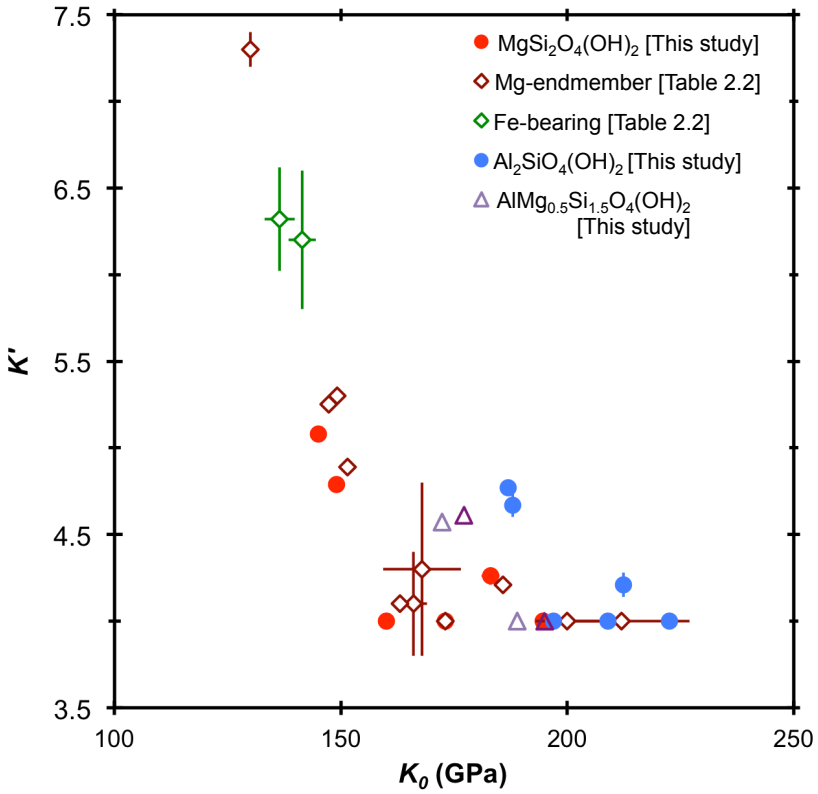

Figure 2.4: Comparison of equation of state parameters for phase D, including $MgSi_2O_4(OH)_2$ (this study, solid red circles), literature values for Mg-endmember phase D (open maroon diamonds), literature values for Fe- and Al- bearing phase D (open green diamonds), $Al_2SiO_4(OH)_2$ (this study, solid blue squares), and $AlMg_{0.5}Si_{1.5}O_4(OH)_2$ in the 88-1 structure and 88-2 structure (this study, open dark purple triangles and open lavender triangles respectively). Error lines indicate the uncertainties as reported by the original authors.

Table 2.2: Previously published Birch-Murnaghan equations of state parameters for phase D of varying compositions. The nature of the study (i.e., experimental or DFT calculations) is indicated, as well the pressure range of each study. In cases where the authors chose to fit hydrogen off-center (HOC) and hydrogen-centered (HC) structures independently due to an observed hydrogen bond symmetrization, those pressure ranges indicate the structure in brackets. Experimental studies reflect room temperature conditions while computational studies were carried out at 0K. Values in parentheses are uncertainties on the last digit as reported by the original authors.

Composition	Study	Method	Pressure Range (GPa)	V_0 (Å^3)	K_0 (GPa)	K_0'
$MgSi_2O_4(OH)_2$	This study	DFT	0 to 75	86.20(4)	145(1)	5.08(4)
$Al_2SiO_4(OH)_2$	This study	DFT	0 to 75	82.26(2)	186.9(9)	4.77(3)
$Mg_{1.11}Si_{1.89}O_6(H)_{2.22}$	Frost and Fei (1998)	experimental	0 to 19.8	85.46(4)	200(7)	4 (fixed)
$Mg_{1.11}Si_{1.6}O_6(H)_{3.4}$	Frost and Fei (1999)	experimental	0 to 30	85.66(4)	166(3)	4.1(3)
$MgSi_2O_6(H)_2$	Tsuchiya et al. (2005)	DFT	0 to 40 [HOC]	86.41	147.29	5.252
$MgSi_2O_6(H)_2$	Tsuchiya et al. (2005)	DFT	40 to 65 [HC]	84.93	185.80	4.209
$Mg_{0.89}Fe_{0.14}Al_{0.25}Si_{1.56}O_6(H)_{2.93}$	Litasov et al. (2007)	experimental	0 to 30.5	86.10(5)	136.5(33)	6.32(30)
$Mg_{0.99}Fe_{0.12}Al_{0.09}Si_{1.75}O_6(H)_{2.51}$	Litasov et al. (2008)	experimental	0 to 20.6	85.32(2)	141.5(30)	6.2(4)
$Mg_{1.02}Si_{1.73}O_6(H)_{3.03}$	Shinmei et al. (2008)	experimental	0 to 44	85.43(4)	130(1)	7.3(1)
$Mg_{1.02}Si_{1.73}O_6(H)_{3.03}$	Shinmei et al. (2008)	experimental	0 to 44	85.43(4)	149.1(7)	5.3 (fixed)
$Mg_{1.02}Si_{1.73}O_6(H)_{3.03}$	Shinmei et al. (2008)	experimental	0 to 44	85.43(4)	163(1)	4.1 (fixed)
$Mg_{1.0}Si_{1.7}O_6(H)_{3.0}$	Hushur et al. (2011)	experimental	0 to 55.8	85.1(2)	167.9(86)	4.3(5)
$Mg_{1.0}Si_{1.7}O_6(H)_{3.0}$	Hushur et al. (2011)	experimental	0 to 30 [HOC]	85.1(2)	173(2)	4 (fixed)
$Mg_{1.0}Si_{1.7}O_6(H)_{3.0}$	Hushur et al. (2011)	experimental	40 to 55.8 [HOC]	85.1(2)	212(15)	4 (fixed)
$Mg_{1.1}Si_{1.8}O_6(H)_{2.5}$	Rosa et al. (2013a)	experimental	0 to 65	85.80(5)	151.4(12)	4.89(8)

trigonal, we calculated the 21 independent elastic constants needed to describe the slight triclinic distortion in our optimized structures. The major single crystal elastic constants (C_{11}, C_{22}, C_{33}, C_{44}, C_{55}, C_{66}) are plotted in Figure 2.5, and the full elastic tensors are included in tabulated form in Tables A.8, A.9, A.10, A.11, A.12, A.13, A.14, and A.15.

The Mg-endmember constants from this study are in close agreement with the previously published calculated elastic constants of Tsuchiya et al. (2008) and Mainprice et al. (2007), which themselves have been extensively compared to experimental results. In the case of the C_{11}, C_{44}, and C_{55} constants, both 88-1 and 88-2 structures of the intermediate composition are bounded by the constants of the endmember compositions, with the Al-endmember C_{44} and C_{55} significantly higher than those of the Mg-endmember. The C_{22} constant largely follows the same pattern, with elevated values for $Al_2SiO_4(OH)_2$ compared to $MgSi_2O_4(OH)_2$, but the the 88-1 structure of $AlMg_{0.5}Si_{1.5}O_4(OH)_2$ is virtually indistinguishable from the Al-endmember. At low pressures the C_{33} of the intermediate composition is also bracketed by the endmember compositions, but coincident with the onset of hydrogen bond symmetrization in these phases the C_{33} of both endmembers undergo discontinuous behavior, increasing abruptly before again smoothly increasing with pressure. The H—O···H bonds within phase D are most closely aligned to the c-axis (Figure 2.1), therefore it is intuitive that the C_{33} elastic constant which indicates stiffness along the c-axis is the most dramatically impacted by hydrogen bond symmetrization. As neither structure of $AlMg_{0.5}Si_{1.5}O_4(OH)_2$ undergoes pressure induced hydrogen bond symmetrization, the C_{33} of this intermediate composition is lower than either endmember at pressures greater than 40 GPa. Lastly, the C_{66} of the tie-line composition of both structures is slightly elevated compared to the end-member compositions. This might be explained by the fact that the triclinic distortion evident in the endmembers structures is absent in the $AlMg_{0.5}Si_{1.5}O_4(OH)_2$ super-cells, with the C_{66} constant accommodating some of the strain otherwise accommodated by these lesser components.

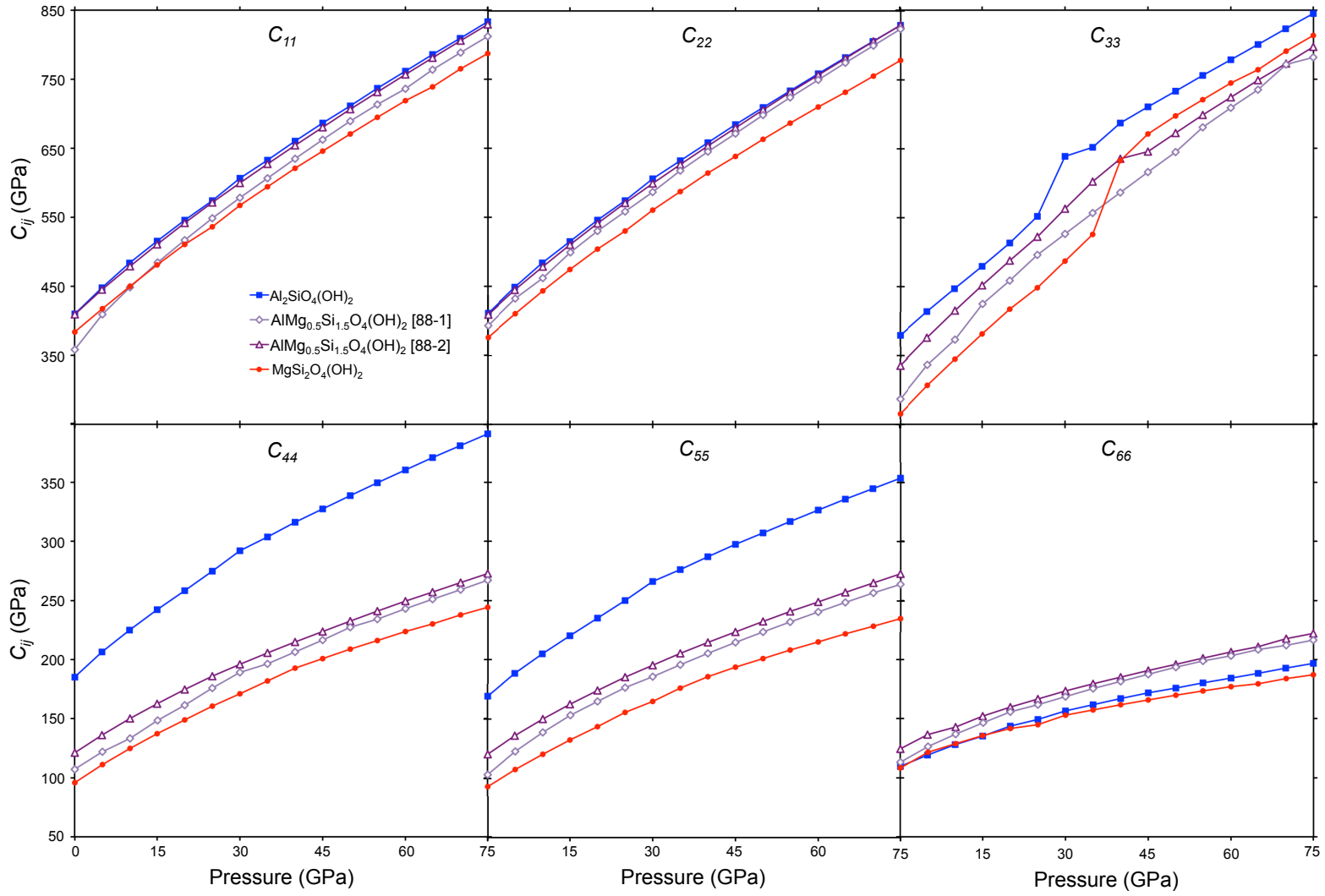

Figure 2.5: The (a) C_{11}, (b) C_{22}, (c) C_{33}, (d) C_{44}, (e) C_{55}, and (f) C_{66} elastic constants of $MgSi_2O_4(OH)_2$ (solid red circle), $AlMg_{0.5}Si_{1.5}O_4(OH)_2$ (solid blue squares), $AlMg_{0.5}Si_{1.5}O_4(OH)_2$ in the 88-1 structure (open dark purple triangles), and $AlMg_{0.5}Si_{1.5}O_4(OH)_2$ in the 88-2 structure (open lavender diamonds).

2.3.4 Moduli and velocities

Bulk and shear moduli of the Mg-endmember, Al-endmember, and two structures of the tie-line composition were calculated from the single crystal elastic constants using the Voigt-Reuss-Hill averaging scheme as shown in Figure 2.6a and Table A.16 (Hill, 1952). The pressure dependence of the bulk modulus of both Al- and Mg-endmembers exhibit discontinuities, reflecting the previously described decrease in compressibility which accompanies pressure-induced hydrogen bond symmetrization in these phases, particularly in along the c-axis. A more subtle inflection is also visible in the shear modulus of the Mg-endmember although no analogous discontinuity occurs within the Al-endmember. Notably, the $AlMg_{0.5}Si_{1.5}O_4(OH)_2$ in both the 88-1 and 88-2 structures has a bulk modulus approximately intermediate to the Mg- and Al-endmembers prior to the onset of hydrogen bond symmetrization at low pressures, but above ∼45 GPa these tie-line compositions have a bulk modulus nearly indistinguishable from that of the Mg-endmember. Additionally, the shear modulus of the intermediate composition is nearly indistinguishable from that of the Al-endmember in the case of both structures evaluated across the entire pressure range investigated.

As phase D exhibits both anisotropic compression, evident in the low-pressure evolution of the c/a ratio, as well as hydrogen bond symmetrization, determining the influence of cation substitution on compressibility is a complex issue. Al-bearing solid solution compositions of phase D have physical properties that are not predicted by interpolation between the endmembers. While the low pressure anisotropy in phase D is likely dictated by differential strain accommodation due to varying cation occupancies in the layered structure, Al-substitution also suppresses hydrogen bond symmetrization, indirectly influencing the elastic behavior. Parsing these distinct but overlapping effects experimentally will likely be daunting, particularly when exploring even more complex compositions (e.g., Fe-substitution). First principles calculations provide a theoretical framework and detailed structural information which com-

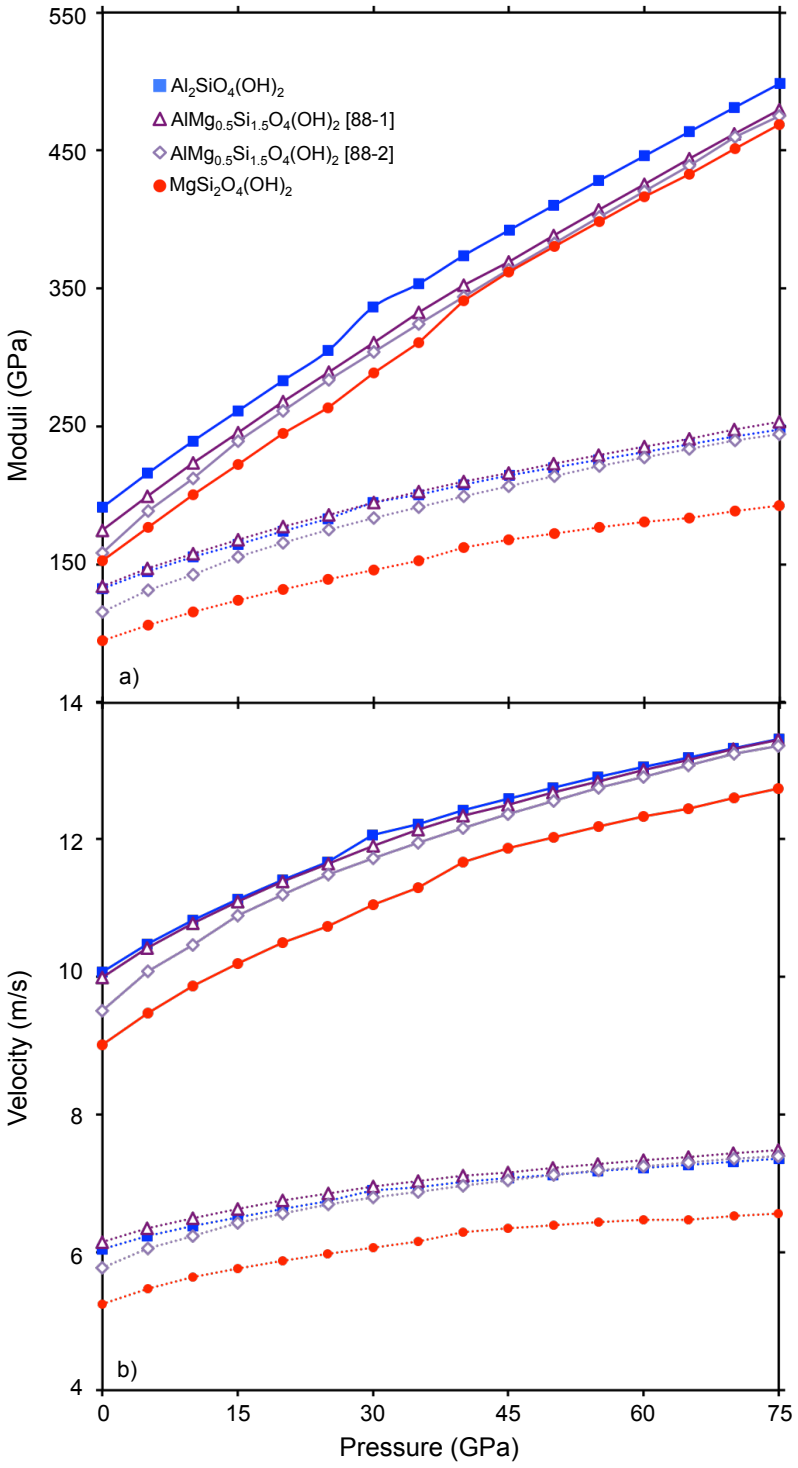

Figure 2.6: (a) Moduli of phase D including bulk modulus (solid line) and shear modulus (dotted line), and (b) sound velocities of phase D including compressional velocity (solid line), and shear velocity (dotted line) of Mg-endmember phase D (solid red circles), Al-end-member phase D (solid blue squares), tie-line composition in the 88-1 structure (open dark purple triangles), and the tie-line composition in the 88-2 structure (open lavender diamonds).

plement and elucidate more compositionally complex experimental studies.

2.4 Discussion

Previous work has investigated the influence of phase D on the velocity structure of hydrous subducting slabs, of which phase D may be a significant component (Mainprice et al., 2007; Rosa et al., 2012, 2013b). These studies have focused on determining to what extent phase D, which exhibits relatively high degree of shear wave anisotropy (AV_S), contributes to observations of shear wave spitting ($S_H > S_V$) in stagnant slabs. Although Rosa et al. (2012) evaluated the influence of compositional variation on these properties and determined the influence of cation substitution was negligible, the extent of solid solution in that study was extremely limited [$Al_{0.03}Fe_{0.11}Mg_{1.0}Si_{1.5}O_4(OH)_2$]. Furthermore, the interpretation of the influence of either Al- or Fe-substitution on the properties of phase D in that study is complicated by the inclusion of both in a single, compositionally complex sample.

We evaluated the influence of Al-substitution on the seismic anisotropy of phase D using the Christoffel equation (Mainprice et al., 2011), reducing our triclinic elastic constants to the appropriate trigonal symmetry with a weighted mean to enable direct comparison to literature values. The maximum shear wave polarization anisotropy (AV_S) of Mg-endmember, Al-endmember, and the tie-line composition of phase D as a function of pressure are reported in Table A.18. At 0 GPa, we find the maximum AV_S of $MgSi_2O_4(OH)_2$ is quite high (AV_S=21.86), in good agreement with previously reported values by Mainprice et al. (2007) (AV_S=19.92) and Rosa et al. (2012) (AV_S=17.69). However, we find a strong, negative pressure dependence of the shear wave polarization anisotropy in $MgSi_2O_4(OH)_2$, such that by the pressure of the lower mantle the magnitude is of the AV_S is halved (Figure 2.7a). Conversely, at 0 GPa the maximum shear wave polarization anisotropy of Al-endmember phase D is significantly lower than that of the Mg-endmember (AV_S=10.65), but due to its strong positive pressure dependence is nearly double that of the Mg-endmember at lower mantle pressures (Figure 2.7b). Additionally, in Al-endmember phase D the maximum shear

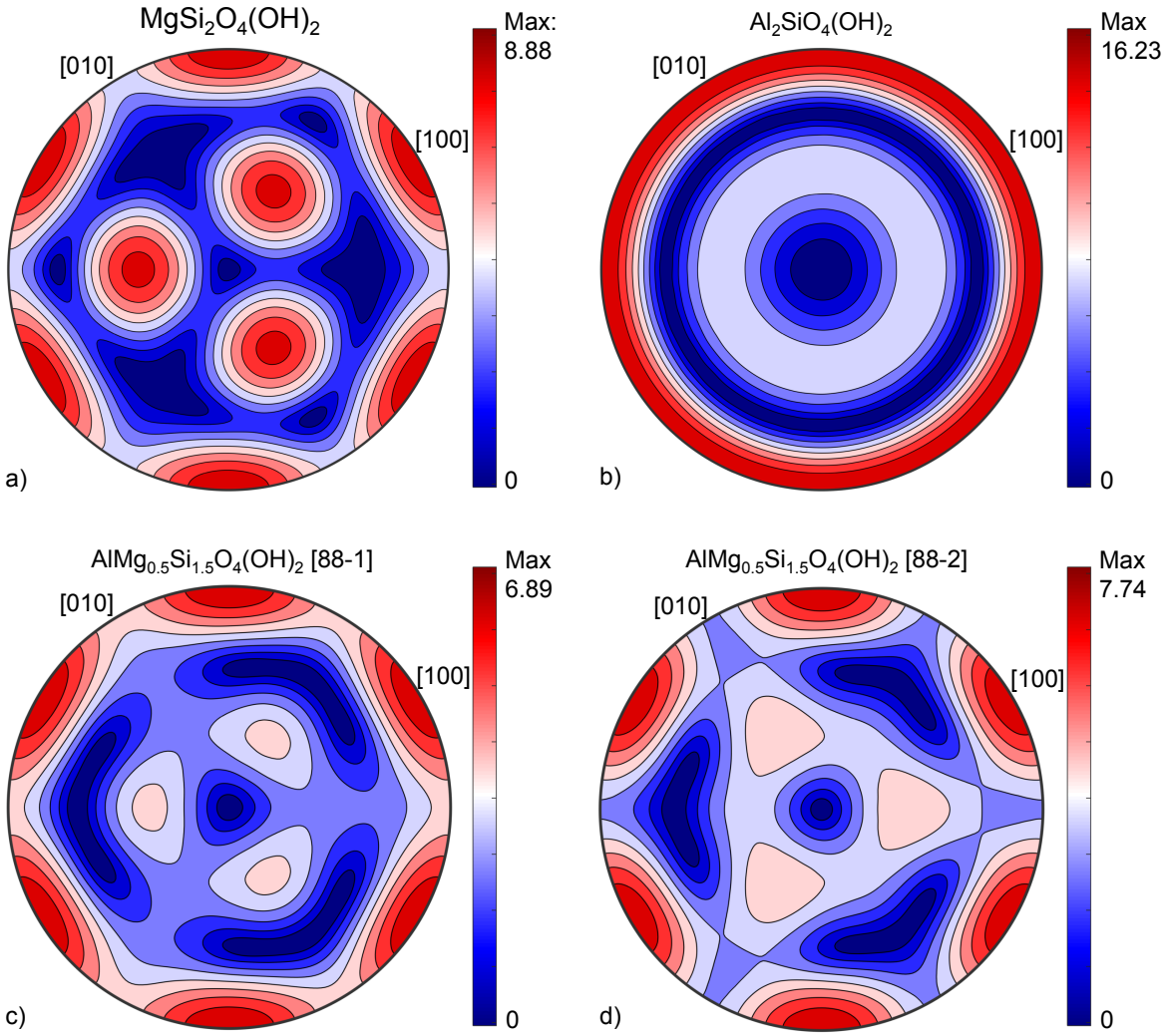

Figure 2.7: Lambert equal-area upper-hemisphere projection of the shear wave polarization (AV_S) of phase D at 30 GPa, including (a) $MgSi_2O_4(OH)_2$, (b) $AlMg_{0.5}Si_{1.5}O_4(OH)_2$, (c) $AlMg_{0.5}Si_{1.5}O_4(OH)_2$ in the 88-1 structure, and (d) $AlMg_{0.5}Si_{1.5}O_4(OH)_2$ in the 88-2 structure. Images were generated using software by Mainprice et al. (2011).

anisotropy exists not only along the a-axis, as in the Mg-endmember, but also along the b-axis.

Based on our observation that the elastic properties of $AlMg_{0.5}Si_{1.5}O_4(OH)_2$ could not be accurately determined by interpolating the properties of the Mg- and Al-endmembers compositions, we evaluated the maximum shear wave polarization anisotropy of the tie-line composition of phase D as a function of pressure (Table A.18). At 0 GPa, the maximum AV_S of both structures (88-1 and 88-2) of the tie-line compositions are intermediate to

that of the Al- and Mg-endmembers (13.48 and 14.87, respectively) (Figure 2.7c and 2.7d). However, like the Mg-endmember, the AV_S of both the 88-1 and 88-2 structures exhibits a negative pressure-dependence at pressures up to ∼50 GPa. Ultimately, both structures of $AlMg_{0.5}Si_{1.5}O_4(OH)_2$ exhibit less shear wave polarization anisotropy than either the Al- or Mg-endmember to pressures up to 70 GPa. As non-endmember, Al-bearing phase D has less shear wave anisotropy than either endmember, studies that estimate regional volume % of D based on matching shear-wave splitting observations based on the properties of $MgSi_2O_4(OH)_2$ or $AlMg_{0.5}Si_{1.5}O_4(OH)_2$ likely underestimated the amount of phase D needed to mimic observations.

2.5 Conclusions

By evaluating three compositions of phase D [$MgSi_2O_4(OH)_2$, $AlMg_{0.5}Si_{1.5}O_4(OH)_2$, $Al_2SiO_4(OH)_2$] using density theory based calculations we were able to probe the extent to which Al-substitution influences the physical properties of this phase. Al-endmember phase D is denser (2-6%, Figure A.2), less compressible (6-25%), and has faster compressional (6-12%) and shear velocities (12-15%) relative to its Mg-endmember counterpart. However, when contemplating the solid solutions more realistically expected in the complex mineralogy of a subducting slab, these properties cannot be determined via a simple volumetric mixing model. In evaluating the properties of two structures of phase D with 50% Al-substitution we see that these tie-line compositions exhibit properties radically different than what would be obtained by interpolating between the endmembers. Furthermore, comparison of these two $AlMg_{0.5}Si_{1.5}O_4(OH)_2$ structures reveals that not only which cations substitute into phase D, but where they substitute, can also dictate macroscale bahavior. Solid solution seemingly inhibits pressure-induced hydrogen bond symmetrization, which in turn significantly influences compressibility at upper mantle pressures. Not only are the elastic tensors of the tie-line composition far from intermediate to the endmembers, but at sufficiently high pressures (>45 GPa) the shear wave velocities of the $AlMg_{0.5}Si_{1.5}O_4(OH)_2$ are higher than

those of either $MgSi_2O_4(OH)_2$ or $Al_2SiO_4(OH)_2$. Lastly, $AlMg_{0.5}Si_{1.5}O_4(OH)_2$ has a lower maximum shear wave polarization anisotropy than either the Mg- or Al-endmember compositions, and studies which constrain the the quantity of phase D in the deep Earth by matching seismic structures to the properties of either endmember may be misleading.

CHAPTER 3

CALCULATED ELASTICITY OF ϵ-FeOOH

3.1 Introduction

Goethite (α-FeOOH) is an abundant and widespread iron oxy-hydroxide found in sediments, ore deposits, and as a primary component of rust at the Earth's surface. This low-pressure structure undergoes a first-order phase transition accompanied by a 7% density increase, transforming into the high-pressure phase ε-FeOOH at $\sim$6 GPa (Bendeliani et al., 1972; Gleason et al., 2008). Structural refinement based on moderate-pressure (<10 GPa) X-ray and neutron diffraction experiments indicate that ε-FeOOH is orthorhombic (space group $P2_1nm$, Z = 2), composed of edge sharing FeO_6 units that are closely packed along the c-axis, forming a rutile-like structure with hydrogen occupying the channels between the edge-sharing chains (Bolotina et al., 2008). This high-pressure phase is reported to undergo a pressure-induced hydrogen bond symmetrization leading to a second order phase transition from P2_1nm to $Pnnm$ (Gleason et al., 2008).

The high-pressure symmetric phase is shown in Figure 3.1, as is the spin polarization density of the iron atoms within the structure. Unfortunately, the exact pressure of this hydrogen bond symmetrization has been difficult to assess, as the corresponding volume change is minimal and hydrogen's minimal cross section makes its position indeterminate by X-ray diffraction. Previously reported pressures of hydrogen bond symmetrization have ranged from 25 to 45 GPa (Xu et al., 2013; Gleason et al., 2013). Additionally, ε-FeOOH has been experimentally demonstrated to undergo a spin transition between 40 and 60 GPa (Gleason et al., 2013). There are numerous complications inherent to experiments on iron-bearing, hydrous phases, including the multiple valence states of iron, defects associated with hydrogen substitution, and in the case of X-ray diffraction studies, the need for a secondary probe to enable the detection of hydrogen (Hu et al., 2016). These complications render phases such as FeOOH ideal candidates for study via density functional theory (DFT)

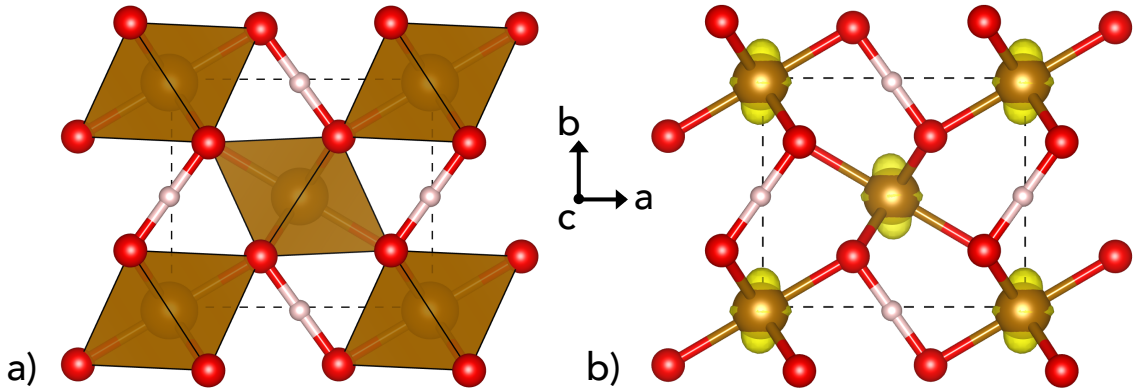

Figure 3.1: High-pressure hydrogen-centered ε-FeOOH structure at 30 GPa. (a) Crystal structure with orange polyhedral representing FeO_6. Large red spheres are O atoms and small white spheres are H atoms. (b) Spin polarization density map (ρ_{up}–ρ_{down}) with yellow isosurface indicating a value of 0.078 e^-/a.u.^{3}. Images were generated in VESTA (Momma and Izumi, 2008).

calculations, particularly in determining material properties at the extreme pressures relevant to the Earth's mantle.

At ambient pressure goethite (α-FeOOH) is isomorphous with the low-pressure aluminum oxide hydroxide diaspore (α-AlOOH). As with goethite, diaspore undergoes a pressure induced phase change, transforming into the high-pressure phase δ-AlOOH, which is isostructural with the high-pressure phase ε-FeOOH (Suzuki, 2010). As with ε-FeOOH, δ-AlOOH undergoes a second-order phase transition due to hydrogen bond symmetrization, though at slightly higher pressures (Tsuchiya et al., 2002; Sano-Furukawa et al., 2009; Kuribayashi et al., 2014). It is presumable that the post-hydrogen bond symmeterized structures of these compositions form a solid solution, which is particularly exciting as δ-AlOOH has a pressure-temperature (P-T) stability that extends to the Earth's core-mantle boundary (CMB) (Sano et al., 2008).

Recently a new dense hydrous magnesium silicate, phase H ($MgSiO_4H_2$), was predicted via DFT calculations and subsequently confirmed experimentally (Tsuchiya, 2013; Nishi et al., 2017). This phase has the highest reported P-T stability of any of the so-called 'alphabet' phases of dense hydrous magnesium silicates. Phase H also belongs to the *Pnnm*

space group (Bindi et al., 2014) and there likely exists a solid solution between phase H, δ-AlOOH, and ε-FeOOH. Aluminum substitution has been experimentally determined to stabilize phase H, but the precise influence of iron on this system remains poorly defined. This study aims to describe the high-pressure elasticity of low-spin hydrogen-symmetric ε-FeOOH, as a means of better understanding the stability and properties of the only known hydrous solid solution with P-T stability that extends throughout the Earth's mantle.

3.2 Methods

Consistent with the methods of 2.2, *first principles* calculations were conducted using the generalized gradient approximation (GGA) to the exchange-correlation functional (Perdew et al., 1996), which more accurately describes hydrogen bonding compared to a local density approximation (LDA) (Umemoto and Hirose, 2015). Density functional theory calculations were performed both with and without the addition of an on-site Coloumbic self-interaction term (U). The addition of a Hubbard U term is critical to accurately describing the stability, electronic, magnetic, and elastic properties of iron-bearing systems, as is the selection of an appropriate U value (Jang et al., 1994). In the case of GGA+U calculations, Hubbard U values were determined by an internally consistent method (Cococcioni and de Gironcoli, 2005; Tsuchiya et al., 2006; Nishi et al., 2017), and a second set of calculations were performed with a fixed value of U=5 to allow direct comparison with literature values (Gleason et al., 2008). All values reported herein reflect self-consistent U-value calculations unless otherwise indicated.

Optimized structures were solved using damped variable cell shape molecular dynamics (Wentzcovitch, 1991) as part of the Quantum ESPRESSO Package (Giannozzi et al., 2009). The effective interaction of core electrons was approximated using previously evaluated norm-conserving pseudopotentials (Troullier and Martins, 1991) with the exception of iron, in which case ultrasoft pseudopotentials were employed (Vanderbilt, 1990; Ichikawa et al., 2014). The irreducible Brillouin zone was sampled by a 4×4×8 Monkhorst Pack mesh (Monkhorst

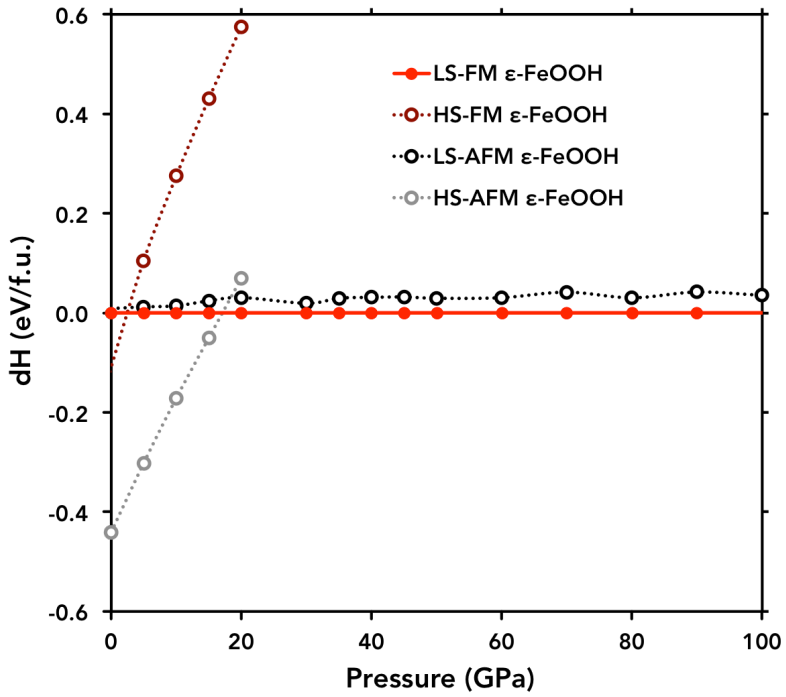

Figure 3.2: Calculated relative enthalpies of ε-FeOOH from 0 to 100 GPa.

and Pack, 1976) and electronic wave functions were expanded in plane-waves with an energy cutoff of 80 Ry. The effects of larger energy cut-offs and k-point sampling were found to be negligible. Elastic constants were determined by applying strains of magnitude 0.01-0.001 depending on the linearity of stress-strain relations (Karki et al., 2001) to optimized, static (0 K) structures.

3.3 Results

3.3.1 Structure

Structural parameters of ε-FeOOH from the GGA+U calculations are plotted in Figure 3.3, and a tabulated version can be found in Table B.1. Analyses of the optimized structural parameters based on both GGA and GGA+U calculations reveal a discontinuity consistent with a second order phase transition due to hydrogen bond symmetrization at ∼10 GPa. Hydrogen bond symmetrization occurs when the hydroxyl bond length ($r_{O—H}$) is equal to the

hydrogen bond length ($r_{O\cdots H}$), therefore comprising half the total oxygen to oxygen distance ($r_{O—O}$). The FeO_6 polyhedral volume pre- and post-hydrogen bond symmetrization were fit to third-order Birch-Murnaghan equations of state (Table 3.1).

These polyhedral equation of state parameters indicate a change in primary strain accommodation mechanism pre- and post-hydrogen bond symmetrization, with hydrogen bonds accommodating more relative strain prior to symmetrization, as seen in Figure 3.5. This shift in strain accommodation is reflected in the pronounced change in pressure derivative of the bulk modulus of the FeO_6 (Table 3.1). This change in strain accommodation mechanism leads to structural changes in both unit cell volume and lattice parameters (Figure 3.3a and 3.3b), a phenomenon previously reported in the experimental study of the effect of hydrogen-bond symmetrization on the compressibility of δ-AlOOH (Sano-Furukawa et al., 2009).

Calculated low-spin ε-FeOOH lattice parameters are in good agreement with previously reported experimental values by Gleason et al. (2013) albeit with a slight underestimate of lattice parameters as shown in Figure 3.3b. Note, the experimental data shown reflects both high-spin and low-spin ε-FeOOH, and agreement with our calculations is only expected at the highest pressure data points, as the high → low spin transition is associated with a significant decrease in unit cell volumes. Additionally, it should be noted that Gleason and coauthors found their experimental data was best fit to their DFT calculation for antiferromagnetic (AFM) low-spin ε-FeOOH using a fixed U value. In this study we reevaluated the stability

Table 3.1: Birch-Murnaghan equation of state parameters of FeO_6 polyhedra in the low-pressure hydrogen off-center (HOC) structure and high-pressure hydrogen bond symmeterized structure (HC) based on self-consistent U-value calculations. Values in parentheses are uncertainties on the last digit.

	HOC (0-20 GPa)	HC (30-140 GPa)
V_0 (Å^3)	10.18(1)	10.06(1)
K_0 (GPa)	205(10)	196(1
K_0'	1.09(83)	4.79(1)

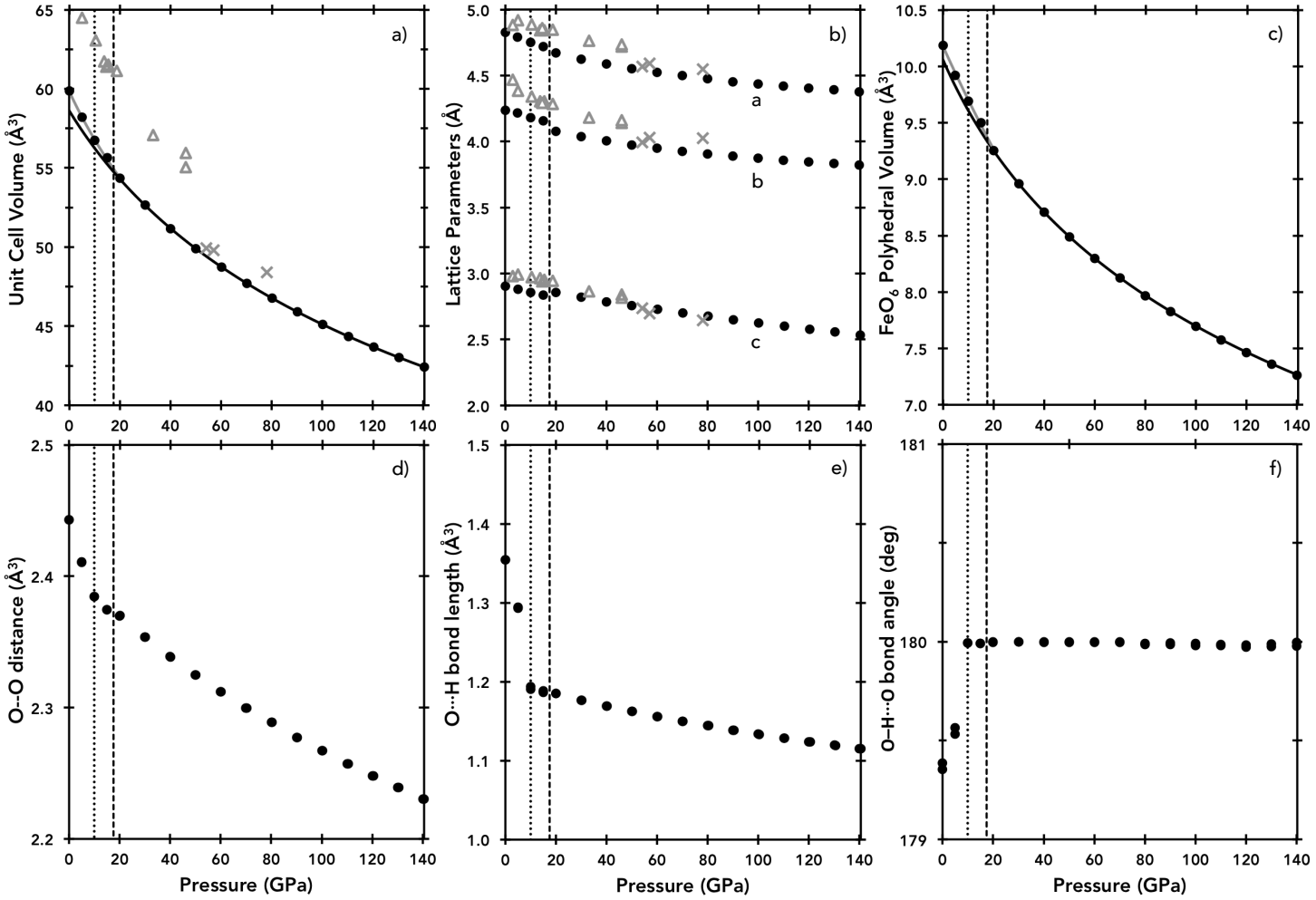

Figure 3.3: Calculated structural parameters of low-spin ferromagnetic ε-FeOOH from 0 to 140 GPa by GGA+U including (a) unit cell volume, (b) lattice parameters, (c) FeO_6 polyhedral volume, (d) O—O distance, (e) O···H bond length, (f) O—H···O angle. Solid black lines are equations of state fitted to hydrogen-centered (HC) structures while solid grey lines are equations of state fitted to hydrogen off-centered (HOC) low-pressure structures. Dotted line indicates pressure at which hydrogen bond symmetrization occurs, dashed line indicates pressure at which symmetry change occurs, and grey symbols are experimental data (Gleason et al., 2013), with open triangles indicating high-spin ε-FeOOH and X's indicating low-spin ε-FeOOH.

of both AFM and ferromagnetic (FM) structures on the basis of calculated enthalpy, and determined the FM structure to be slightly more stable (∼0.03 eV) at all pressure points based on calculations using both a fixed or self-consistent U parameter (Figure 3.2). Monoclinic distortion (i.e., deviation from orthorhombic lattice angles of 90°) remained minimal (< 1°) throughout the entire pressure range investigated.

3.3.2 Equation of state and density of states

Compressive behavior of the unit cell as a whole changes as a result of hydrogen bond symmetrization, consistent with prior studies of hydrous phases including δ-AlOOH and phase H (Tsuchiya and Tsuchiya, 2009; Tsuchiya and Mookherjee, 2015). Hydrogen bond symmetrization led to a ∼19% increase in the bulk modulus (K_0) and a ∼22% reduction of its pressure derivative (K_0') (Table 3.2). Due to changes in compressional behavior coincident with the second-order transition due to hydrogen bond-symmetrization, pre- and post-symmeterized structures were treated as separate phases and used to derive separate sets of equation of state parameters. Calculated volumes of optimized structures of both GGA and GGA+U calculations were used to fit third-order Birch-Murnaghan equations of state (Birch, 1947):

$$P(V) = \frac{3K_0}{2}\left[\left(\frac{V_0}{V}\right)^{\frac{7}{3}} - \left(\frac{V_0}{V}\right)^{\frac{5}{3}}\right]\left\{1 + \frac{3}{4}\left(K_0' - 4\right)\left[\frac{V_0}{V}^{\frac{2}{3}} - 1\right]\right\} \tag{3.1}$$

in which K_0 is the bulk modulus at ambient pressure, K_0' is the first pressure derivative of the bulk modulus, V_0 is the reference volume. Results from these fits are listed in Table 3.1; the GGA+U results should be preferred because the U term provides a more accurate characterization of the transition metal bonding. This resulted in significantly lower errors in comparison to fitting the entire pressure range with a single equation of state. The reference volume (V_0) was treated as a free parameter in the equation of state fitting.

The density of states (DOS) of ferromagnetic low-spin ε-FeOOH was determined from

optimized structures at five GPa intervals below 20 GPa and at ten GPa intervals up to 140 GPa. These densities of states, referenced to the Fermi level, indicate a clear and abrupt change in orbital structure pre- versus post-hydrogen bond symmetrization (Figure 3.4). Densities of states at all pressures in the 0 to 140 GPa range exhibit nonzero bandgaps indicative of insulator behavior, with increased bandwidths at higher pressures. There is a secondary and more gradual pressure dependent evolution in the structure of the density of states above 20 GPa and independent of hydrogen bond symmetrization. The general structure of the density of states and band gap width at 60 GPa are similar to those calculated for ferromagnetic low-spin ε-FeOOH at comparable pressure by Otte et al. (2009).

3.3.3 Elastic Constants

The elastic tensor of the high-pressure hydrogen-centered structure of ε-FeOOH was determined up to CMB pressure. Because of the orthorhombic symmetry of ε-FeOOH, there are nine unique elastic constants needed to fully describe the elastic behavior of this phase as a function of pressure (Figure 3.5). The full elastic tensors as a function of pressure are also reported in tabulated form in Table B.2. Calculated structures using only GGA, without the addition of the columbic self-interaction term (U) are systematically smaller than structures determined using the GGA+U method at the same pressure. Yet a comparison of GGA and GGA+U elastic constants, normalized by volume, reveals little discrepancy (mean deviation <8%) in the value or trend of the elastic constants of the HC structure over the pressure

Table 3.2: Birch-Murnaghan equation of state parameters for the low-pressure hydrogen off-center (HOC) structure and high-pressure hydrogen bond symmeterized structure (HC), based on self-consistent U-value calculations. Values in parentheses are uncertainties on the last digit.

	HOC (0-20 GPa)	HC (30-140 GPa)
V_0 (Å^3)	57.43(7)	58.62(5)
K_0 (GPa)	188(4)	223(2)
K_0'	5.19(12)	4.07(3)

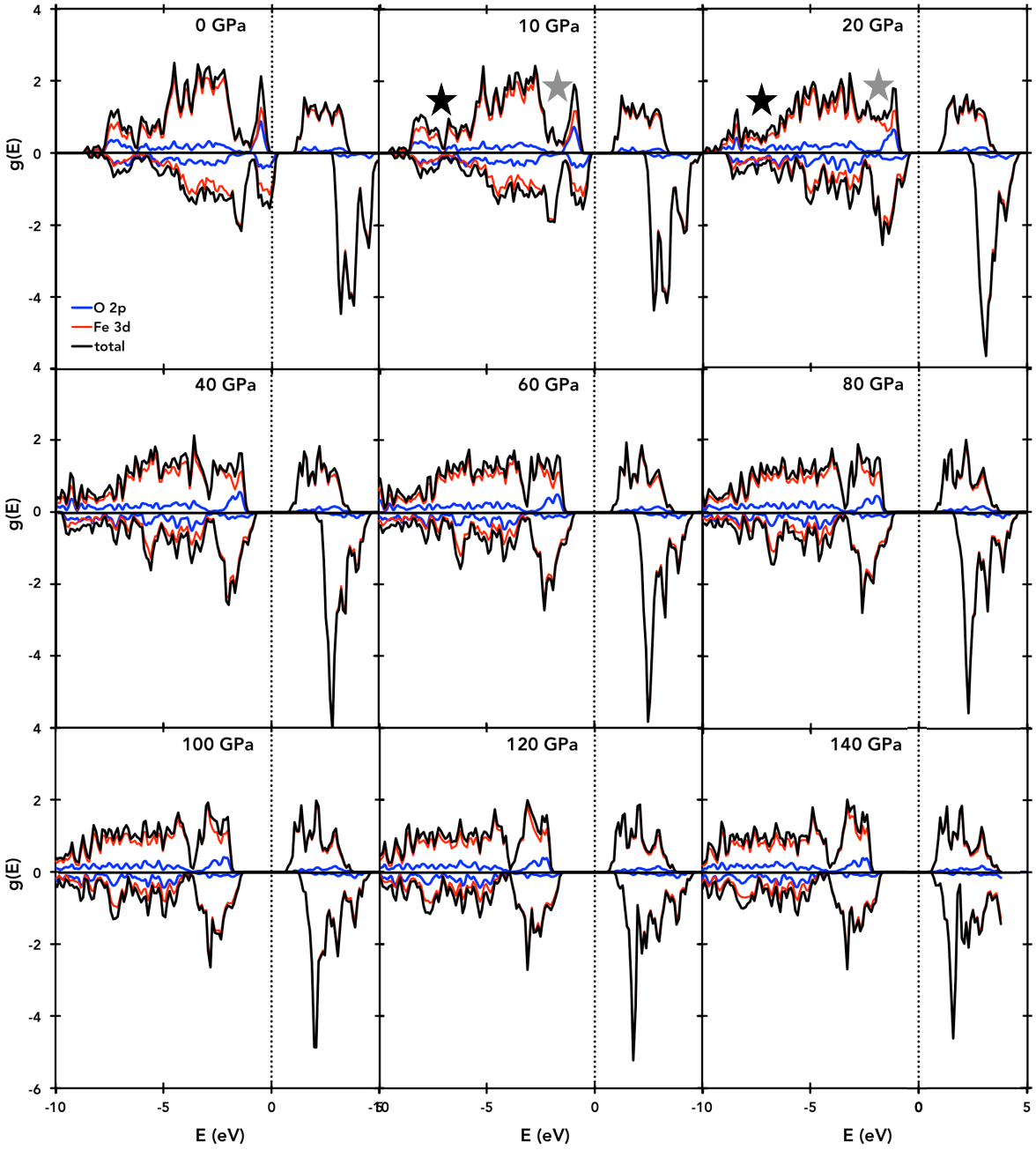

Figure 3.4: Calculated density of states relative to the Fermi level from 0 to 140 GPa. Dotted lines indicate the Fermi level (E=0). Black and dark grey stars indicate local minima which increase across the pressure-induced hydrogen bond symmetrization-induced symmetry transition.

range investigated. Seven of the nine elastic constants exhibit positive slopes and smooth trends indicative of gradual stiffening with increasing pressure, while the C_{55} elastic constant is pressure insensitive and the C_{44} elastic constant decreases with increasing pressure.

The three Born stability criteria (Born and Huang, 1954) relevant to orthorhombic symmetry (See Eqs. B.1, B.2, and B.3 in Appendix) were calculated for the entirety of the pressure range for which the HC structure elastic constants were determined (30 to 140 GPa) and the structure was found to be mechanically stable, as shown in Figure 3.6. Nevertheless, the negative pressure dependence of C_{44} is indicative of eventual mechanical instability at sufficiently high pressures. To better constrain the elastic behavior of intermediate compositions the elastic tensor of ε-FeOOH is compared to that of δ-AlOOH and phase H, with which it is isostructural. The Fe-endmember (ε-FeOOH) has smaller diagonal elastic constants and larger off-diagonal elastic constants than those of either δ-AlOOH (Tsuchiya and Tsuchiya, 2009) or phase H (Tsuchiya and Mookherjee, 2015) (Figure 3.5).

Bulk and shear moduli of the HC phase were calculated from single crystal elastic constants using the Voigt-Reuss-Hill averaging scheme as shown in Figure 3.7a and Table 3.3 (Hill, 1952). The bulk modulus (K) of HC-structure ε-FeOOH smoothly increases with pressure but the shear modulus (μ) is nearly pressure independent. In comparison with that of ε-FeOOH, the bulk modulus and its pressure dependence of both phase H and hydrogen-centered structure of δ-AlOOH are quite similar, averaging 7% and 10% lower, respectively, across the 30 to 100 GPa pressure interval (Tsuchiya and Mookherjee, 2015; Tsuchiya and Tsuchiya, 2009). The pressure dependence of the shear modulus of ε-FeOOH differs dramatically from those of phase H and δ-AlOOH. Both δ-AlOOH and phase H have positive, albeit small, pressure dependences in contrast to the negative pressure dependence of the Fe-endmember (Tsuchiya and Mookherjee, 2015; Tsuchiya and Tsuchiya, 2009).

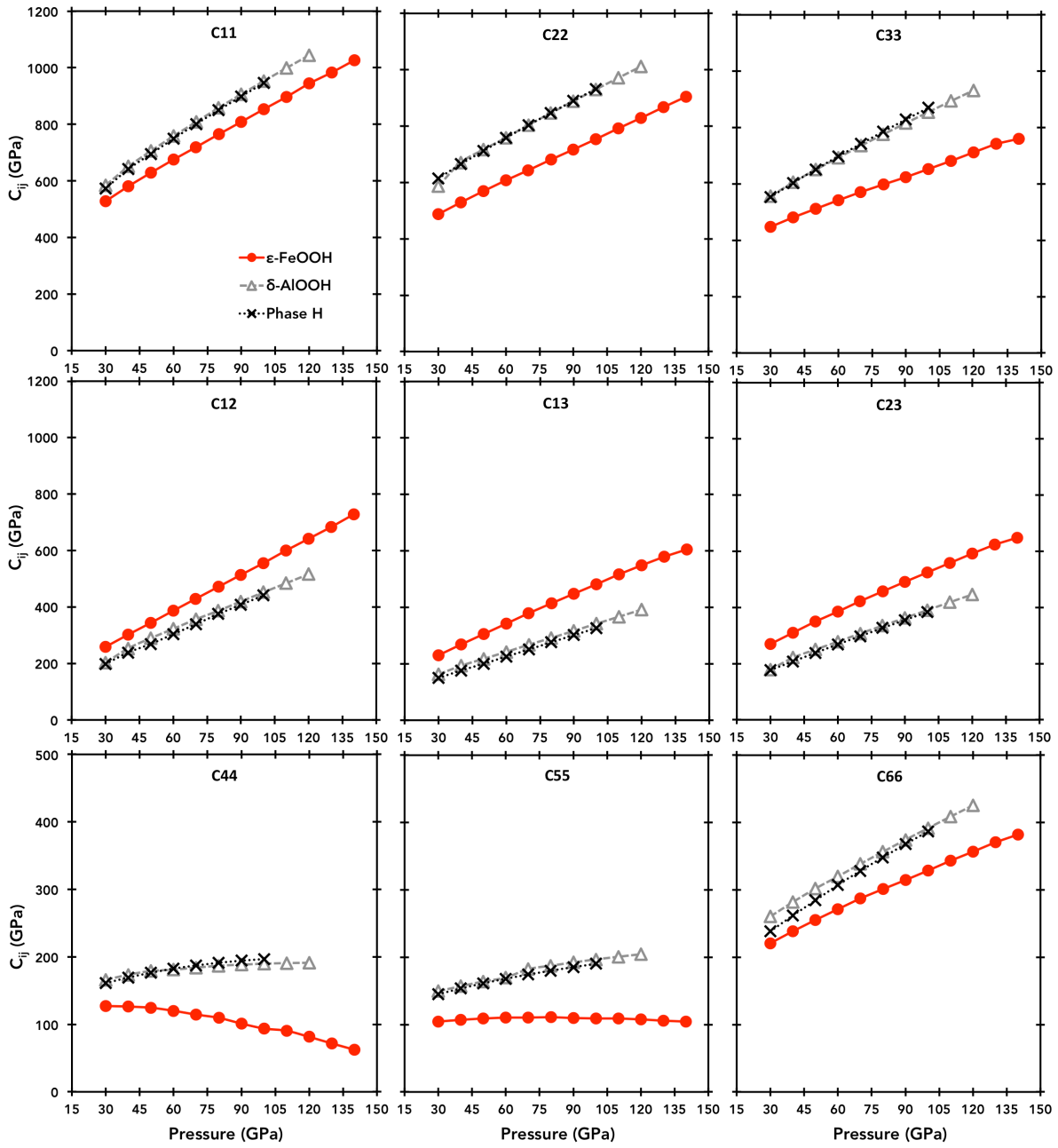

Figure 3.5: Elastic constants of low-spin ferromagnetic ε-FeOOH calculated with self-consistent U parameter (filled circles, this study), δ-AlOOH (open triangles, (Tsuchiya and Tsuchiya, 2009), and phase H (open X-symbols, (Tsuchiya and Mookherjee, 2015)) between 30 and 140 GPa.

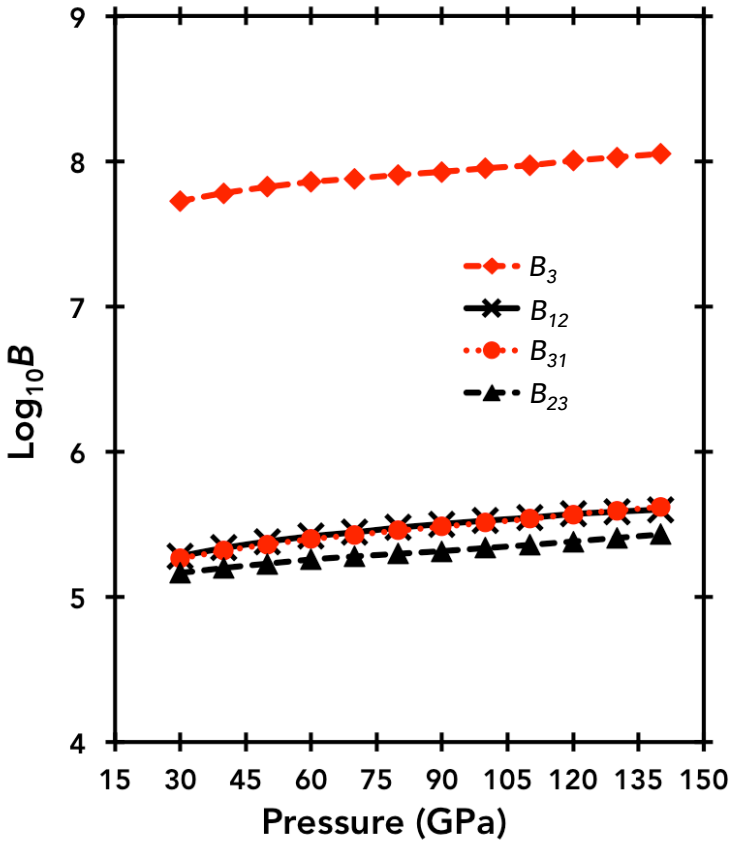

Figure 3.6: Born stability criteria hydrogen-bond symmetric low-spin ferromagnetic ε-FeOOH from 30 to 140 GPa. Mechanical stability of the structure requires each value be greater than zero.

3.3.4 Sound Velocities

Elastic moduli were used to calculate the aggregate compressional velocity (V_P), shear velocity (V_S), and bulk sound speed (V_{BSS}) of ε-FeOOH as a function of pressure (Figure **??**c; Table 3.3). The density, moduli and velocities of ε-FeOOH as a function of pressure are reported in tabulated form in Table B.3. The compressional sound velocity of HC-structure ε-FeOOH increases monotonically with pressure while the shear velocity gradually decreases with increasing pressure. Similarly, the compressional wave velocity of both phase H and δ-AlOOH show strikingly similar pressure dependences, although the average V_P are ∼25 and ∼27% higher, respectively, than that of ε-FeOOH across the same pressure

interval. However, the pressure dependence of the shear wave velocity of ε-FeOOH differs dramatically from those of phase H and δ-AlOOH, despite cation substitution being the only difference between these phases. Both δ-AlOOH and phase H have positive, although slight, pressure dependences in in contrast to the negative pressure dependence of the Fe-endmember (Tsuchiya and Mookherjee, 2015; Tsuchiya and Tsuchiya, 2009). Due to the paired positive pressure dependence of the compressional velocity and negative pressure dependence of the shear wave velocity, the existence of iron-enriched solid solutions from this system may contribute to previously unexplained large-low shear velocity provinces as discussed in Section 3.4 below (Ganero and McNamara, 2008).

In addition to aggregate seismic velocities, the single crystal azimuthal anisotropy for compressional waves (AV_P) and the shear wave polarization anisotropy (AV_S) were determined for ε-FeOOH as a function of pressure using the formalism of (Mainprice, 1990), such that:

$$AV_P = \frac{V_{Pmax} - V_{Pmin}}{\langle V_P \rangle} \times 100 \tag{3.2}$$

$$AV_S = \frac{V_{Smax} - V_{Smin}}{\langle V_S \rangle} \times 100 \tag{3.3}$$

As shown in Figure 3.8, ε-FeOOH exhibits substantial shear wave polarization anisotropy

Table 3.3: Density, Hill averages of bulk moduli (K), shear moduli (μ), and sound velocities at 60 and 90 GPa for ε-FeOOH (This Study), δ-AlOOH (Tsuchiya and Tsuchiya, 2009), and $MgSiO_4H_2$ (Tsuchiya and Mookherjee, 2015).

	FeOOH		AlOOH		Phase H	
P (GPa)	60	90	60	90	60	90
ρ (g/cm^3)	6.055	6.428	4.204	4.476	4.202	4.481
K (GPa)	448.2	556.2	431.7	532.3	415.0	519.6
μ (GPa)	138.3	137.4	219.7	243.8	203.4	221.6
V_S (km/s)	4.78	4.62	7.23	7.38	6.99	7.11
V_P (km/s)	10.22	10.73	13.13	13.84	12.82	13.56
V_ϕ (km/s)	8.60	9.30	10.13	10.91	9.97	10.79

that increases with increasing pressure. The degree of shear wave anisotropy in the iron end-member (ε-FeOOH) is similar to, although higher, than previously reported values for phase H and δ-AlOOH (Tsuchiya and Mookherjee, 2015) (Figure 3.8a). The single crystal shear wave anisotropy of ε-FeOOH is horizontally polarized, i.e., the horizontally polarized shear waves (S_H) are larger than vertically polarized shear wave (S_V). This S_H>S_V anisotropy occurs in ε-FeOOH along both *a*- and *b*-axes, enabling significant shear wave polarization regardless of rotation along the *c*-axis (Figure 3.8b). As such, this significant shear wave polarization would be geophysically significant in conjunction with lattice-preferred orientation (LPO), with considerable flexibility in fabric strength. The existence of iron-rich solid solutions from the FeOOH–AlOOH–$MgSiO_4H_2$ system at the base of the lower mantle could contribute to the S_H>S_V polarization which is seismically observed in that region (Romanowicz and Wenk, 2017). If seismic anisotropy at the base of the mantle is due to LPO in this system, neither partial melting (Williams and Garnero, 1996) nor sustained high strains needed to maintain anisotropy from shape-preferred orientation (SPO) would need to be invoked to explain the observed seismic phenomena.

3.4 Discussion

Increasingly advanced seismic observations, particularly recent tomographic work, have provided evidence that the Earth's mantle is far more heterogeneous than previously believed (Lekic et al., 2012). Among the observed heterogeneities are pair of continent scale regions in the Earth's mantle, thousands of kilometers across and likely hundreds of kilometers high, which are seismically distinct from the surrounding mantle material (Ganero and McNamara, 2008). These regions, dubbed large low-shear velocity provinces (LLSVPs), are detectable by their increased density and decreased shear-wave velocities, and are sharply defined, implying a geochemical rather than solely thermodynamic origin. Since their observation, several potential explanations have been proposed including thermal plumes (Thompson and Tackley, 1998), iron-rich melts (Zhang et al., 2016), and variable oxidation (Gu et al.,

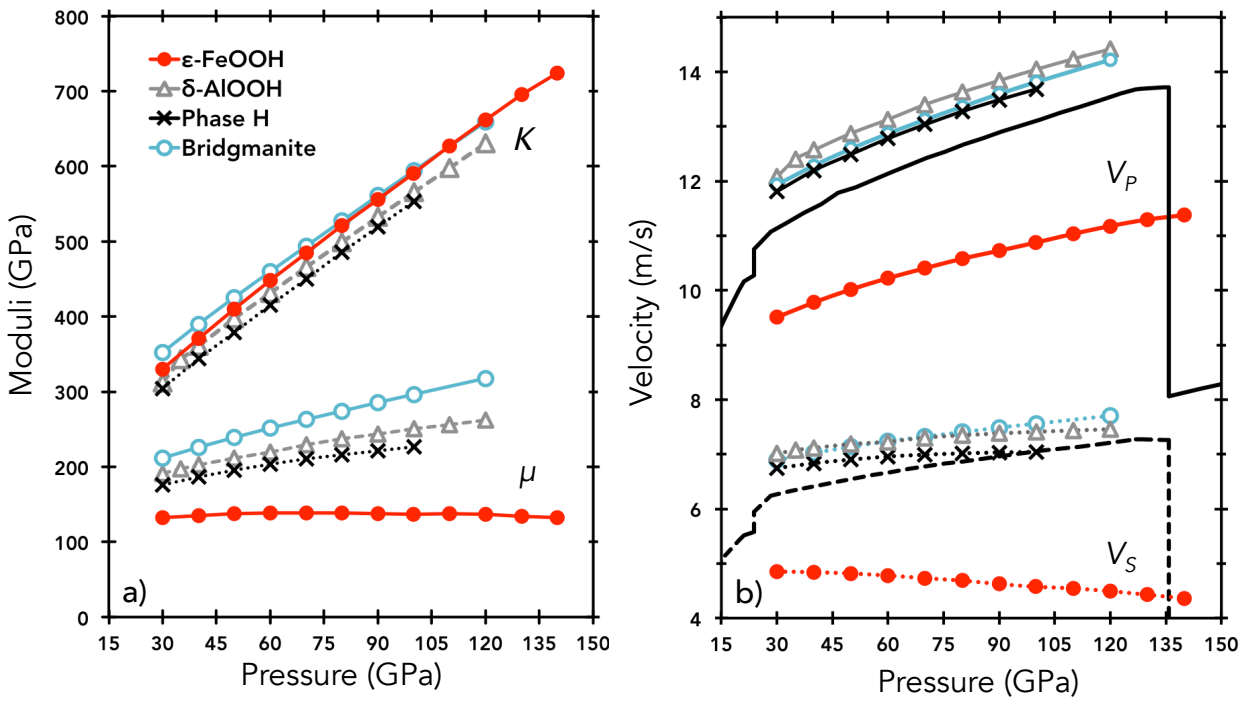

Figure 3.7: Comparison of the elastic properties of ε-FeOOH, δ-AlOOH, phase H, and $MgSiO_3$ bridgmanite as a function of pressure, including (a) bulk moduli (solid lines) and shear moduli (dashed lines), and (b) aggregate compressional (solid lines) and shear wave velocities (dotted lines). All values plotted are 0 K values excluding those of PREM. Phase H and δ-AlOOH literature data from (Tsuchiya and Mookherjee, 2015) and (Tsuchiya and Tsuchiya, 2009) respectively, and bridgmanite data is from (Wentzcovitch et al., 1996).

2016), but additional mineral physics investigations are needed to evaluate the stability and material properties of candidate materials at lower mantle conditions to find a robust answer to this mystery.

As the most abundant mineral of the lower mantle, bridgmanite ($MgSiO_3$-perovskite) is thought to largely dictate the material properties of this expansive region of the Earth. Although the thermoelastic properties of the FeOOH–AlOOH–$MgSiO_4H_2$ solid solution have yet to be evaluated, the properties of volumetrically dominant bridgmanite have been calculated (Wentzcovitch et al., 1996). This allows for the comparison of 0 K ε-FeOOH material properties with the material properties of 0 K bridgmanite, with the assumption that observed differences scale proportionally with temperature for the three endmembers of the solid solution and Mg-endmember bridgmanite. This is a significant assumption, as it is not

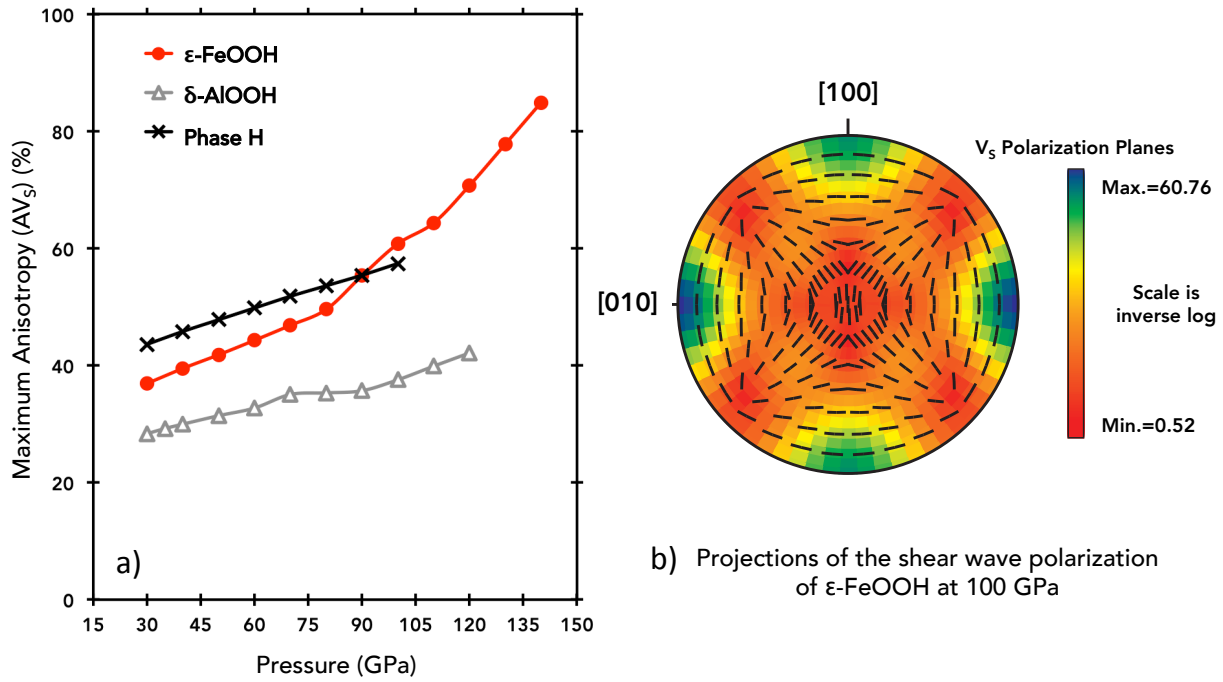

Figure 3.8: (a) Comparison of the shear wave polarization anisotropy (AV_S) of ε-FeOOH, δ-AlOOH, phase H as a function of pressure, and (b) Lambert equal-area upper-hemisphere projection of the shear wave polarization (AV_S) of ε-FeOOH generated using software by (Mainprice, 1990). Black lines indicate the polarization planes of the fast shear wave (V_{Smax}).

known to what extent hydrogen incorporation effects the high-temperature extrapolation of the properties of this solid solution to geotherm conditions, including thermoelasticity or anharmonicity. As shown in Figure 3.7c, the compressional and shear-wave velocities of δ-AlOOH and $MgSiO_4H_2$ do not dramatically differ from that of bridgmanite, but the velocities of ε-FeOOH do. Specifically, the V_P of ε-FeOOH is reduced compared to bridgmanite by a near-constant margin ($21.0 \pm 0.5\%$) while the V_S deviates progressively from an initial reduction of 30% at 30 GPa to a reduction of 44% by CMB pressure. Due to this pronounced difference, less than 1 vol.% of FeOOH is needed in order to reproduce the ~0.27% V_S reduction characteristic of LLSVPs (Ganero et al., 2016). Future high-temperature experiments and molecular dynamics calculations could aid in assessing the validity of the necessary assumption that elastic properties scale consistently with temperature across phases.

In the evaluated ternary FeOOH–AlOOH–$MgSiO_4H_2$ system, ε-FeOOH is anomalous in

the negative pressure dependent behavior of its shear velocity. The addition of similar vol.% amount of δ-AlOOH or $MgSiO_4H_2$ has little impact on the V_S of bridgmanite. While it is unlikely that large regions of endmember ε-FeOOH exist in the deep Earth, regions of iron-enriched, hydrated rock assemblages may be prevalent. And since only small vol.% of FeOOH are needed to mimic the shear wave velocity reductions of LLSVPs, it is plausible that iron enriched solid solutions from the FeOOH–AlOOH–$MgSiO_4H_2$ system contribute to the observed seismic properties of large low-shear velocity provinces in the Earth's lower mantle. These intermediate compositions would bear a seismic signature similar to that of LLSVPs, and the thermodynamic (i.e., P-T) stability of the phases are likely enhanced by the addition of aluminum, which has been experimentally shown to substantially increase the stability of phase H (Nishi et al., 2014; Ohira et al., 2014; Panero and Caracas, 2009). Additionally, the horizontally polarized shear wave anisotropy of ε-FeOOH implies that iron-rich solid solutions from the FeOOH–AlOOH–$MgSiO_4H_2$ system, exhibiting LPO in which the c-axis is vertically aligned due to the strong shear stresses at the CMB, could contribute to the seismically observed $S_H > S_V$ polarization at the base of the mantle (Romanowicz and Wenk, 2017).

3.5 Conclusions

We have investigated the structural properties of low-spin ε-FeOOH up to core-mantle boundary pressure. An abrupt change in the structural parameters of ε-FeOOH at 10-20 GPa indicates a second-order phase transition due to pressure-induced hydrogen bond symmetrization. While the calculated pressure of hydrogen bond symmetrization occurs below prevailing estimates of the stability of the low-spin phase, it is important to nevertheless study the influence that hydrogen-bond symmetrization has on the bulk properties of minerals. These findings are in contrast to those of Gleason et al. (2013), who report a hydrogen bond symmetrization coincident with the high→low spin transition. Rather, it is our finding that hydrogen bonds of ε-FeOOH are symmeterized tens of GPa in advance of this spin

transition. In this case hydrogen bond symmetrization corresponded to a change in the equation of state of the bulk material, a change in the elastic behavior, and a change in the electronic density of state. Determining the high-pressure properties of hydrous phases such as ε-FeOOH is a critical step to future studies of more complex systems. Additionally, systematically describing the influence of proton behavior on seismic observables such as density and sound speeds may allow us to better constrain the quantity and location of water in the lower mantle.

The elasticity of the hydrogen-bond symmetric low-spin ferromagnetic ε-FeOOH was determined from stress-strain relations up to core-mantle boundary pressure. The bulk (κ) and shear (μ) moduli, and sound velocities (V_P, V_S) of the HC phase were calculated from these elastic constants and compared against those of the Preliminary Reference Earth Model (PREM) and 0K bridgmanite. In comparison to different compositions with which it is isostructural and likely to form a solid solution (i.e., phase H and δ-AlOOH), ε-FeOOH is anomalous in regards to the negative pressure dependence of its shear wave velocity. Using bridgmanite as a well-studied proxy for the sound velocities of the bulk lower mantle, it was determined that FeOOH–AlOOH–$MgSiO_4H_2$ solid solutions containing between 0.6 and 0.9 vol.% ε-FeOOH would reproduce the observed reduced shear wave velocities characteristic of large low shear velocity provinces. The addition of ε-FeOOH in these regions may also help explain the elevated density characteristic of LLVPs (Figure B.1). And because ε-FeOOH exhibits significantly shear wave polarization anisotropy, these same iron-rich solid solutions could also help explain seismically observed to the $S_H > S_V$ anisotropy in this region of the deep Earth (Romanowicz and Wenk, 2017).

CHAPTER 4

EXPERIMENTAL EVALUATION OF ϵ-FeOOH AT HIGH PRESSURE

4.1 Introduction

At moderate-pressures (>6 GPa) goethite (α-FeOOH), a widespread iron oxy-hydroxide, transforms into ε-FeOOH, an orthorhombic (space group $P2_1nm$, Z = 2) phase composed of edge sharing FeO_6 units that are closely packed along the c-axis, with hydrogen atoms occupying the channels between these close-packed octahedra (Bendeliani et al., 1972; Pernet et al., 1975; Bolotina et al., 2008). At increased pressure, ε-FeOOH undergoes pressure-induced hydrogen bond symmetrization resulting in a second order phase transition that allows ε-FeOOH to form a solid-solution with δ-AlOOH and phase H ($MgSiH_2O_4$), creating a viable hydrogen reservoir with P-T stability extending from lower mantle conditions to those of the core-mantle boundary (CMB) (Sano et al., 2008; Nishi et al., 2015), although the pressure at which this transition occurs remains contested (Gleason et al., 2008; Xu et al., 2013; Thompson et al., 2017). Hydrogen bond symmetrization is the process by which the hydrogen in an asymmetrical O—H···O bonding unit becomes centered with respect to the two oxygens with increased pressure, as the longer hydroxyl bond compresses more rapidly than the shorter but stiffer hydrogen bond. Once the hydrogen bond is 'symmetrized', the two donor-acceptor distances are equivalent, and this shift in charge balance can lead to additional, subtle structural changes. In ε-FeOOH, the FeO_6 octahedra shift from a slightly offset position to a centered one along the two-fold axis, leading to an increase in symmetry from $P2_1nm$ to $Pnnm$ (Sano-Furukawa et al., 2009) (Figure 3.1). Similarly, proton disorder in which both hydrogen and iron atoms are disordered over symmetric positions on the two-fold axis may also produce ε-FeOOH with $Pnnm$ symmetry (Bolotina et al., 2008).

In addition to the previously described $P2_1nm \rightarrow Pnnm$ transition, ε-FeOOH reportedly undergoes a high spin (HS) to low spin (LS) transition, determined on the basis of X-ray

diffraction (XRD) and X-raw emission spectroscopy (XES) experiments (Gleason et al., 2008). The XES results from this earlier study are indicative of a HS $\rightarrow$ LS transition initiated at $\sim$40 GPa and completed at $\sim$60 GPa. Using XRD, the authors determined a coincident volume collapse (11%) at $\sim$54 GPa, which they attribute to hydrogen bond symmetrization. Yet, previous studies have reported similar volume reductions due to HS $\rightarrow$ LS transitions without invoking hydrogen bond symmetrization (Speziale et al., 2005; Lin et al., 2005a). In this study we present experimental evidence of two distinct transitions in ε-FeOOH in the explored pressure range (0-70 GPa): a low-pressure (17.5 GPa) transition, possibly connected to hydrogen bond symmetrization and a high-pressure transition at 45 GPa, which is likely connected the the previously observed spin transition in this phase.

4.2 Methods

Synthesis of ε-FeOOH for this study was performed by Akio Suzuki, and is described in Suzuki (2010). The high pressures necessary for this study were achieved by compressing ε-FeOOH samples using symmetric-type diamond anvil cells (DACs) with 250 μm culet type II diamonds. Seventy micron diameter sample chambers were laser ablated into stainless steel gaskets pre-indented to $\sim$22 GPa. Powdered ε-FeOOH, kept in a desiccator prior to loading, was pressed into platelets $\sim$1-3 μm thick and $\sim$30 microns in diameter. Compressed ε-FeOOH platelets were loaded into the sample chamber, utilizing either $\sim$10 μm thick platelets of KBr or gas-loaded Ne as pressure medium, reducing pressure gradients within the sample. Neon was loaded as a pressurized gas at the Advanced Photon Source using the COMPRES/GSECARS gas-loading system Rivers et al. (2008) or at Advanced Light Source and also acted as a secondary pressure standard. Pressures were determined via *in situ* monitoring of the R_1 luminescence line (Mao et al., 1978) of 2-3 ruby grains placed in the sample chamber, with errors reflecting the larger of either standard deviations or 3%.

Fourier transform infrared (FTIR) spectra in this study were collected using both synchrotron and globar sources. Synchrotron experiments were performed at the 1.4.3 beam-

line of the Advanced Light Source at Berkeley Laboratory using a Bruker IFS/66v FTIR spectrometer with custom microscope and HgCdTe detectors. Offline experiments were performed at the National Synchrotron Light Source II at Brookhaven National Laboratory using a Bruker Vertex 80v spectrometer and Hyperion 2000 microscope. All FTIR spectra presented here reflect a spectral resolution of 4 cm^{-1}, a measured wavelength range of 500 to 8000 cm^{-1}, and were recorded as 1024 or 512 scans. PeakFit (Systat Software) was used for background subtraction and to obtain precise absorption peak positions using a least-squares refinement.

Optical absorption measurements were collected at the University of Chicago using a 0.3 meter focal length Princeton Instruments SP-2300i spectrograph. Incident light (I) was generated with a tungsten filament bulb and was measured through the pressure medium (KBr) only. Transmitted light (I_0) was collected after it had passed through both the sample (ε-FeOOH) and pressure medium. Background samples were measured two ways: (1) with the light source off to determine the extent of scattered light, and (2) with the light source on but the measurement collected $\sim$ 50 μm from the sample chamber on the opaque, stainless steel gasket. Absorption determinations using both background measurements were comparable but the results presented here used background measurements with the light source off to avoid potential over-correction leading to exaggerated values of sample absorption. Interference fringes in all absorbance spectra were reduced mathematically in DatLab.

Room temperature X-ray diffraction experiments were performed at beamline 13-ID-D (GSECARS) at the Advanced Photon Source, Argonne National Laboratory. Beamline 13-ID-D utilizes a monochromatic incident X-ray beam (λ= 0.3344) of 3 μm by 4 μm at full-width at half-maximum of the focused spot. Sample-to-detector distances and tilt were calibrated using 1-bar diffraction of LaB_6. Diffraction patterns were integrated to produce 2Θplots using DIOPTAS Prescher and Prakapenka (2015), and the resultant integrated patterns were fit to determine lattice parameters as a function of pressure PeakFit (Systat Software). Individual peaks were fit to single Gaussian curves and unresolved overlapping

peaks were not used in the calculation of lattice parameters.

4.3 Results and Discussion

4.3.1 Infrared spectroscopy

Room temperature infrared spectra were collected at ambient pressure and at regularly increasing pressure intervals up to ∼60 GPa. While the O-H stretching region presents as a broadband feature, consistent with previously reported spectra of low pressure-polymorphs of FeOOH (e.g., Williams and Garnero 1996; Kagi et al. 2008), there are three distinct absorption bands which were identified as O-H bending vibrations (Figure 4.1) based on comparison to similar structures (Williams and Garnero, 1996; Mashino et al., 2016; Pinney and Morgan, 2013). Qualitatively the spectrum of ambient pressure ε-FeOOH bears a striking similarity to that of $P2_1nm$ β-CrOOH, with which ε-FeOOH is expected to be iso-symmetric (Jahn et al., 2012). Spectra at each pressure step were evaluated to determine the frequency shifts in the O-H bending and as a function of pressure (Figure C.1).

With increased pressure the broadband O-H stretching region (2600-3100 cm^{-1}) further broadens and shifts to lower wavenumbers (Figure C.1b). Unfortunately, the increased breadth of the O-H stretching feature, and it's increased proximity to the diamond absorption region, prevents tracking this pressure dependence of this feature above ∼17.5 GPa. Although the O-H stretching feature could only be monitored over a limited pressure range, at low pressures a negative frequency shift pressure dependence was clearly observable. This behavior is consistent with eventual hydrogen bond symmetrization in this phase, although there is insufficient data to predict the pressure at which this will occur. Additionally, it isn't feasible to predict the pressure of hydrogen bond symmetrization based on the 1-bar frequency of the OH-stretching band as has been previously done in other phases (Thompson et al., 2016a), as the relationship between the 1-bar stretching frequency and O-H pressure dependence is poorly understood in ε-FeOOH and similarly structured phases.

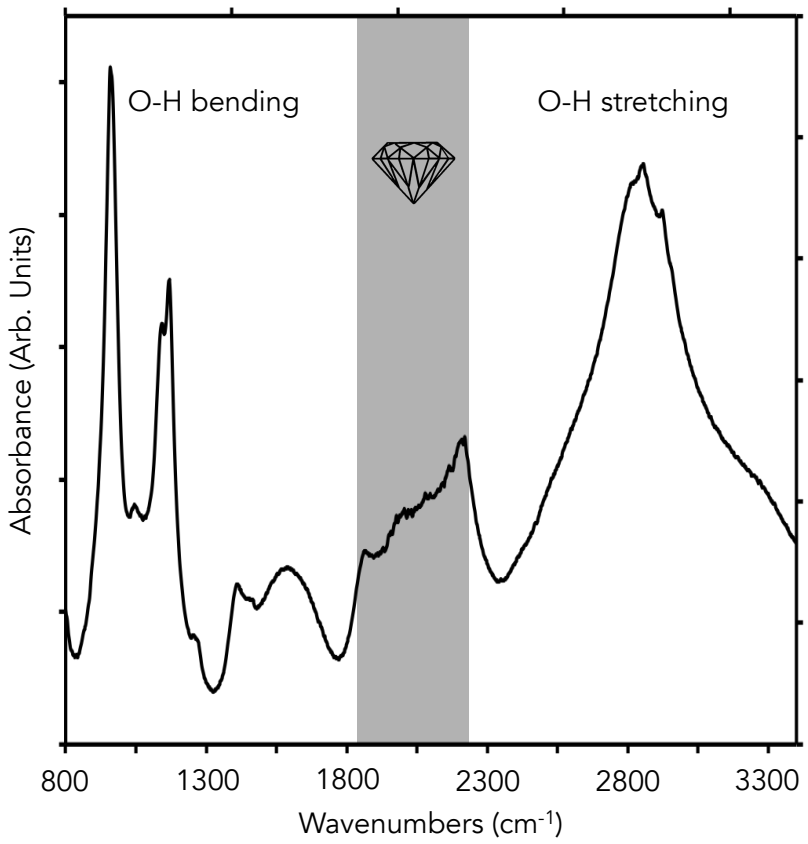

Figure 4.1: Infrared spectra of ε-FeOOH at 0 GPa. The three sharp bands to the left are O-H bending modes, while the broadband feature to the right is the O-H stretching mode. The region marked in grey is the area where diamond absorption has been removed from the spectra.

At ambient pressure the O-H bending vibrations present as sharp features, at 965, 1145, 1175 cm^{-1}. That there are three distinct bands suggests there are three O-H bond orientations within the structure. As with the OH-stretching region, these features also broaden with pressure, with the two higher frequency bands becoming indistinguishable above 17.5±1 GPa (Figure C.1). The lowest frequency stretching band remains distinct to higher pressures, but the pressure dependence of this band changes dramatically above 17.5±1 GPa also (Figure 4.2). The sudden change in this pressure dependence suggests a re-orientation of the O-H bonds, suggestive of either pressure-induced hydrogen bond symmetrization or proton disordering. Lastly, during the course of these IR measurements, a sharp, pressure dependent reduction in transmitted IR signal was observed in ε-FeOOH samples compressed above ∼40

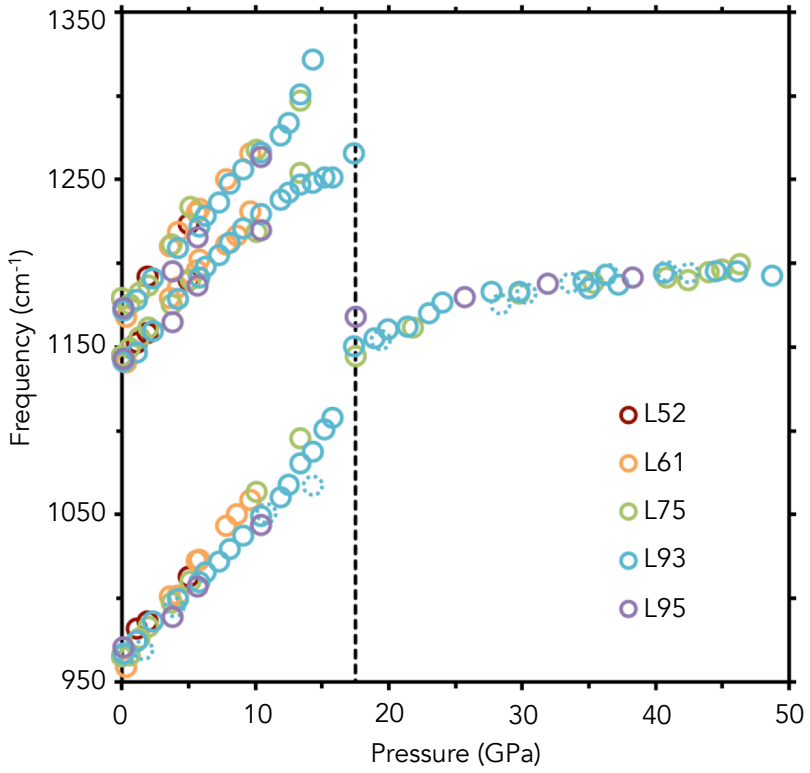

Figure 4.2: Pressure dependence of O-H bending frequencies in ε-FeOOH. A dashed black line indicated the pressure of the proposed phase boundary. Different colored circles indicate different samples, including L52 (red), L61 (orange), L75 (green), L93 (aqua), and L95 (purple).

GPa, as shown in Figure C.2. A color change was observed in the FeOOH region of the samples at this time, as previously translucent dark yellow samples darkened with increased pressure, eventually becoming opaque (black) at ∼40 GPa.

4.3.2 Optical and infrared absorption

As previously mentioned, a pressure-induced color change was observed using optical microscopy during the course of FTIR measurements, in which ε-FeOOH pellets reddened with increased pressure and eventually became opaque to transmitted visible light. To quantify these findings, and track the pressure dependence of the absorption edge at low energies, optical absorption measurements of ε-FeOOH were performed on five samples of ε-FeOOH pellets to pressures up to ∼70 GPa. Representative high-pressure optical absorption spectra

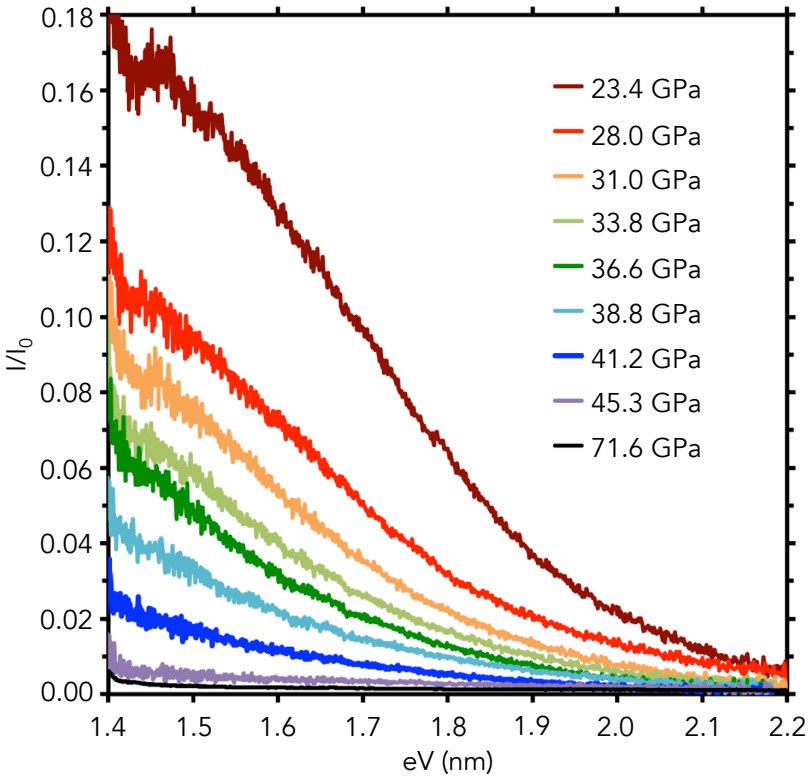

Figure 4.3: Representative optical absorption spectra, indicating the pressure dependent increase in the absorption of ε-FeOOH.

of ε-FeOOH are shown in Figure 4.3 and tabulated absorption data from all optical absorption measurements can be found in Tables C.1, C.2, C.3, C.4, and C.5. As is shown in Figure 4.3, there is a systematic pressure-induced increase in absorption concordant with qualitative observations. Due to variation in sample thickness (d), absorption ($\alpha d = -\ln(I/I_0)$) was scaled such that broadband transmission (I/I_0) was equal for all samples at 10 GPa. Normalized data for all five samples is plotted in Figure 4.4, in which there are two key features. First, each sample underwent a transient minimum in optical absorption between 15-20 GPa before gradually recovering to previous values over the subsequent ~5 GPa. Second, all five samples became opaque in the visible light range probed (1.45 eV to 2.05 eV) above 50 GPa.

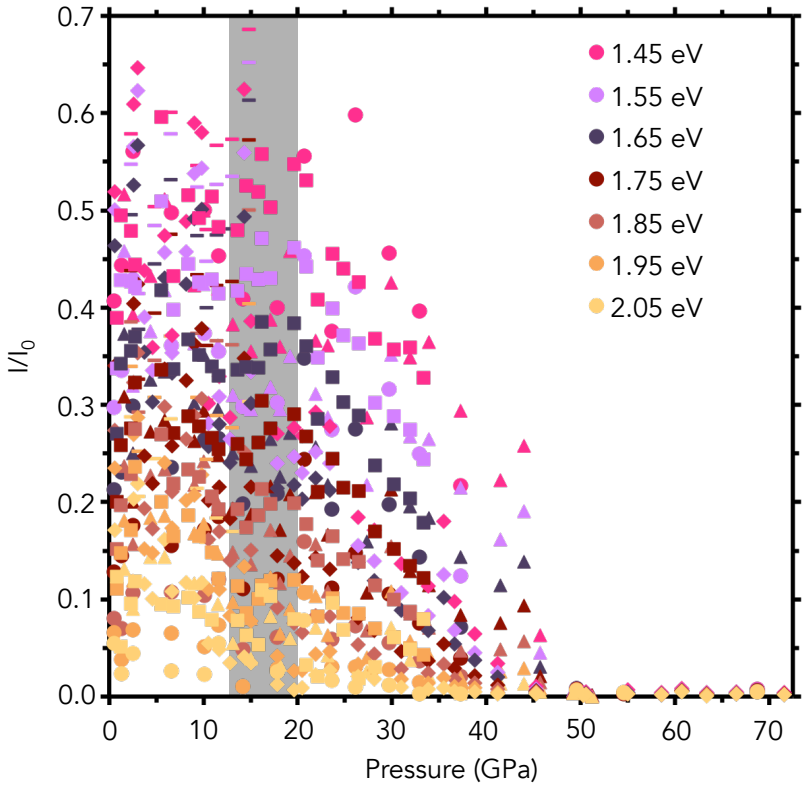

Figure 4.4: Optical absorption data from five samples of ε-FeOOH, each indicated with a different symbol (diamonds, squares, circles, triangles, and horixontal dashes). Here we show the change in the ratio of transmitted light (I) to incident light (I_0) as a function of pressure (X-axis) and the wavelength of the incident light, indicated by color. The shaded grey region indicates the pressure range in which samples undergo a transient minimum in optical absorption.

4.3.3 X-ray diffraction

High-pressure, room-temperature X-ray diffraction (XRD) measurements of ε-FeOOH were used to re-evaluate the phase diagram of this material, as the existing literature exhibits a paucity of V-P data in the mid-pressure range (20-50 GPa) (Gleason et al., 2008; Suzuki, 2010; Gleason et al., 2013; Suzuki, 2016). Using a gas-membrane diaphram to remotely pressurize the DAC between diffraction measurements, we collected diffraction data with far greater pressure resolution than previous studies. As X-ray diffraction inherently relies on electron density, the detection of hydrogen using powder XRD is virtually impossible. The $P2_1nm \rightarrow Pnnm$ transition is primarily defined by the pressure induced symmetrization of

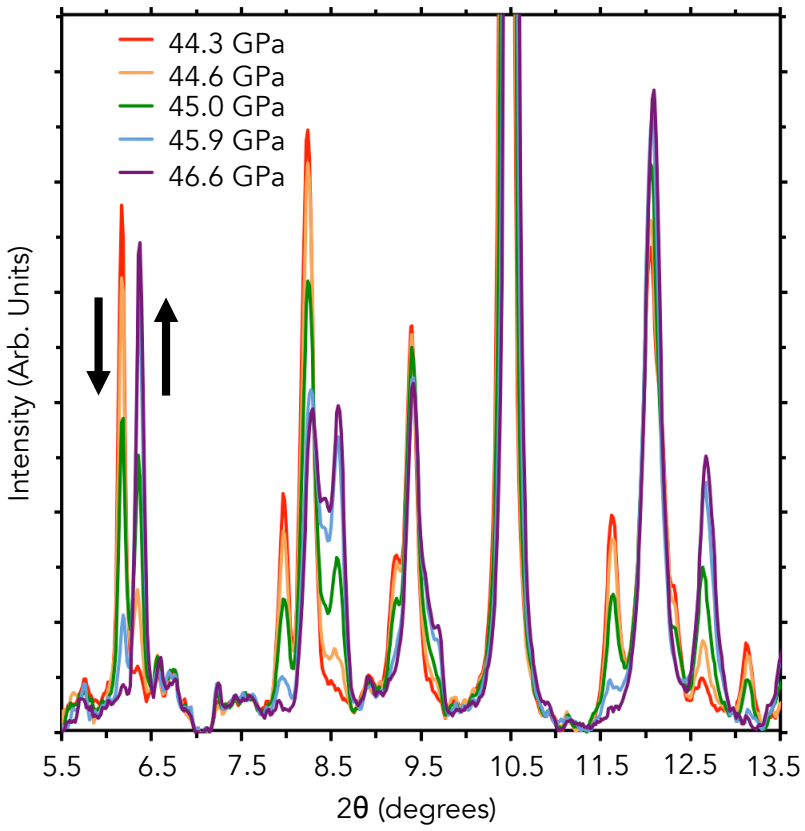

Figure 4.5: Diffraction of ε-FeOOH at five pressure steps: 44.3 GPa (red), 44.6 GPa (orange), 45.0 GPa (green), 45.9 GPa (blue), and 46.6 GPa (purple). A downward black arrow is included to indicate peaks which are disappearing with increased pressure across this interval, and an upward black arrow indicates which peaks are growing in with increased pressure.

the hydrogen bonds, but associated with hydrogen bond symmetrization are subtle changes in the structure and strain accommodation which enable the detection of this transition indirectly (e.g., Thompson et al. 2017). Additionally, XRD data collected up to 75 GPa revealed a second structural transition in ε-FeOOH at ∼45 GPa (Figure 4.5), which is likely linked to the observed changes in FTIR transmission, optical absorption, the observed color change of ε-FeOOH, and the previously reported spin transition in this phase (Gleason et al., 2013).

In the lower pressure interval (0.5-43 GPa) the unit cell volumes of ε-FeOOH were determined using at a minimum, the {110}, {101}, {011}, {020}, {211}, {121}, {220}, {002}, {301}, and {112} hkl peaks. These unit cell volumes and lattice parameters are reported in

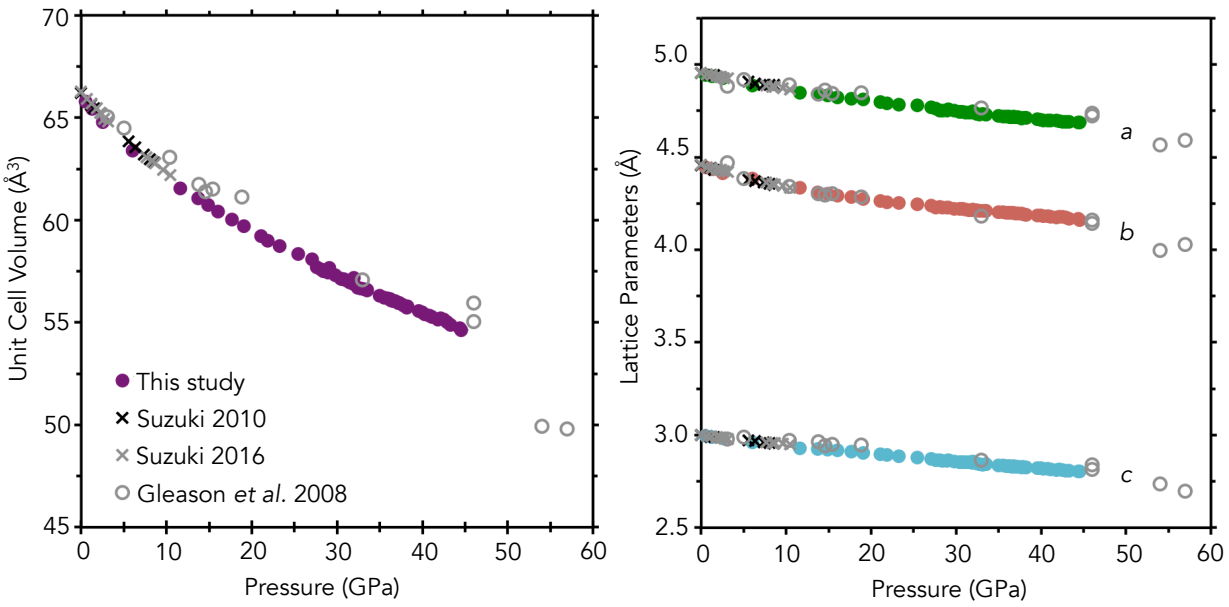

Figure 4.6: (left) V-P relationship and (right) lattice parameters of ε-FeOOH based on XRD measurements. Data includes this study (solid colored circles), Suzuki (2010) (black crosses), Suzuki (2010) (grey crosses), and (Gleason et al., 2013) (grey open circles).

tabulated form in Tables C.6 and C.7 and plotted in Figure 4.6. These lattice parameters were found to be in excellent agreement with the results of Suzuki (2010, 2016), although both lattice parameters and unit cell volumes are intermediate to those of the high- and low-spin structures predicted by the Gleason et al. (2008). On the basis of the Bragg peaks which could be indexed in our sample, the $P2_1nm$ and $Pnnm$ structure can not be distinguished, as we did not identify any peaks which violated the systematic absences characteristic of the $Pnnm$ symmetry ($h + l$ odd for $h0l$, $k + l$ odd for $0kl$). Additionally, based on the findings of Sano-Furukawa et al. (2009), who evaluated the $P2_1nm \rightarrow Pnnm$ transition in iso-structural δ-AlOOH, the volume reduction associated with this second-order transition is likely unresolvable, rendering determinations of this phase boundary on this basis alone dubious. Thus, employing the approach of Sano-Furukawa et al. (2009), we evaluated the ratios of lattice parameters as a means of elucidating the subtle $P2_1nm \rightarrow Pnnm$ transition (Figure 4.7).

The plotted lattice parameter ratios (Figure 4.7) reveal a change in the axial compression

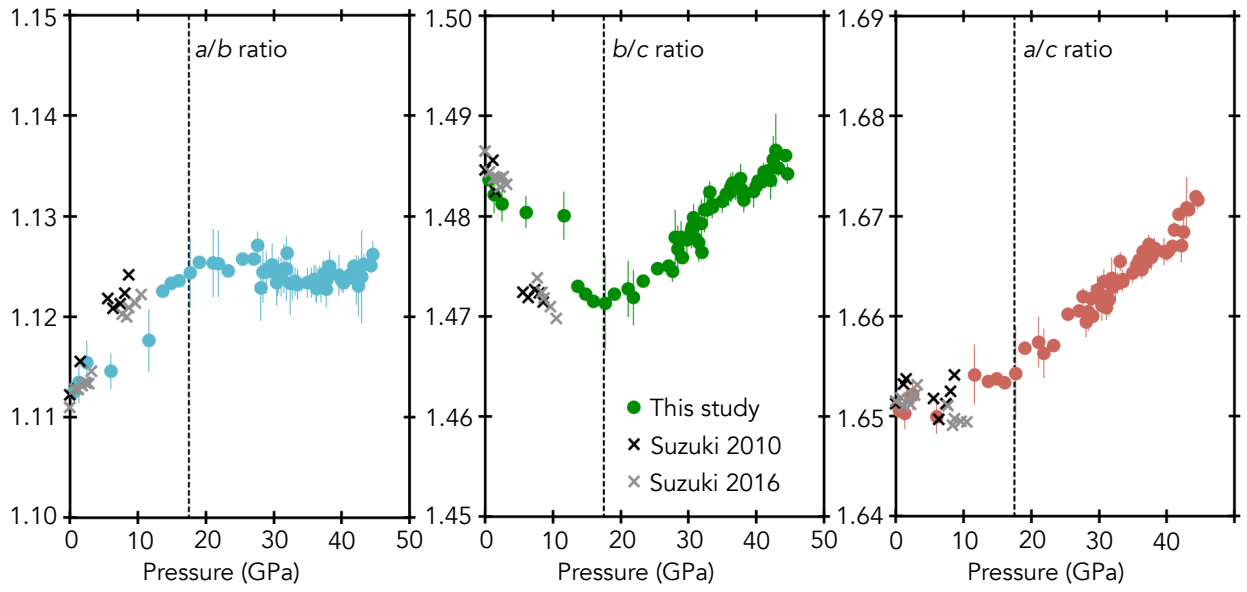

Figure 4.7: Ratios of ε-FeOOH lattice parameters, including (left) a/b ratio, (center) b/c ratio, and (right) a/c ratio. Data from this study are indicated by solid circles, previously published data by Suzuki (2010) and Suzuki (2010) are indicated as black and grey crosses, respectively. The proposed $P2_1nm \rightarrow Pnnm$ boundary is indicated by a black dotted line.

of ε-FeOOH with pressure, and the inflection points evident at 17.5±1 GPa indicate a shift in the accommodation of strain in this system. Similar changes in axial compression have been used previously as an indicator of second-order phase changes (Sano-Furukawa et al., 2009; Kuribayashi et al., 2014). On the basis of these lattice parameter ratios, as well as the previously described changes in the O-H bonding observed using FTIR spectroscopy, we conclude that ε-FeOOH undergoes a second-order phase transition from the $P2_1nm$ to $Pnnm$ structure at 17.5±1 GPa. Yet, plotting Eulerian strain (f) versus the normalized pressure (F_E) across this presumed phase boundary (0.5-43 GPa) revealed no significant discontinuity in the V-P relationship, confirming that any phase transition within this pressure range resulted in a minimal volume reduction (Figure C.3). As such, the V-P data from the entire pressure interval (0.5-43 GPa) was fit to a third-order Birch-Murnaghan (BM) equation of state (Birch, 1978):

$$P(V,T) = 3K_0 f_E \left[\left(1 + 2f_E\right)^{\frac{5}{2}} \left(1 + \frac{3}{2}\left[K_0' - 4\right] f_E\right) \right] \tag{4.1}$$

which relates pressure (P), volume (V), ambient pressure bulk modulus (K_0), and its pressure derivative (K_0') in terms of finite Eulerian strain (f_E):

$$f_E = \frac{1}{2}\left[\left(\frac{V_0}{V}\right)^{\frac{2}{3}} - 1\right] \tag{4.2}$$

which is a measure of the volume compression of a solid relative to its initial volume (V_0), which was treated at a free parameter. Additionally, as the studies of Suzuki (2010, 2016) provide additional V-P data in the low pressure region ($<$ 13 GPa), we fit the combined results from this study and Suzuki (2010, 2016) to obtain equation of state parameters with the most comprehensive data set available. Lastly, we fit the $P2_1nm$ and $Pnnm$ structures separately, combining our results with those of Suzuki (2010, 2016) for the lower-pressure $P2_1nm$ structure. The resultant equation of state parameters from these fittings, as well as previously published results, are reported in Table 4.1. Based on these results, we find that the parameters derived from fitting the combined data set across the the entire pressure range (0-45 GPa) are in reasonable agreement with those reported by Gleason et al. (2008) and Suzuki (2010, 2016). However, fitting V-P data independently above and below the presumed phase transition boundary of 17.5$\pm$1 GPa using a fixed K_0' value of 4, reveals the $Pnnm$ structure has a bulk modulus $\sim$20% higher than that of the $P2_1nm$ ε-FeOOH, in good agreement with the $\sim$19% increase predicted in Chapter 3 (Table 3.2) and in Thompson et al. (2017).

Table 4.1: Experimental Birch-Murnaghan equation of state (EoS) parameters of ε-FeOOH, including ambient-pressure unit cell volume (V_0), ambient-pressure bulk modulus (K_0), and the pressure derivative of the bulk modulus (K_0'). Also included is the pressure range of room-temperature XRD data and the number of V-P data points included in each EoS fitting. Values in parentheses are uncertainties on the last digit.

	Pressure range (GPa)	# Data points	V_0 (Å$_3$)	K_0 (GPa)	K_0'
This study	0.5 to 45	58	65.88(8)	150(4)	5.0(2)
This study	0.5 to 45	58	65.57(6)	170(1)	4 (fixed)
This study, Suzuki (2010, 2016)	0 to 45	79	66.16(4)	140(2)	5.4(2)
This study, Suzuki (2010, 2016)	0 to 45	79	65.90(4)	162.9(9)	4 (fixed)
This study, Suzuki (2010, 2016) ($P2_1nm$)	0 to 16	29	66.14(4)	146(2)	4 (fixed)
This study ($Pnnm$)	18 to 45	50	65.30 (9)	176(2)	4 (fixed)
Gleason et al. (2008)	8 to 17	9	66.3(5)	158(5)	4 (fixed)
Suzuki (2010)	0 to 9	8	66.20(3)	126(3)	10(1)
Suzuki (2016)	0 to 11	13	66.278(6)	135(3)	6.1(9)

4.4 Conclusions

Close evaluation of the high-pressure behavior of ε-FeOOH up to 70 GPa indicates two distinct transitions. A second-order $P2_1nm \rightarrow Pnnm$ phase transition at 17.5±1 GPa was determined on the basis of three observations: (1) a change in the OH-bending modes observed with FTIR spectroscopy, (2) a transient decrease in optical absorption, and (3) a change in axial compressibility evident in the lattice parameter ratios measured using powder XRD. In accordance with the previous work of Sano-Furukawa et al. (2009), this transition my be attributed to either pressure-induced hydrogen bond symmetrization or proton disordering. The pressure at which the $P2_1nm \rightarrow Pnnm$ phase transition occurs is in reasonable agreement with the hydrogen bond symmetrization induced symmetry change previously predicted based on DFT calculations (∼20 GPa, Thompson et al. 2017) but conflicts substantially with the previous findings of Gleason et al. (2013). That earlier study attributed a volume collapse at ∼43 GPa to a hydrogen bond symmetrization induced $P2_1nm \rightarrow Pnnm$ phase transition, but although we also observe a structural transition at this pressure, we interpret this transition as unrelated to hydrogen bonding.

At ∼45 GPa *Pnnm* ε-FeOOH undergoes a second phase transition, which was determined based on three observations: (1) the reduction in FTIR transmission through the sample, (2) the increase in optical absorption, (3) the appearance of new Bragg peaks coincident with the disappearance of observed *Pnnm* peaks. The infrared transmission and optical absorption findings suggest this phase undergoes a significant and relatively rapid reduction in the band gap, as the absorption edge begins to occlude IR transmission at 35 GPa and has swept the visible region by 50 GPa. However, the complete band gap collapse (i.e., metallization) of this phase cannot be established on the basis of these experiments alone. Pressure-induced changes in the band gap are likely linked to the previously reported HS → LS transition in this material, as both phenomenon are tied to changes in the d orbitals of the iron atoms and occur at overlapping pressures. A similar increase in optical opacity linked to a HS → LS

transition has been observed in ferropericlase (Keppler et al., 2007). While it is also possible the bandgap closure and spin transition in ε-FeOOH are unrelated, this does not alter our primary finding that the $P2_1nm \rightarrow Pnnm$ symmetry transition associated with hydrogen bond symmetrization was observed ∼30 GPa below the spin transition pressure reported by Gleason et al. (2013).

Coincident with the electronic transition observed in *Pnnm* is a clear structural transition to an as-of-yet unidentified structure. While the exact symmetry of this phase is still unknown, we can definitively state that this is not the appearance of the high-pressure pyrite structure of FeOOH, which ε-FeOOH is expected to transition to at ∼ 60 GPa (Nishi et al., 2017; Hu et al., 2017, 2016). It is likely this new higher pressure phase is a distortion of the *Pnnm* structure with a volume collapse associated with the previously described electronic transition. Based on our findings, it is unlikely that hydrogen-bond symmetrization is the driver of spin transition in ε-FeOOH, as these transitions are separated by ∼30 GPa. Rather, at high pressure FeOOH undergoes two distinct structural transitions, the first transition at 17.5 GPa is the $P2_1nm \rightarrow Pnnm$ symmetry change caused by a shift in hydrogen bonding at increased pressure, and the second structural transition at ∼45 GPa is tied to changes in the d-orbital occupations of the octahedrally coordinated trivalent iron in this phase.

CHAPTER 5

CALCULATED PROPERTIES OF PYRITE-TYPE (Fe,Al)O_2H

5.1 Introduction

Hydrogen storage and cycling in the deep Earth has profound implications on the chemistry and dynamics of Earth's mantle. Recent literature suggests a likely carrier of hydrogen into the Earth's lower mantle in the solid solution formed by ε-FeOOH, δ-AlOOH, and phase H ($MgSiO_4H_2$) (Ohira et al., 2014; Nishi et al., 2017; Thompson et al., 2017). At high pressure (>170 GPa), δ-AlOOH is predicted to transform into a cubic, pyrite (pyrite-type) structure consisting of an AlO_2 framework (Tsuchiya and Tsuchiya, 2011) with symmetrically bonded interstitial hydrogens (Figure 5.1). An analogous high-pressure phase transition from ε-FeOOH to a pyrite structure has been previously proposed, but the stability, stoichometry, and properties of the resultant phase remains contested (Hu et al., 2016, 2017; Nishi et al., 2017; Liu et al., 2017; Yuan et al., 2018b).

This chapter aims to provide a detailed examination of the stability, structure, and electronic properties of high-pressure pyrite-structure FeO_2H at pressure conditions relevant to the Earth's lower mantle. Importantly, these density function theory (DFT) calculations make use of a self-consistent Coloumbic self-interaction term (U), which enables more accurate prediction of the electronic behavior in 3d transition metals (e.g., Kulik et al. 2006). These findings are presented alongside those of pyrite-type AlO_2H, with which FeO_2H likely forms a solid solution, analogous to the solid solution formed by the lower pressure endmember polymorphs ε-FeOOH and δ-AlOOH. Conversely, no pyrite-type structure of phase H has been reported, although pyrite-type magnesium peroxide (MgO_2) may be stable at lower mantle conditions (Lobanov et al., 2015). The inclusion of aluminum is reported to enhance the P–T stability of similar hydrous phases, including the aforementioned lower-pressure polymorphs of this system (Sano et al., 2008; Ohira et al., 2014; Pamato et al., 2015).

By determining the geophysical properties of both the Fe- and Al- endmembers of the

pyrite-structure (Fe,Al)O_2H solid solution we hope to constrain the behavior of intermediate compositions, and to compare the calculated sound velocities to seismic observations of the deep Earth as in Section 3.3.4. In particular, a recent study suggested that partially dehydrated pyrite-type FeO_2H may explain the shear wave velocity reduction characteristic of Ultra Low Velocity Zones (ULVZs) near the core mantle boundary (Liu et al., 2017). Ultra Low Velocity Zones are seismically distinct regions typically clustered near LLSVPs, which are more numerous but smaller than LLSVPs—extending only 10 to 20 km above the Earth's core–mantle boundary. ULVZs regions are characterized by compressive and shear wave velocity reductions of up to 10% and 30%, respectively, compared to surrounding mantle material, and have morphologies consistent with compositional rather than purely thermal origin (Li et al., 2017; Yu and Ganero, 2018). Due to the geophysical proximity of ULVZs and LLSVPs, and the previously established likelihood that the lower-pressure polymorph of (Fe,Al)OOH contributes to LLSVPs due to the anomalous negative pressure dependence of ε-FeOOH (Section 3.4; Thompson et al. 2017), we re-evaluated the potential for pyrite-type FeO_2H to contribute the velocity reductions characteristic of ULVZs based on the formation of a solid solution [i.e., (Al,Fe)O_2H] rather than partial dehydration.

5.2 Methods

Similar to the methods described in 2.2 and 3.2, *first principles* calculations of high-pressure pyrite-type FeO_2H carried out using Quantum ESPRESSO 4.3.2 were performed using a generalized gradient approximation (GGA) to the exchange-correlation functional (Perdew et al., 1996) with an on-site Coloumbic self-interaction term (U) determined using an internally consistent method (Nishi et al., 2017). A generalized gradient approximation is necessary to accurately describe weak hydrogen bonding (Tsuchiya et al., 2002; Umemoto and Wentzcovitch, 1991) and the determination of an appropriate U value is paramount to accurately describing the electronic structure and stability of iron-bearing phases (e.g., Jang et al. 1994). Optimized structures were determined using damped variable cell shape

molecular dynamics (Wentzcovitch, 1991) from Quantum ESPRESSO (Giannozzi et al., 2009). The effective interaction of core electrons was approximated with previously evaluated norm-conserving pseudopotentials (Troullier and Martins, 1991), with the exception of iron, in which case an ultrasoft pseudopotential was used (Vanderbilt, 1990; Ichikawa et al., 2014). The irreducible Brillouin zone was sampled by a 4×4×4 Monkhorst–Pack mesh (Monkhorst and Pack, 1976) and electronic wave functions were expanded in plane-waves with an energy cutoff of 80 Ry. The effects of larger energy cut-offs and k-point sampling were found to be negligible.

Additional *first principles* calculations of related high-pressure phases ε-FeOOH, α-PbO_2-type FeO_2H, δ-AlOOH and pyrite-type AlO_2H were calculated to enable the determination of high-pressure phase boundaries for comparison to aluminum-endmembers. The details of the low-spin ferromagnetic ε-FeOOH calculation have been previously reported (Thompson et al., 2017). FeOOH polymorphs including distorted-rutile structure α-PbO_2-type (*Pbcn*) FeO_2H, low-spin antiferromagnetic ε-FeOOH, high-spin antiferromagnetic ε-FeOOH, and high-spin ferromagnetic ε-FeOOH were evaluated using a fixed on-site Coloumbic self-interaction term of U=5.0, with irreducible Brillouin zones sampled by a 4×4×4 Monkhorst–Pack mesh and an energy cutoff of 80 Ry. Generalized gradient approximation calculations of δ-AlOOH and pyrite-type AlOOH were performed, sampling irreducible Brillouin zones with a 4×4×4 Monkhorst–Pack mesh and using an energy cutoff of 80 Ry, consistent the methodology of Tsuchiya and Tsuchiya (2011) and with the FeO_2H calculations presented herein. These structures were recalculated using the same norm-conserving pseudopotentials as our FeOOH calculations to enable direct comparison, with the addition of aluminum, for which a projector augmented wave method (PAW) pseudopotential was utilized.

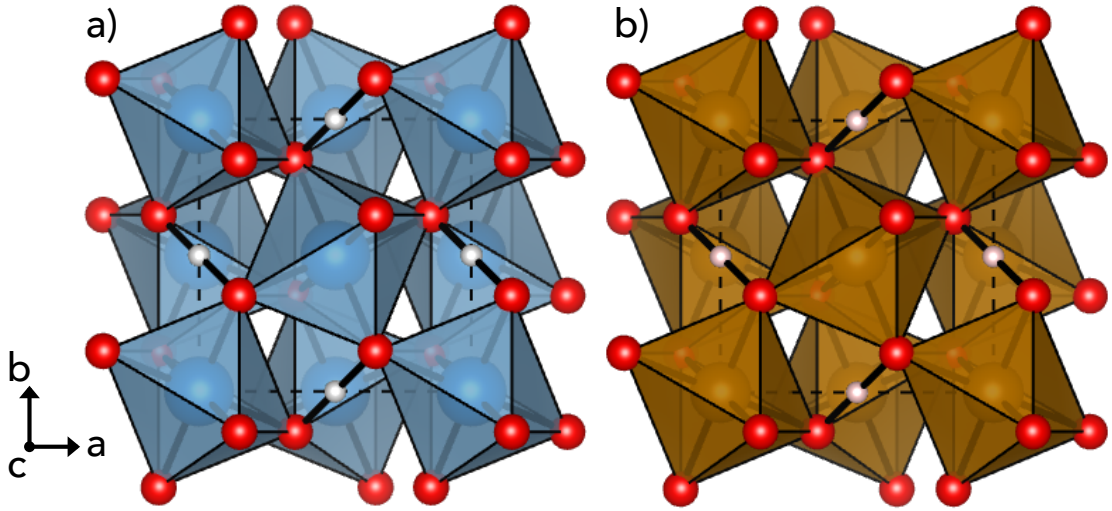

Figure 5.1: Structure (a) AlO_2H and (b) FeO_2H at 60 GPa. Oxygen atoms are red spheres, hydrogen atoms are white spheres, aluminum atoms are blue spheres, and iron atoms are gold spheres.

5.3 Results

5.3.1 Stability

The high-pressure phase relations of ε-FeOOH and pyrite type FeO_2H were determined quantitatively using a generalized gradient approximation plus self-consistent Hubbard U method (GGA+U), on the basis of least enthalpy (Figure 5.2). Three polymorphs of FeOOH are potentially stable at the pressures relevant to the lower mantle; low-spin ferromagnetic ε-FeOOH at moderate pressure and either cubic or orthorhombic pyrite-type FeO_2H at high pressure (Figure 5.2). Additional polymorphs of FeOOH including δ-PbO_2 structure FeO_2H, low-spin antiferromagnetic ε-FeOOH, high-spin antiferromagnetic ε-FeOOH, and high-spin ferromagnetic ε-FeOOH were evaluated for potential stability but the enthalpies of these structures were found to be significantly higher in the pressure range explored (30-140 GPa). As such, the phase transition in the FeO_2H system likely parallels that of the AlO_2H system, namely low-pressure goethite (α-FeOOH, isomorphous with diaspore, α-AlOOH) transforms

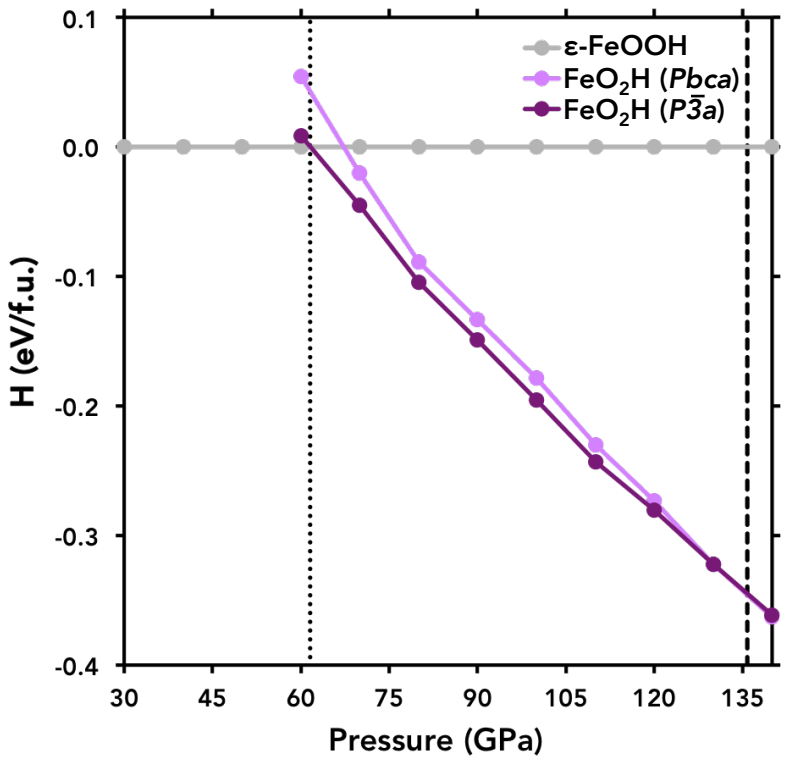

Figure 5.2: Calculated relative enthalpies of FeO_2H from 30 to 140 GPa. Light grey symbols indicate low-spin ferromagnetic ε-FeOOH, light purple indicate orthorhombic (*Pbca*) structure FeO_2H, and dark purple symbols indicate ($Pa\bar{3}$) FeO_2H. The black dotted line indicated the pressure above which pyrite-type FeO_2H is the stable structure, and the dashed black line indicates core-mantle boundary pressure.

first to ε-FeOOH (isomorphous with δ-AlOOH) with moderate pressures and subsequently transforms to a pyrite structure at the pressures relevant to the base of the Earth's mantle.

As previously mentioned, depending on the d-orbital occupation of the iron in FeO_2H, two potential pyrite-type structures are stabilized at high pressure. This difference, fundamentally linked to the electronic structure of iron, is explored in greater detail below, but a spin-polarization density map (ρ_{up}–ρ_{down}) is included in Figure D.1 to enable the reader to visualize the influence of iron's electronic structure on the crystalline symmetry of the optimized structures. Of these two high-pressure pyrite polymorphs, the cubic structure ($Pa\bar{3}$), space group No. 205) has a slightly lower enthalpy up to 120 GPa and is therefore the stable structure at these pressures. However, the enthalpy difference is slight, with an enthalpy crossover occurring at ∼130 GPa, leading to the orthorhombic pyrite structure (*Pbca*, space

group No. 63) exhibiting slightly lower enthalpy at 140 GPa. Despite this crossover, at the high temperatures relevant to the Earth's lower mantle, spin polarization disordering likely occurs, leading to preferential stabilization of the cubic phase up to core-mantle boundary pressures. Additionally, the formation of (Fe,Al)O_2H solid solutions should reduce the relative stability of the orthorhombic structure, as its formation is predicated on spin ordering. Lastly, it warrants mention that due to variability in the algorithm of different versions of Quantum Espresso, larger smearing values may be required to converge the cubic structure. However, due to the reduced relative enthalpy of the cubic structure over most of the pressure range of the lower mantle and experimental confirmation of the cubic structure (Hu et al., 2016, 2017; Nishi et al., 2017), the properties of cubic FeO_2H are presented here to enable direct comparison to the cubic AlO_2H.

Regardless, the ε-FeOOH → FeO_2H pyrite phase transition occurs at significantly lower pressure (∼65 GPa, Figure 5.2) than the analogous δ-AlOOH → AlO_2H pyrite phase transition has been predicted to occur (∼170 GPa) (Tsuchiya and Tsuchiya, 2011). Notably, this AlOOH → AlO_2H pyrite phase transition is predicted to occur at even higher pressure using the pseudopotentials employed here (∼195 GPa). This suggests that solid solutions from the (Fe,Al)O_2H system undergo a structural phase transition between 70-195 GPa, and that the precise transition pressure is compositionally dependent. For example, a 1:1 ratio of iron to aluminum ($Al_{0.5}Fe_{0.5}O_2H$), would undergo the phase transition to the pyrite structure at pressures approximating those at the core-mantle boundary (CMB), while solid solutions containing greater than 50% Fe by mole would transition to the pyrite structure at shallower depths. Ultimately these findings suggest that solid solutions from the (Fe,Al)O_2H system exist as a minor mantle phase capable of ushering iron and hydrogen to the core-mantle boundary.

5.3.2 Electronic properties

Cubic pyrite ($Pa\bar{3}$) structured FeO_2H were optimized using a standard t_{2g} d-orbital configuration, while orthorhombic pyrite-type FeO_2H is the optimized structure resulting from any non-t_{2g} initial d-orbital occupation. Given the disparities in the electronic properties and spin-polarization densities of the two pyrite-type FeO_2H polymorphs, it is evident that the d-orbital configuration is the primary determinant of the optimized FeO_2H symmetry. In the case of the orthorhombic (*Pbca*) structure, the spin polarization isosurfaces are oriented such that they are in close proximity to the hydrogen atoms, creating strong repulsive forces and producing an orthorhombic Jahn-Teller distortion (Figure D.1). Conversely, in the cubic ($Pa\bar{3}$) structure, the spin polarization isosurfaces are oriented antithetical to the hydrogen and iron atoms, with no resultant distortion (Table D.2). Additionally, in both structures the densities of state at all explored pressures (70-140 GPa) exhibit nonzero bandgaps indicative of insulator behavior. This finding contrasts the reported electronic properties of FeO_2 (Jang et al., 1994), in that neither pyrite-type FeO_2H undergoes a metal-insulator transition (MIT) in the pressure range relevant to the Earth's mantle.

5.3.3 Structure and equation of state

Structural parameters of pyrite-type FeO_2H and AlO_2H are plotted in Figure 5.3, with lattice parameters and unit cell volumes also reported in Table D.1. As shown in Figure 5.3a the b-lattice of the *Pbca* FeO_2H structure evolves steadily with pressure, such that both the b/a and b/c ratios steadily increase across the 60-140 GPa pressure interval. Additionally, the length and pressure-evolution of the a-lattice of the ($Pa\bar{3}$) FeO_2H structure approximates that of the *Pbca* b lattice parameter. The unit cell volumes (Figure 5.3b) of the orthorhombic and cubic structures of FeO_2H are quite similar, the orthorhombic unit cell being $\sim$0.3-0.4% smaller than its cubic structure counterpart. The difference in volume between $Pa\bar{3}$ FeO_2H and AlO_2H is more substantial, with the Al-endmember $\sim$4-5% smaller than FeO_2H.

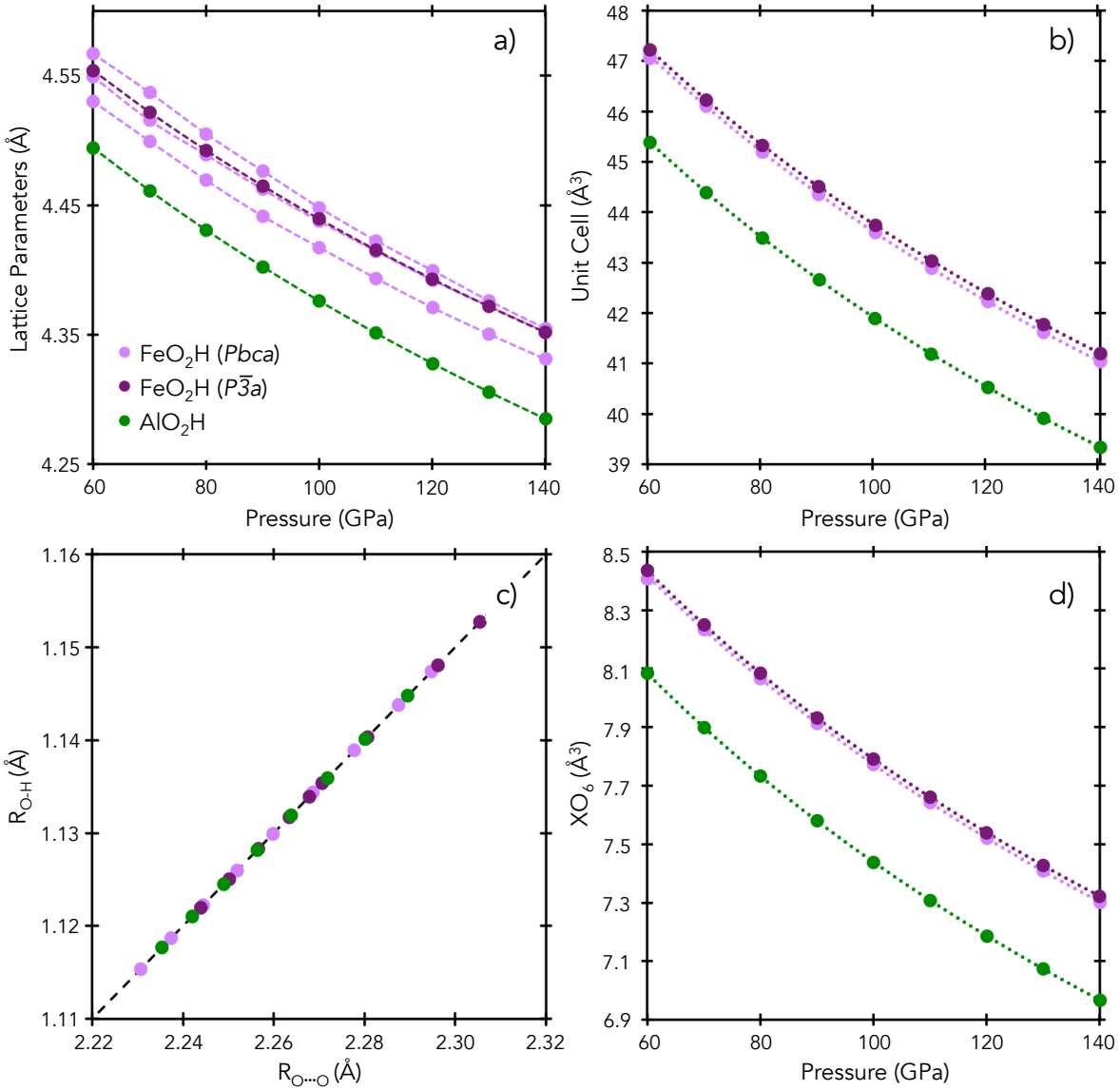

Figure 5.3: Structural parameters of pyrite-type FeO_2H and AlO_2H from 60 to 140 GPa including (a) lattice parameters, (b) unit cell volume, (c) the relationship between oxygen to oxygen distances (O—O) and oxygen to hydrogen bond length (O—H), and (d) the FeO_6 or AlO_6 polyhedral volume, referred to generally as XO_6. In all plots lavender symbols indicate the orthorhombic structure of FeO_2H, dark purple symbols indicate the cubic structure of FeO_2H, and green symbols indicate AlO_2H. The dashed black line included in plot (c) indicates the line on which symmetric hydrogen bonds will fall.

As previously mentioned, neither pyrite-type FeO_2H or AlO_2H contain discreet hydroxyl units. Unlike their respective lower pressure polymorphs, they do no undergo pressure-induced hydrogen bond symmetrization, but rather the hydrogen bonds are symmetric from the onset, as shown in Figure 5.3c. In the lower pressure polymorph of pyrite-type FeO_2H, ε-

FeOOH, hydrogen bond symmetrization led to an abrupt change in strain accommodation, which manifested as a discontinuity in the V-P relationship of the FeO_6 in that phase (Thompson et al., 2017). As the hydrogen bonds in pyrite-type FeO_2H and AlO_2H are symmetric even at the lowest pressures of these phase's respective stabilities, the volumes of their respective cation octahedra (FeO_6 or AlO_6, collectively referred to here as XO_6) decrease smoothly with pressure (Figure 5.3d).

Equation of state parameters for pyrite-type FeO_2H were determined by fitting the volume of optimized structures of GGA+U calculations between 70 and 140 GPa to third-order Birch-Murnaghan equations of state (Birch, 1947):

$$P(V) = \frac{3K_0}{2}\left[\left(\frac{V_0}{V}\right)^{\frac{7}{3}} - \left(\frac{V_0}{V}\right)^{\frac{5}{3}}\right]\left\{1 + \frac{3}{4}\left(K_0' - 4\right)\left[\frac{V_0}{V}^{\frac{2}{3}} - 1\right]\right\} \tag{5.1}$$

in which K_0 is the bulk modulus at ambient pressure, K_0' is the first pressure derivative of the bulk modulus, and V_0 is the volume per formula unit at ambient pressure. The reference volume (V_0) structure was treated as a free parameter, and results are presented for which the bulk modulus pressure derivative (K_0') was treated as either a fixed or free parameter. Results from these fits are listed in Table 5.1, where they are compared to the equation of state parameters for pyrite structure AlO_2H, with which FeO_2H forms a solid solution. Pyrite-type AlO_2H equation of state parameters were obtained using the same pressure range and methodology and our findings are in good agreement with previously reported parameters for this phase (Tsuchiya and Tsuchiya, 2011). While the iron endmember, FeO_2H, is slightly more compressible at ambient pressure than the aluminum endmember, AlO_2H, the pressure derivative of the bulk modulus in FeO_2H is higher, rendering it ultimately less compressible at the extreme pressures of the lowermost mantle.

In addition to evaluating the volume-pressure (V-P) relationship of these phases holistically, the pressure dependence of the FeO_6 and AlO_6 octahedra were also determined. This enables the evaluation of pressure regimes in which strain is accommodated unequally by the deformation of one of these components—a phenomenon associated with pressure-induced

Table 5.1: Birch-Murnaghan equation of state parameters for the high-pressure pyrite structures of FeO_2H and AlO_2H based on self-consistent U-value calculations. Values in parentheses are uncertainties on the last digit

	V_0	K_0	K'_0
Pbca FeO_2H	56.23(4)	236(1)	4 (fixed)
Pbca FeO_2H	56.97(7)	209(2)	4.33(3)
$Pa\bar{3}$ FeO_2H	56.28(4)	213(1)	4 (fixed)
$Pa\bar{3}$ FeO_2H	56.94(4)	240(1)	4.33(2)
$Pa\bar{3}$ AlO_2H	54.944(2)	214.20(4)	4 (fixed)
$Pa\bar{3}$ AlO_2H	54.914(6)	215.3(2)	3.988(3)

hydrogen bond symmetrization, in which hydrogen bonds absorb greater proportions of strain prior to symmetrization. In the case of pyrite type FeO_2H and AlO_2H, the hydrogen bonds were determined to be symmetric throughout their predicted stability ranges as previously described. Consistent with this, the V-P relationships of the FeO_2H polyhedra are smooth, lacking the change in curvature associated with a post-hydrogen bond symmetrization increase in strain accommodation (Table D.3). Additionally, as both iron and aluminum endmembers contain only symmetric bonds across their stability ranges, solid solutions from these systems are more likely to behave in a manner consistent with a linear mixing model than in systems where pressure-induced hydrogen bond symmetrization is a concern (Panero and Caracas, 2009).

5.3.4 Elastic constants and moduli

The elastic tensors of high-pressure pyrite-type FeO_2H and AlO_2H were determined to CMB pressure, as shown in Figure 5.4. As an orthorhombic distortion may exist in pyrite-type FeO_2H depending on its electronic configuration, the elastic tensor of both cubic and orthorhombic FeO_2H were evaluated. Fully describing the elasticity of an orthorhombic phase requires nine elastic constants, but these can be averaged to produce a cubic-equivalent three-constant tensor, enabling a degree of comparison between the *Pbca* and $Pa\bar{3}$ structures of FeO_2H. As shown in Figure 5.4, the elastic constants of $Pa\bar{3}$ and *Pbca* FeO_2H are in good

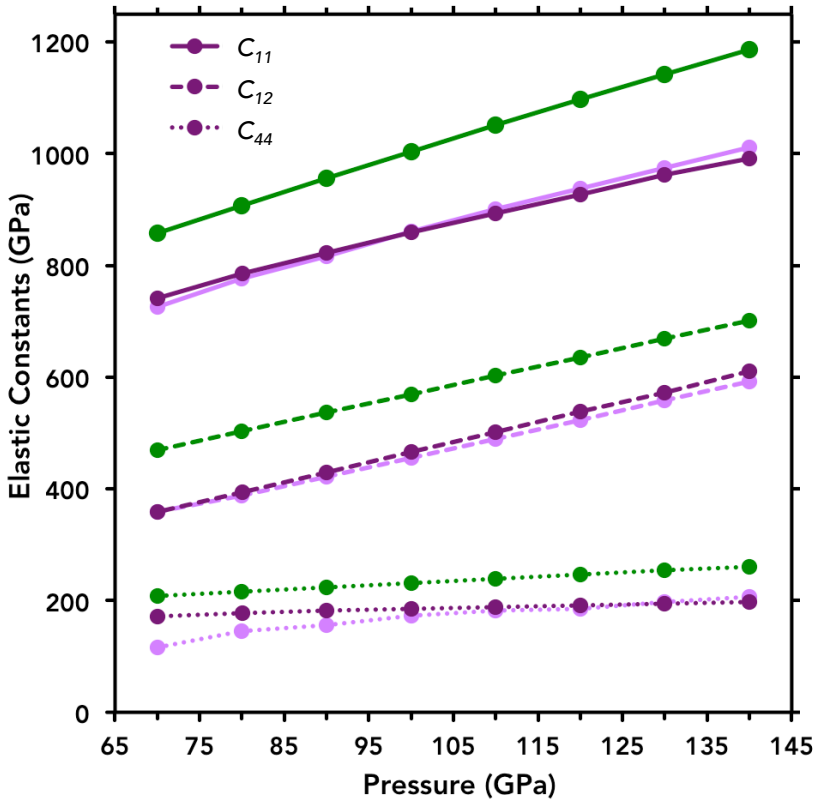

Figure 5.4: Elastic constants of pyrite-type FeO_2H and AlO_2H as a function of pressure from 70 to 140 GPa. Solid lines indicate the C_{11} constant, dashed lines indicate the C_{12} constant, and dotted lines indicate the C_{44} constant. Green lines are AlO_2H, dark purple lines are cubic ($Pa\bar{3}$) FeO_2H, and light purple lines are the cubic average of the nine constants describing the elasticity of orthorhombic ($Pbca$) FeO_2H.

agreement, becoming virtually indistinguishable at pressures >100 GPa. However, the elastic constants of pyrite-type AlO_2H differ significantly from those of FeO_2H, both in magnitude, and to a lesser degree pressure dependence. The elastic constants of the Al-endmember are 15-33% greater than those of the Fe-endmember, with the C_{12} of the two compositions converging with increased pressure while the C_{11} and C_{44} of AlO_2H and FeO_2H diverge with increased pressure. The elastic constants of both structures of FeO_2H, as well as those of AlO_2H, can be found in tabulated form in Tables D.4 and D.5. The mechanical stability of both structures of pyrite-type FeO_2H and AlO_2H were verified with the Born stability criteria (Born and Huang, 1954) relevant to orthorhombic symmetry and cubic symmetry respectively (Equations B.1, B.2, and B.3).

Table 5.2: Comparison of the elastic properties of pyrite-type FeO_2H and AlO_2H as a function of pressure from 70 to 140 GPa.

P (GPa)	*Pbca* FeO_2H			*Pa*$\bar{3}$ FeO_2H			*Pa*$\bar{3}$ AlO_2H		
	ρ (g/cm^3)	K (GPa)	μ (GPa)	ρ (g/cm^3)	K (GPa)	μ (GPa)	ρ (g/cm^3)	K (GPa)	mu (GPa)
60	—	—	—	6.248	449.0	174.0	4.389	435.0	228.9
70	6.401	481.0	134.1	6.383	485.9	179.5	4.488	469.5	237.9
80	6.530	517.1	161.5	6.510	524.8	184.7	4.581	503.8	247.5
90	6.652	552.8	170.1	6.630	560.8	187.4	4.670	536.8	256.8
100	6.769	590.5	183.3	6.746	597.3	189.5	4.755	569.7	265.8
110	6.880	626.1	188.4	6.856	632.8	191.2	4.837	602.9	274.3
120	6.988	661.5	194.5	6.962	667.4	192.6	4.916	635.4	282.7
130	7.091	696.5	200.8	7.064	702.9	194.5	4.992	668.3	290.4
140	7.190	731.3	207.0	7.162	737.5	194.4	5.065	700.6	298.2

The bulk and shear moduli of pyrite-type FeO_2H and AlO_2H were calculated from single crystal elastic constants using the Voigt-Reuss-Hill averaging scheme (Hill, 1952) as shown in Table 5.2 and Figure D.2. Bulk moduli of all three phases (*Pbca* FeO_2H, $Pa\bar{3}$ FeO_2H, and $Pa\bar{3}$ AlO_2H) are remarkably similar across the pressure range investigated, with <5% variation. Conversely the shear moduli are quite variable depending on both composition and symmetry. *Pbca* FeO_2H exhibits a reduced shear modulus compared to the cubic structure at pressures <100 GPa, due to differences between the C_{44} of cubic FeO_2H and the C_{44}, C_{55}, and C_{66} of orthorhombic FeO_2H. These differences are drastically reduced at high pressure, and at pressures of 100-140 GPa both structures of FeO_2H exhibit shear moduli within ~6% of one another. No such convergence occurs in the shear moduli of $Pa\bar{3}$ FeO_2H and $Pa\bar{3}$ AlO_2H. At 60 GPa the shear modulus of AlO_2H is ~33% greater than that of FeO_2H, and with increased pressure this divide widens, so that by core-mantle boundary (CMB) pressures the difference is ~52%.

5.3.5 Sound velocities

Elastic moduli of pyrite-type FeO_2H and AlO_2H were used to calculate the aggregate sound velocities of both compositions as a function of pressure as shown in Figure 5.5 and Table 5.3. As with the elastic moduli, the sound velocities of the two structures of FeO_2H differ most at low pressure, with the orthorhombic FeO_2H exhibiting compressional (V_P) and shear velocities (V_S) reduced relative to those of cubic FeO_2H by up to ~5 and ~14% respectively. However, differences in the sound velocities of the FeO_2H structures are significantly reduced at pressures >100 GPa, at which point the difference is <3% for both V_P and V_S. However, the compressional velocity of AlO_2H is consistently elevated relative to that of FeO_2H by a margin of 24-25% across the 70-140 GPa pressure range investigated. Furthermore, the shear velocity of AlO_2H is higher than that of FeO_2H and exhibits a positive pressure dependence, producing a V_S ~37-46% greater than that of the Fe-endmember. As the calculated δ-AlOOH → pyrite-type AlO_2H transition occurs at pressures exceeding

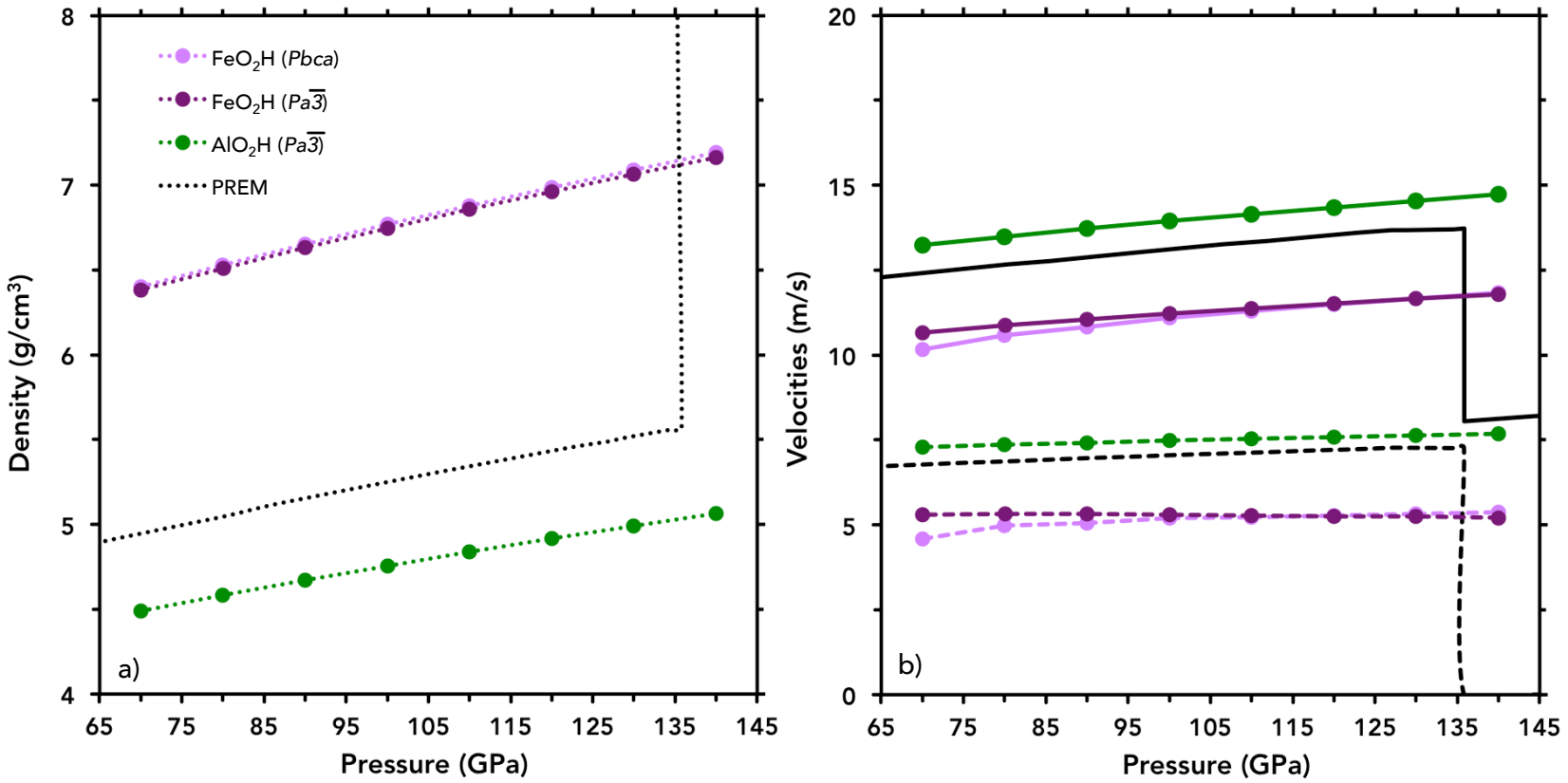

Figure 5.5: Density (a) and sound velocities (b) of orthorhombic (*Pbca*) FeO_2H (light purple symbols), cubic ($Pa\bar{3}$) FeO_2H (dark purple symbols), and cubic ($Pa\bar{3}$) AlO_2H (green symbols) as a function of pressure from 70 to 150 GPa compared to the density of the Preliminary Reference Earth Model (PREM) (black symbols). Compressional velocity is indicated by solid lines and shear velocity is indicated by dashed lines. All values plotted are 0 K values excluding those of PREM.

Table 5.3: Compressional (V_P) and shear (V_S) velocities for pyrite-type FeO_2H and AlO_2H from 70 to 140 GPa based on Hill averages (Hill, 1952).

P (GPa)	*Pbca* FeO_2H		$Pa\bar{3}$ FeO_2H		$Pa\bar{3}$ AlO_2H	
	V_P	V_S	V_P	V_S	V_P	V_S
60	—	—	10.44	5.28	12.99	7.22
70	10.15	4.58	10.66	5.30	13.24	7.28
80	10.59	4.97	10.88	5.33	13.49	7.35
90	10.83	5.06	11.06	5.32	13.72	7.42
100	11.11	5.20	11.22	5.30	13.94	7.48
110	11.29	5.23	11.38	5.28	14.15	7.53
120	11.48	5.28	11.52	5.26	14.35	7.58
130	11.66	5.32	11.67	5.25	14.54	7.63
140	11.84	5.37	11.80	5.21	14.73	7.67

those of the Earth's mantle (>170 GPa), the elastic behaviors of the Al-endmember at these pressures are relevant only in that they allow us to determine the moduli and sound velocities of intermediate (Al,Fe)O_2H compositions expected to be stable at the pressure of the lowermost mantle.

In addition to aggregate sound velocities, the single crystal azimuthal anisotropy for compression (V_P) and shear (V_S) waves and the polarization anisotropy for (V_S) of $Pa\bar{3}$ pyrite-type FeO_2H and AlO_2H were determined using the previously described formalism of Mainprice (1990) (Equations 3.2 and 3.3) as shown in Figure 5.6. Furthermore, the maximum shear wave polarization of pyrite-type FeO_2H and AlO_2H are compared here to that of their low-pressure polymorphs, ε-FeOOH and δ-AlOOH (Figure 5.7). These lower pressure polymorphs exhibit a strong degree of horizontally polarized shear wave anisotropy (S_H-S_V), a property that increases with increasing pressure (Tsuchiya and Mookherjee, 2015; Thompson et al., 2017). However, the maximum shear wave polarization anisotropy of both pyrite-type FeO_2H and AlO_2H is significantly lower than their lower pressure counterparts, and in the case of FeO_2H, exhibits a strong negative pressure dependence.

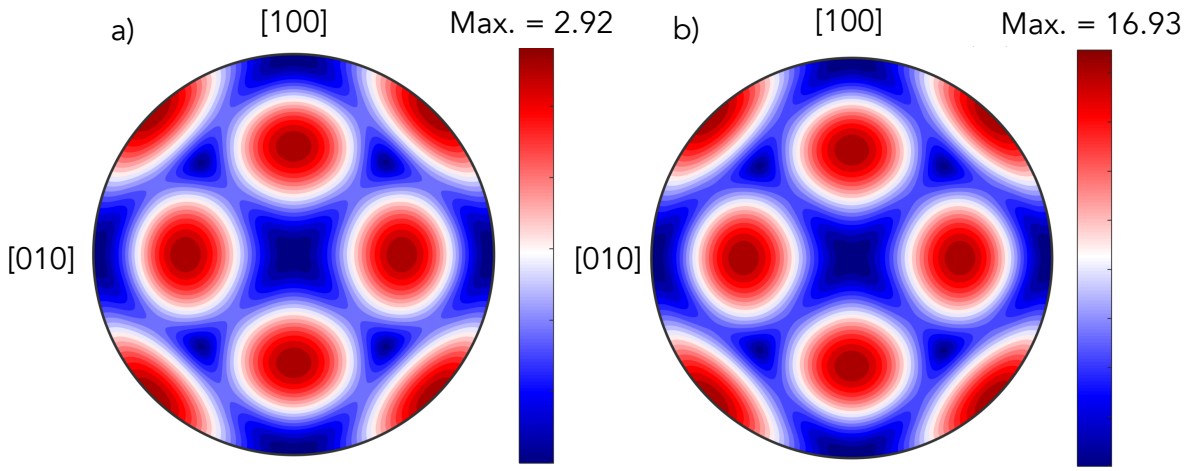

Figure 5.6: Lambert equal-area upper-hemisphere projections of the shear wave polarization (AV_S) of cubic ($Pa\bar{3}$) pyrite-type AlO_2H (left) and FeO_2H (right) at 100 GPa. Pole figures were generated using software by Mainprice et al. (2011).

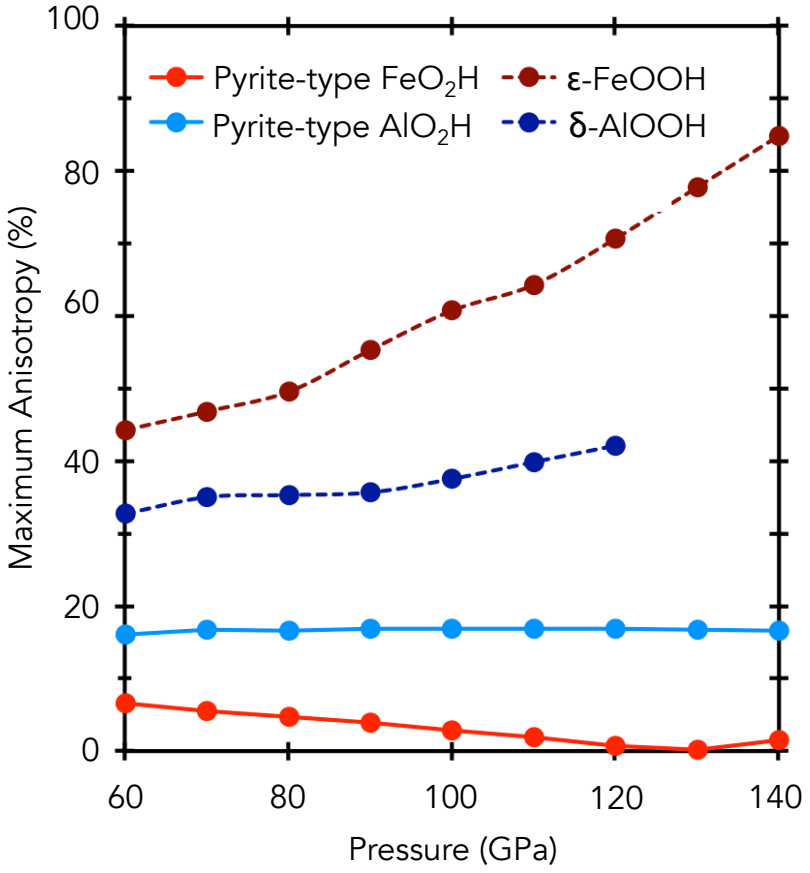

Figure 5.7: Comparison of the maximum Karat anisotropy (AV_S) of pyrite-type FeO_2H (solid red line) and AlO_2H] (solid light blue line) from 60 to GPa compared to lower pressure polymorphs ε-FeOOH (dashed dark blue line) and δ-AlOOH (dashed dark red line).

5.4 Discussion

Optimized structures indicate that the electronic structure of iron may produce a Jahn-Teller distortion in pyrite-type FeO_2H, such that the orthorhombic pyrite structure (*Pbca*) may be stable at the pressures of the lowermost mantle. This distortion evolves with increasing pressure, producing non-fixed b/a and b/c ratios. Recognition of this distortion is significant, as it may influence the interpretation of experimental data collected on this phase. Powder diffraction of orthorhombic FeO_2H may easily be interpreted as cubic, as the distortion is minimal enough to contribute to peak widths rather than the addition of discrete, resolvable diffraction peaks. Owing to the averaged nature of volume determination using powder diffraction, the effect of an orthorhombic distortion would have a minimal impact on the final resultant cell volumes ($\sim$0.1%). Conversely, misconstruing *Pbca* FeO_2H as a cubic structure is potentially more problematic when utilizing 'multigrain method' X-ray diffraction. This method combines powder and single crystal methodologies to analyze microcrystalline samples at high pressures. As this technique evaluates large numbers of overlapping single crystal patterns, an orthorhombic structure could be misinterpreted as three concurrent cubic unit cells of varying volume (one unit cell being matched to each lattice parameter). In this situation, the volume variation would not be mitigated by averaging as with powder diffraction, and any volume variation would likely be misattributed to a pressure or chemical gradient in the sample.

Based on our calculations, the transition pressure of $CaCl_2$-type (Al,Fe)OOH to the pyrite structure is strongly compositionally dependent, and both $CaCl_2$-type and pyrite-type (Al,Fe)OOH may persist to pressures up to the core-mantle boundary. The lower pressure $CaCl_2$ polymorph is stabilized by the incorporation of aluminum, while compositions predominated by iron are likely to transform to the pyrite structure at the pressures of the lowermost mantle. The seismic signature of AlOOH is not expected to change dramatically across this phase transition, as the compressional and shear wave velocities of δ-AlOOH and

pyrite-type AlO_2H differ by <2%. However, while the compressional velocities of pyrite-type FeO_2H and ε-FeOOH are roughly similar in magnitude and pressure dependence, with the V_P of ε-FeOOH reduced 2-4% relative that of the pyrite structure across the 60-140 GPa pressure range, the difference in shear velocity is more substantial. The V_S of ε-FeOOH is reduced 11-16% compared to the V_S of pyrite-type FeO_2H.

The sound velocities of pyrite-type FeO_2H from this study can also be compared to, with some limitations, the DFT results published recently by Liu et al. (2017) as shown in Figure D.3. Unfortunately this study did not report 0K velocities, 0K moduli, or sufficient computational details to enable the temperature correction of their data back to static conditions. With those caveats in mind, the FeO_2H sound velocities of Liu et al. (2017) are quite similar to those reported here, the V_P and V_S differing by <3% and <7% respectively. Conversely, both compressional and shear wave sound velocity trends reported by Liu et al. (2017) exhibit higher positive pressure dependences than those of this study. Liu et al. (2017) concluded, based on the previously described DFT calculations of the density and sound velocities of pyrite-type FeO_2H as wells as limited experimental results, that Ultra Low Velocity Zones (ULVZs) might be reasonably explained by domains at the CMB rich in pyrite-type FeO_2H_X–a partially dehydrated form of stoichiometric FeO_2H.

We have re-evaluated the potential for pyrite-type FeO_2H, and more importantly the solid solution it likely forms [(Al,Fe)O_2H], to contribute to the ∼10% V_P reduction and 10-30% V_S reduction relative to surrounding mantle material which is characteristic of ULVZs (e.g., Ganero and Helmberger 1996; Thorne and Ganero 2004; McNamara et al. 2010; Li et al. 2017; Yu and Ganero 2018). Based on these calculations we determined that pyrite-structured $(Al_X,Fe_{1-X})O_2H$ with X =0.4-0.5 can simultaneously match both requisite sound velocity reductions for this region. Additionally, as the phase is predominately iron bearing, we expect the phase transition to the pyrite-structure to occur above the base of the mantle where these features are observed. Importantly, this shows that pyrite-type FeO_2H, or more exactly, iron rich pyrite-type solid solution enriched regions may contribute to observed

ULVZs without any dehydrogation needed to match seismic observations. However, the persistence of ULVZs and other deep Earth structures dominated by hydrous phases at geological timescales might be mitigated by the rate of hydrogen diffusion in the Earth's mantle, which has yet to be conclusively resolved (e.g., Mackwell and Kohlstedt (1990); Novella et al. (2017)).

Previously, the anomalous negative pressure dependence of the V_S of ε-FeOOH was used to conclude that Fe-bearing solid solutions from the FeOOH–AlOOH–$MgSiO_4H_2$ system may contribute to the reduced shear wave velocities characteristic of large low shear velocity provinces (Section 3.4; Thompson et al. 2017). Because endmember ε-FeOOH is unexpected in the deep Earth, and the $CaCl_2 \rightarrow FeS_2$ structural transition is highly dependent on composition, solid solutions containing the $< 1\%$ by volume FeOOH previously invoked to reproduce the shear wave velocity reductions of LLSVPs are expected to be stable at the P-T conditions of the lower mantle. Physically proximal and compositionally similar LLSVPs containing Al-dominant solid solutions of $CaCl_2$-type (Al,Fe)OOH and ULVZs containing Fe-dominant solid solutions of pyrite-type (Al,Fe)O_2H might also share a geochemical origin. As gravitationally unstable $CaCl_2$-structured (Al,Fe)OOH solid solutions reach the core-mantle boundary, elevated temperatures and reaction with core material may produce elevated levels of iron enrichment, driving the transition to the pyrite structure. Additionally, pyrite-type FeO_2H may be produced by the reaction of water with iron at the core-mantle boundary (Yuan et al., 2018b).

There is sharp contrast in the maximum shear wave polarization anisotropy of high-pressure pyrite-type FeO_2H and AlO_2H compared to their respective lower pressure $CaCl_2$-type polymorphs—a contrast which is greatest at the pressures of the lowermost mantle. As such, the $CaCl_2 \rightarrow FeS_2$ structural transition in the (Al,Fe)OOH solid solution may be marked by an observable seismic signature. The sharpness of such a signal would depend strongly on two primary factors: (1) variability in composition, as the iron and aluminum endmembers have phase boundaries >100 GPa apart, and (2) the degree of lattice preferred

orientation (LPO) locally in each phase. Pyrite-type $(Al_X,Fe_{1-X})O_2H$ with X<0.5 is likely stable at CMB pressures, where it would exhibit low to negligible degrees of shear wave polarization. Conversely, $CaCl_2$-type $(Al_X,Fe_{1-X})OOH$ in which X>0.5 may also be stable at CMB pressures, and would be characterized by strongly horizontally polarized shear waves consistent with observations of horizontally polarized shear waves at the base of the mantle (Section 3.4; Thompson et al. 2017). Although there is no data regarding the shear wave polarization anisotropy of δ-AlOOH above 120 GPa, the difference in the maximum shear wave polarization anisotropy of $CaCl_2$-type $(Al_X,Fe_{1-X})OOH$ [X>0.5] is already an order of magnitude higher than that of pyrite-type $Al_XFe_{1-X}O_2H$ [X<0.5] at 120 GPa. As the shear wave anisotropy $CaCl_2$-type FeOOH has a strong positive pressure dependence, and the pyrite-type structure has a strong negative dependence, we expect the difference in the solid solutions to be as great, if not greater at the CMB.

5.5 Conclusions

We have presented a detailed computational analysis of the stability, structure, and elastic properties of high-pressure pyrite-type FeO_2H. The structure, transition pressure, and equation of state of this phase was compared to that of pyrite-type AlO_2H, with which it forms a solid solution. Based on our *first principles* calculations the likely stable structure is cubic, although at sufficiently high pressure a Jahn-Teller distortion in FeO_2H may produce an orthorhombic structure. Such an orthorhombic distortion could lead to an inaccurate assessment of the unit cell volume of this phase, particularly in conjunction with the 'multigrain method 'of experimental crystal structure determination.

Solid solutions from the $CaCl_2$-structured $(Fe,Al)O_2H$ system transform to the pyrite (FeS_2) structure between 70-195 GPa, with an appropriate transition pressure being compositionally dependent and obtainable using a linear mixing model of the Al- and Fe-endmembers. Owing to this compositionally driven phase boundary, which can occur over a range of >100 GPa, it is likely that Al-dominant $CaCl_2$-type $(Fe,Al)O_2H$ coexists with Fe-dominant pyrite-

type (Al,Fe)O_2H in the Earth's lower mantle. Yet, pyrite-type (Al,Fe)O_2H exhibits significantly different seismic properties compared to those of $CaCl_2$-structured (Al,Fe)OOH, both in terms of seismic velocities and shear wave anisotropy. Both $CaCl_2$ and pyrite-structured (Fe,Al)O_2H solid solutions may deliver hydrogen through the Earth's lower mantle to the core-mantle boundary, but the seismic properties of these solid solutions are strongly tied to their structure, which itself is compositionally dependent. Al-rich compositions are likely to maintain the $CaCl_2$ structure and could contribute to LLSVPs, while iron-rich compositions will transform at lower mantle pressures to the pyrite-structure and could contribute to the reduced velocities observed in ULVZs. Hence, it is paramount that when matching seismic observations, one takes into account the composition, structure, and stability of the solid solution rather than an isolated endmember composition.

CHAPTER 6

GEOPHYSICAL PROPERTIES OF *fcc* IRON HYDRIDE

6.1 Introduction

Earth's core is composed of an iron-rich alloy with the inclusion of light elements necessary to compensate for the 5-10% difference between seismically determined core densities and the density of pure iron at relevant pressure and temperature (P-T) conditions (Birch, 1952). As the most abundant and lightest element in the solar system, hydrogen is a plausible contributor to this core density deficit (Williams and Hemley, 2001). Iron hydride formation at Earth's surface is unlikely because the equilibrium hydrogen solubility in iron at atmospheric conditions is prohibitively low. However, as hydrogen solubility increases with pressure, so does the likelihood of FeH_X formation within the Earth's interior (Fukai and Akimoto, 1983). Nearly stoichiometric iron hydride (FeH_X, X$\sim$1) has been shown to result from either the reaction of Fe and hydrous silicates (Yagi and Hishinuma, 1995) or the reaction of Fe and water at lower mantle conditions (Ohtani et al., 2005).

Within the known iron hydride phase diagram, the face-centered cubic (*fcc*) structure is considered the most stable structure at high temperatures, rendering it more important for extrapolation to core P-T conditions than the *bcc* or *hcp* structures (Pépin et al., 2014). Despite its importance, experimental and *ab initio* efforts have yet to agree on the equation of state parameters needed to describe the compressional behavior of FeH_X (Fukai et al., 2003; Pépin et al., 2014; Hirao, 2004; Badding et al., 1991). To constrain the extent to which hydrogen contributes to the density deficit of the Earth's core, it is necessary to first establish the compressional wave velocity-density (V_P-ρ) relationship of iron hydrides. New experimentally determined sound velocities of *fcc* FeH_X are reported here. These values are combined with literature values to determine, via Birch's law, the influence of the non-stoichiometric hydrogen on the V_P-ρ relationship of iron.

6.2 Methods

6.2.1 Sample synthesis

Two sample geometries were used in this study—one geometry for X-ray diffraction (XRD) experiments only, and a second geometry for samples on which both Nuclear resonant inelastic X-ray scattering (NRIXS) and XRD experiments were performed. XRD-only samples were composed of a 3-5 μm thick, 30-50 μm diameter natural iron foil (99.9% purity, Alfa Aesar) pressed between an upper layer of C_nH_{2n+2} paraffin (100% purity, Candlewic), which served as the hydrogen source, and a lower layer of MgO, which served as pressure medium and secondary pressure standard. Paraffin was chosen as a hydrogen source based on the recently published synthesis of *fcc* FeH using this sample configuration (Narygina et al., 2011). Additionally, we found no increased occurrence of diamond failure in these samples, presumably indicative of relatively low rates of hydrogen embrittlement. Sample pressures in this geometry were monitored using the Raman shift of the diamond peak (Akahama and Kawamura, 2007) and the equation of state for MgO (Matsui et al., 2000). These XRD-only samples were loaded into Re-gaskets pre-indented to ∼27 GPa. In the second geometry, samples were composed of individual μm thick, 30-50 μm diameter iron foils of 20-95% ^{57}Fe enrichment (>98% purity, Cambridge Isotope Laboratories) pressed between two layers of C_nH_{2n+2} paraffin (100% purity, Candlewic) that served as both hydrogen source and pressure medium. A small (<10 μm) ruby ball was included in the sample chamber adjacent to the iron foil, to enable pressure determination via the established pressure dependence of the ruby R_1 luminescence line (Mao et al., 1986). These samples, prepared for both XRD and NRIXS experiments, were loaded into pre-indented Be-gaskets with boron-epoxy inserts. Samples of both configurations were loaded into ∼70 μm sample chambers in pre-indented gaskets, using panoramic or symmetric diamond anvil cells with 150-300 μm culet anvils.

6.2.2 Synchrotron X-ray diffraction

Double-sided laser-heating synthesis was performed at beamline 13-ID-D (GSECARS) at the Advanced Photon Source (APS) of Argonne National Laboratory, where the formation of *fcc* FeH_X was monitored using *in situ* angle-dispersive XRD. Samples were simultaneously laser-heated on both sides using a flat-top profile laser, and laser power was adjusted upstream and downstream throughout heating to minimize axial temperature gradients, such that upstream/downstream differences were ∼4% of the sample temperature. Temperatures were determined via spectroradiometry using the greybody approximation (Prakapenka et al., 2008). Diffraction measurements utilized a monochromatic incident X-ray beam (λ= 0.3344 or 0.2952 Å) with a 3 μm by 4 μm focus size at full-width at half-maximum. Additional details of sample synthesis including P–T–V information can be found in Supplemental Table 1. Sample to detector distances and tilt were calibrated using 1-bar diffraction of LaB_6. DIOPTAS was used to produce 2θ plots (Prescher and Prakapenka, 2015), and PeakFit (Systat Software) was used to fit individual Gaussian peaks in the resultant integrated patterns to determine lattice parameters as a function of pressure.

Pre-heating XRD confirmed that initial sample foil composition at high pressure was *hcp* iron, and *in situ* high-temperature diffraction established the formation of *fcc* FeH_X at temperatures of, or exceeding, 1500 K (Table 6.1). Although the peak synthesis temperatures of this study at times exceeded the melting curve reported by Sakamaki et al. (2009), this discrepancy may be attributed to the different eutectic melting systems in these studies, which were on opposite sides of the FeH composition. High P-T conditions were held until all *hcp* iron peaks diminished, at which point the sample was thermally quenched by shutting off laser power. Post-heating room-temperature patterns were evaluated to confirm quenching of *fcc* FeH_X (Figure 6.1). Pre- and post-heating sample pressures determined using the Raman shift of the diamond peak revealed a post-heating pressure decrease (∼0.5 GPa), consistent with the transition to a higher density phase. The reaction sequence previously

described by Narygina et al. (2011) (Fe + C_nH_{2n+2} → $2Fe_3C$ + $3H_2$ → 6FeH + 2C) was not consistently observed, as no attempt was made to evaluate this transformation with low temperature (<1500 K) diffraction. Additionally, the obtained phase assemblage (Table S1) did not consistently indicate the presence of diamond, likely due to diamond's poor diffraction properties, particularly when synthesized at low temperatures (Zeng et al., 2017). Though the formation of *fcc* FeH_X could be confirmed using at minimum the (111) and (200) peaks, the presence of iron carbide was not detected via XRD.

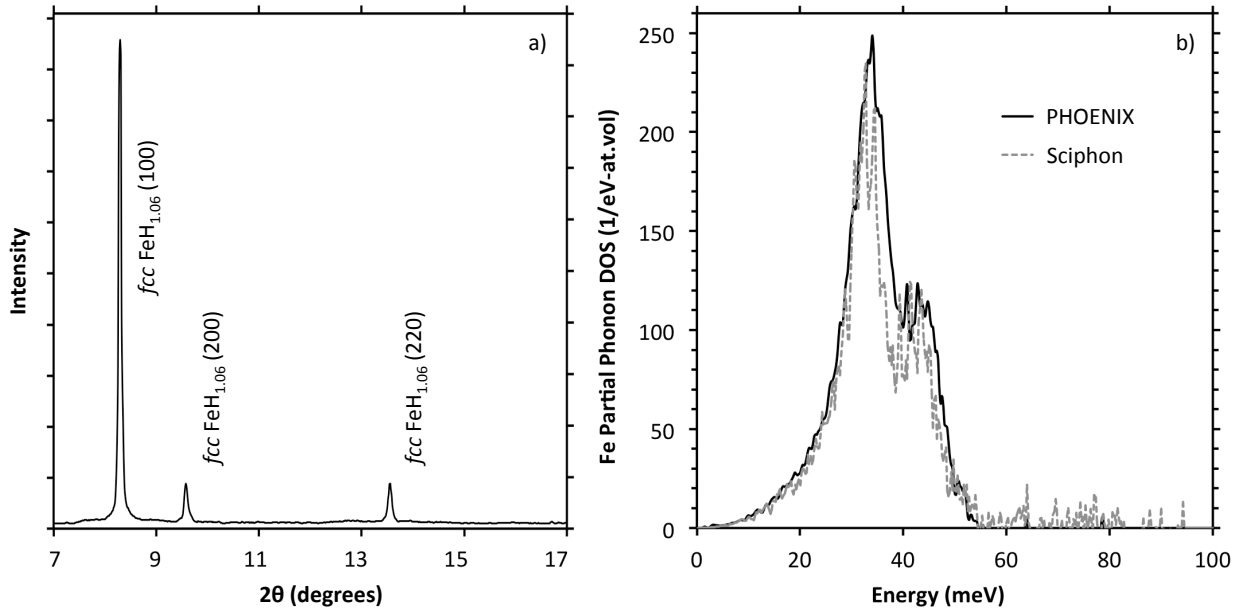

Figure 6.1: Measurements of quenched non-stoichiometric (X ∼1.06) *fcc* FeH_X at 64 GPa, including (a) Integrated X-ray diffraction with FeH_X peaks labeled with their respective Miller indices, and (b) Fe partial phonon density of states (DOS). The DOS indicated by the solid black line was obtained using the PHOENIX program (Sturhahn, 2000), and dotted grey line is the DOS obtained from Sciphon 1.0.3 (Dauphas et al., 2014).

6.2.3 Nuclear resonant inelastic X-ray scattering (NRIXS)

Sample synthesis for NRIXS experiments relied on the sample geometry described previously in 2.1 in panoramic-type diamond anvil cells. After starting materials were loaded, FeH_X was synthesized at the University of Chicago via single-sided laser heating with a 1064 nm Yb-doped fiber laser. Temperatures were determined by multispectral imaging radiom-

etry (Campbell, 2008) and reported uncertainties reflect the temperature gradient typical of one-sided laser heating of a thin foil sample. To homogenize the synthesized sample, the laser, producing a ∼15μm diameter heated spot, was slowly rastered across the sample chamber, avoiding the outermost edges nearest the gasket. Post-synthesis synchrotron XRD to confirm the conversion of iron to *fcc* FeH_X and evaluate sample stoichiometry was performed at 13-ID-D (as previously described) or at 13-BM-C using a monochromatic incident X-ray beam (λ= 0.3344 Å). Initially, diffraction patterns were obtained at each post-synthesis pressure step to monitor stoichiometric changes in the quenched sample. In the final sample this was deemed unnecessary as the stoichiometry of each sample was found to depend solely on the P-T conditions of formation and not post-quench pressure changes.

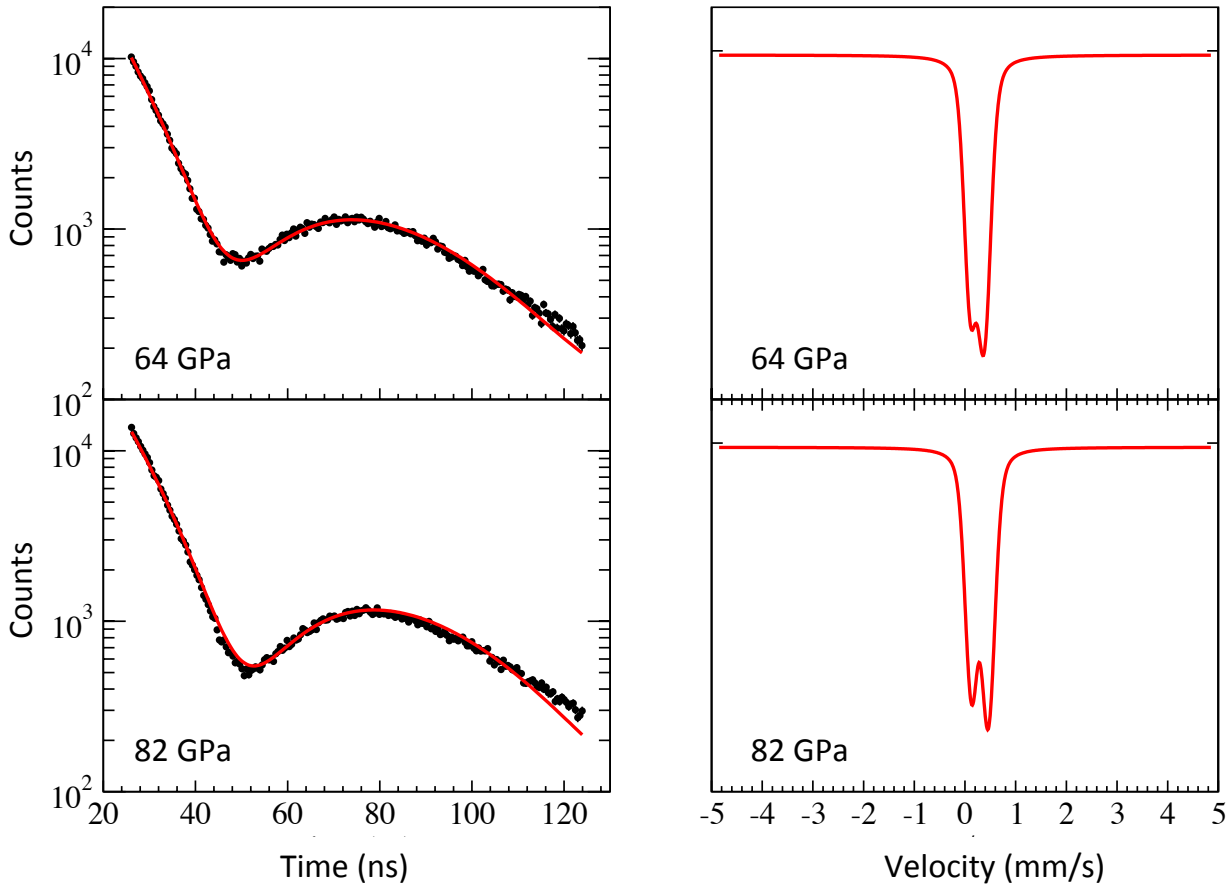

Figure 6.2: (a) Synchrotron Mössbauer spectra of non-stoichiometric (X∼0.94) *fcc* FeH_X at 64 and 82 GPa, black dots are experimental SMS data and red lines are modeled spectra. (b) Energy spectra calculated from the modeled Mössbauer fits.

Ambient temperature NRIXS experiments on thermally quenched *fcc* FeH_X were performed at Sector 3 of APS, Argonne National Laboratory. NRIXS spectra were obtained using an incident X-ray energy tuned within ±100 meV around the nuclear transition energy of ^{57}Fe (14.4125 keV), an X-ray beam of approximately 15 μm diameter (FWHM) and an energy resolution of 1 meV in the first experimental run and 2 meV in the second run. Three avalanche photodiode detectors, positioned equidistantly around the panoramic DAC, collected time-delayed $\chi_{\alpha,\beta}$-fluorescence emitted from the excitation of the enriched iron sublattice due to the incident X-ray beam. The storage ring was operated in top-up mode with 24 bunches separated by 153 ns, allowing for the detection of nuclear resonant scattering during the time window following initial excitation. Multiple ∼45 minute NRIXS scans were collected at each pressure step and stacked to maximize counts with total per sample accumulation times of 10-21 hours, increasing the signal to noise ratio. The collected *fcc* FeH_X spectral form was found to be distinct from that of pure Fe or *dhcp* FeH_X. Stacked spectra were analyzed using both PHOENIX (Sturhahn, 2000) and Sciphon 1.0.3 (Dauphas et al., 2014) to extract the partial phonon density of states (pDoS) from the iron sublattice using a quasiharmonic model (Figure 6.1).

6.2.4 Synchrotron Mössbauer spectroscopy (SMS)

Room-temperature forward scattering synchrotron Mössbauer spectra of thermally quenched *fcc* FeH_X samples were collected at beamline 3-ID-B of the Advanced Photon Source, Argonne National Laboratory using a fourth detector in line with the incident X-ray beam path. These experiments were performed contemporaneously to 64 and 82 GPa NRIXS measurements using the same samples. A thin plate of $FeSO_4{\cdot}7H_2O_4$ (IS = 1.34 mm/s, QS = 3.16 mm/s) introduced into the beam path was used as a reference to obtain the isomer (central) shift. Resultant SMS spectra were evaluated using the CONUSS program (Sturhahn, 2000) to determine the magnetic properties, isomer shift, and quadrupole splitting of *fcc* FeH_X as a function of pressure (Figure 6.2).

6.3 Results

6.3.1 Equation of state and sample stoichiometry

Determining the stoichiometry of metal hydrides is difficult owing to the small X-ray cross-section of hydrogen. However, it is possible to make informed estimates of the amount of hydrogen dissolved in the phase based on cell volumes and the well-established behavior of pure *fcc* iron. Hydrogen content of FeH_X can be estimated using the formula:

$$x = \frac{\left(V_{FeH_X} - V_{Fe}\right)}{\Delta V_H} \tag{6.1}$$

in which V_{FeH_X} and V_{Fe} are unit cell volumes of iron hydride and pure iron metal, respectively, and ΔV_H is a predetermined volume expansion due to a single formula unit of interstitial hydrogen. The value of ΔV_H is not precisely known for iron hydrides, and previous studies have utilized fixed values ranging from 1.8 to 2.6 $Å^3$ (Antonov et al., 1998; Badding et al., 1991; Fukai, 2005; Narygina et al., 2011). The basis for these approximations is the interstitial volumes associated with other *3d*-transition metal hydrides or deuterides (e.g., CoH; Fukai 2005). Variations in ΔV_H can substantially alter the assumed stoichiometry of a sample, and the assumption that this value is fixed across all pressures may result in erroneous equations of state.

This study instead leverages more realistic interstitial hydrogen volumes that vary as a function of pressure. We utilize two different interstitial hydrogen equations of state, one based on the calculations of Caracas (2015) and one based on the experimental *dhcp* FeH results of Pépin et al. (2014). No comparable work on the equation of state of *fcc* FeH is available, so we rely on the interstitial H volume in these closely related structures. In both cases, the *V-P* relationship of interstitial hydrogen in FeH_X was determined by evaluating the difference in volume between the volumes of iron hydride and pure *hcp* iron at the same pressure. The reference volume of pure iron used with the Caracas (2015) dataset was the

Table 6.1: Third-order Birch-Murnaghan equation of state parameters for interstitial hydrogen in iron hydride, including ambient-pressure volume (V_0), ambient-pressure bulk modulus (K_0) and its pressure derivative (K_0'). Values in parentheses are uncertainties in the last digit.

EoS	V_0 (Å^3)	K_0 (GPa)	K_0'
Based on Caracas (2015)	2.232(0)	181.3(1)	3.18(1)
Based on Pépin et al. (2014)	2.684(3)	63.14(5)	3.82(1)

iron curve presented in that same work, while an empirical equation of state by Dewaele et al. (2006) was used for the Pépin et al. (2014) dataset. This synthetic V-P data for hydrogen in FeH_X was fit to a third-order Birch-Murnaghan (BM) equation of state (Birch, 1978):

$$P(V,T) = 3K_0 f_E \left[\left(1 + 2f_E\right)^{\frac{5}{2}} \left(1 + \frac{3}{2}\left[K_0' - 4\right] f_E\right) \right] \tag{6.2}$$

which relates pressure (P), volume (V), ambient pressure bulk modulus (K_0), and its pressure derivative (K_0') in terms of finite Eulerian strain (f_E):

$$f_E = \frac{1}{2}\left[\left(\frac{V_0}{V}\right)^{\frac{2}{3}} - 1 \right] \tag{6.3}$$

which is a measure of the volume compression of a solid relative to its initial volume (V_0). The resultant equation of state parameters for interstitial hydrogen in iron hydrides are reported in Table 6.1. A known trade-off exists between reference volume (V_0) and bulk modulus (K_0), such that both experimentally and theoretically grounded equations of state provide reasonable, and not dissimilar, estimates of interstitial hydrogen compressibility.

The two interstitial hydrogen equations of state were combined with an experimental equation of state (EoS) for *fcc* iron (Tsujino et al., 2013) to enable the determination of sample stoichiometry in our experiments (Figure 6.3, Table S1), using equation 6.1 with ΔV_H from the equations of state for interstitial H in FeH_X (Table 6.1). While the stoichiometries of our samples cluster around X=1, there is scatter, particularly in at low pressures (<35 GPa). No systematic co-variation was observed linking temperature of synthesis, heating

duration, or sample geometry to stoichiometry. It is possible that local variation, at the scale of the laser heated spot, in the paraffin:Fe ratio of the sample led to reduced hydrogen enrichment at some P-V points. These sample stoichiometries were subsequently used to interpret the resultant phonon density of states and Mössbauer hyperfine field parameters. Here it is assumed that ΔV_H is identical in both *fcc* and *hcp* FeH, because of the similarity of interstitial sites in these structures. Based on the congruence of FeH_X volumes and inferred stoichiometries (and velocities, described below) presented herein and earlier work in carbon-free (with respect to starting materials) Fe-H systems (e.g., Mao et al. 1990), we infer that during synthesis only negligible amounts of carbon entered the iron hydride.

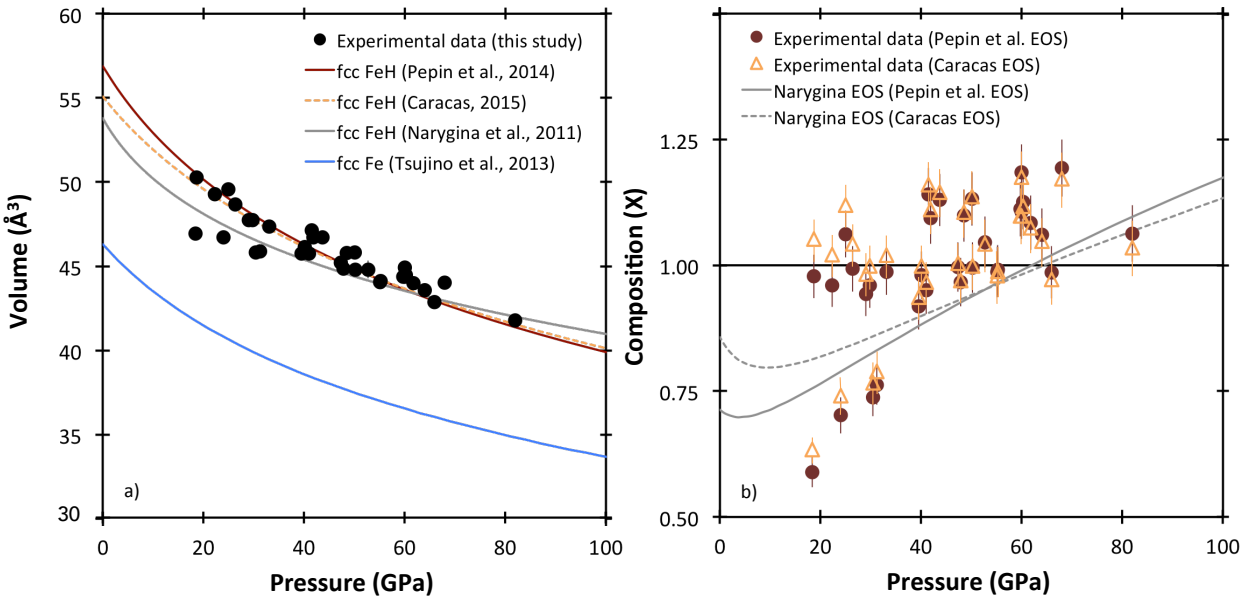

Figure 6.3: (a) Experimental P-V data from this study (black circles) compared to an *fcc* iron equation of state (blue), a previously reported *fcc* FeH equation of state (grey), and the two new synthetic *fcc* FeH_X equations of state reported in this study, based on Pépin et al. (2014) (red) and Caracas (2015) (orange). Error bars show uncertainty of experimental data points, and when not evident reflect errors not exceeding the size of the symbol itself. (b) Calculated sample stoichiometries of FeH_X as a function of pressure calculated using the hydrogen equation of state based on Pépin et al. (2014) (red solid circles) and Caracas (2015) (open orange triangles). The equation of state for stoichiometric (X=1) *fcc* FeH reported by Narygina et al. (2011) has been re-evaluated using the both synthetic equations of state reported here. Both experimental data and equations of state are plotted at room temperature (300 K).

In addition to evaluating the stoichiometry of our own samples, our synthetic FeH equations of state based on combining the EoS of pure fcc iron Tsujino et al. (2013) with the addition of hydrogen determined both theoretically and experimentally (Caracas, 2015; Pépin et al., 2014) were used to reevaluate the previously published EoS of *fcc* FeH_X by Narygina et al. (2011) (Figure 6.3a). This comparison illuminates an important discrepancy as shown in Figure 6.3b, namely that the Narygina et al. (2011) EoS requires the interstitial hydrogen to exhibit a negative bulk modulus, as the volume difference between their FeH isotherm and that of pure *fcc* iron increases with increasing pressure. The results of Narygina et al. (2011) might instead be better interpreted as a pressure dependent evolution of stoichiometry, an interpretation that could also explain the unusually large bulk modulus pressure derivative (K_0'=11.7) reported in their study.

6.3.2 Nuclear hyperfine interactions

Synchrotron Mössbauer spectra of *fcc* FeH_X at 64 and 82 GPa consist of a single broad feature (Figure 6.2). The 64 GPa hyperfine fields were best fit by model with a single iron sublattice site while the 82 GPa hyperfine fields were best fit by a model with a second site, consistent with a slightly distorted cubic system, possibly due to the room-temperature compression of the sample post-synthesis. The quadrupole splitting (QS) of a material using SMS is determined by fitting the experimental spectra to a model, and is indicative of the degree to which an electric field gradient has caused nuclear splitting in the iron sublattice, and to a lesser extent, the coordination of iron. If present, a pressure-induced spin transition (HS→LS) would lead to a dramatic increase in the value of QS (Li et al., 2006; Bengtson et al., 2009; Catalli et al., 2011; Hsu et al., 2010), but as no such change in the value of QS between the 64 and 82 GPa spectra from this experiment (Table 6.1) a spin transition appears unlikely in *fcc* FeH_X in this pressure range. Spectra at both pressures have similar (isomer) central shifts (CS) with respect to α-iron at comparable pressure, are in reasonable agreement with the CS previously reported by Narygina et al. (2011) at 47 GPa, and are

distinct from the central shift reported for either the *dhcp* or *hcp* phases (Table S2). In agreement with previous studies, the *fcc* phase of FeH_X is not ferromagnetic, in contrast to that of the *dhcp* and *hcp* phases (Narygina et al., 2011; Tsumuraya et al., 2012), and as such SMS functions as a secondary confirmation of the structure of our samples, as there is no evidence of magnetic hyperfine field splitting in the measured spectra.

6.3.3 Sound velocities and geophysical parameters

Coupled with quasi-hydrostatic XRD data and two *fcc* FeH equations of state to provide appropriate parameters, NRIXS provides velocity-density (V_P-ρ) information for comparison against seismic measurements. The Debye velocity (V_D) was determined from the calculated pDoS using both PHOENIX (Sturhahn, 2000) and Sciphon (Dauphas et al., 2014), assuming Debye-like behavior at low energies and fitting the low energy (3.8 to 16.2 meV) region to a parabola (Table 6.4). Once a Debye velocity was obtained by fitting the partial phonon density of states curve, additional equation of state information was incorporated to extract compressional (V_P) and shear velocities (V_S) using the following equation (Mao et al., 2001):

$$\frac{3}{V_D^3} = \frac{1}{V_P^3} + \frac{2}{V_S^3} \tag{6.4}$$

In this study, the necessary input parameters (K, ρ), as well as stoichiometric information, were obtained from the two previously described FeH_X equations of state. Sound velocities as determined from PHOENIX software are reported in Table 2; comparable values determined using Sciphon, as well as the mean interatomic force constants (Φ) and Lamb-Mössbauer factor (f_{LM}), are included in Table S1. These parameters help to constrain the density, velocities, and moduli of *fcc* FeH_X for comparison to seismic observations of Earth's core.

Table 6.2: Geophysically relevant parameters of including sample pressure at time of NRIXS measurement (P), composition in terms of FeH_X (X), density (ρ), bulk modulus (κ), and shear modulus (μ) as determined using PHOENIX software. Parameters are shown as calculated using both *fcc* FeH_X equations of state rooted in the Caracas (2015) hydrogen values (denoted as 'C' below) and the Pépin et al. (2014) hydrogen volumes (denoted 'P'). Values in parentheses reflect uncertainties.

P (GPa)	EoS	X	ρ (kg·m^{-3})	K (GPa)	μ (GPa)
18.4(2)	C	0.63(4)	8.14(1)	232(1)	83(1)
18.4(2)	P	0.59(3)	8.14(1)	212(1)	84(1)
29.0(3)	C	0.98(4)	7.94(1)	277(1)	136.5(8)
29.0(3)	P	0.94(4)	7.93(1)	250(1)	137.1(9)
41.0(4)	C	0.97(5)	8.28(1)	326(1)	148.2(9)
41.0(4)	P	0.95(5)	8.28(1)	300(1)	149(1)
64.0(6)	C	1.05(5)	8.83(1)	416(1)	172(1)
64.0(6)	P	1.06(5)	8.83(1)	390(1)	173(1)
82.0(8)	C	1.04(6)	9.21(1)	484(1)	183(1)
82.0(8)	P	1.06(6)	9.21(1)	460(1)	184(2)

6.4 Hydrogen in the core

The Earth's core is known to be lighter than pure iron at the corresponding pressures and temperatures (Birch, 1952). The density deficit has been estimated to be 5–10% for the outer core (Stevenson, 1981; Anderson and Isaak, 2002) and 1–2% for the inner core (Jephcoat and Olson, 1987; Stixrude et al., 1997), attributable to the presence of one or more light element-bearing component(s) in the Earth's core. In addition to other elements (O, S, C, Si, etc.), hydrogen has long been considered a potentially major light component in the core (e.g., Stevenson 1977). The amount of hydrogen needed to fulfill the density deficit can be estimated assuming an ideal mixture of pure iron and light element-bearing phases, and extrapolating the corresponding equations of state (EOSs) to core-mantle boundary (CMB) conditions (Poirier, 1994).

High-temperature Birch-Murnaghan EoSs for *fcc* iron (Tsujino et al., 2013) and *hcp* iron (Dewaele et al., 2006) were combined with our theoretically-based interstitial hydrogen equations of state (Table 1) to determine the necessary hydrogen content required to match the density of PREM at the CMB and at the inner core boundary (ICB) in *fcc* and *hcp* iron

Table 6.3: Sound velocities from NRIXS measurements (P), composition in terms of FeH_X (X), compressional wave velocity (V_P), Debye velocity (V_D), and shear wave velocity (V_S) as determined using PHOENIX software. Parameters are shown as calculated using both *fcc* FeH_X equations of state rooted in the Caracas (2015) hydrogen values (denoted as 'C' below) and the Pépin et al. (2014) hydrogen volumes (denoted 'P'). Values in parentheses reflect uncertainties.

P (GPa)	EoS	X	V_P (km·s^{-1})	V_D (km·s^{-1})	V_S (km·s^{-1})
18.4(2)	C	0.63(4)	6.49(5)	3.59(7)	3.20(7)
18.4(2)	P	0.59(3)	6.30(5)	3.59(7)	3.20(7)
29.0(3)	C	0.98(4)	7.61(2)	4.63(3)	4.15(3)
29.0(3)	P	0.94(4)	7.39(2)	4.63(3)	4.16(3)
41.0(4)	C	0.97(5)	7.96(3)	4.73(4)	4.23(4)
41.0(4)	P	0.95(5)	7.76(3)	4.73(4)	4.24(4)
64.0(6)	C	1.05(5)	8.55(3)	4.94(5)	4.42(5)
64.0(6)	P	1.06(5)	8.38(3)	4.94(5)	4.42(5)
82.0(8)	C	1.04(6)	8.90(3)	5.01(6)	4.46(5)
82.0(8)	P	1.06(6)	8.75(4)	5.00(5)	4.47(5)

hydrides. While these synthetic equations of state reflect the thermal expansion of the iron component, no additional adjustment was made to mimic the potential thermal expansion of the interstitial hydrogen, as this relationship is unconstrained. To our knowledge no experimental measurements of the density of liquid FeH_X exist, and approximations made on the basis of the known behavior of solids are the best available estimates. All CMB density calculations included a δV of +1.5% due to melting (Anderson and Isaak, 2000) and used CMB temperatures of 4000±500 K (Anderson, 2003). Based on these calculations, the density at the CMB can be matched by an *hcp* iron hydride alloy of 1.0–1.3 wt.% hydrogen or an *fcc* alloy containing 0.8–1.1 wt.% hydrogen. A similar density calculation was made to determine the maximum hydrogen content of the Earth's inner core based on matching PREM ICB density, using an ICB temperature of 5500±500 K (Anderson, 2003). This calculation indicated the ICB density can be matched an *hcp* iron hydride alloy of 0.4–0.6 wt.% hydrogen or an *fcc* alloy containing 0.2–0.3 wt.% hydrogen. Although the accuracy of the *fcc* iron equation of state is sufficient to determine the hydrogen contents in our FeH_X samples, which are close in pressure to the stability range of *fcc* iron, the extrapolation of the *fcc* equation of state to Earth core conditions is significant. As such, hydrogen core-content

Table 6.4: Birch's law parameters calculated using both *fcc* FeH_X equations of state rooted in the Caracas (2015) (denoted as 'C' below) and the Pépin et al. (2014) (denoted 'P') hydrogen volumes. Input sound velocities (V_P) have been calculated from NRIXS data using PHOENIX (Sturhahn, 2000) software, while parameters determined using V_P determined using Sciphon are in Table S2. Values in parentheses are uncertainties in last digit.

EoS	a ($km \cdot s^{-1}$)	b ($m^4 \cdot kg^{-1} \cdot s^{-1}$)	c (unitless)	Data included in fit
C	-4 (fixed)	1.206 (fixed)	1.72(8)	This study; Shibazaki et al. (2012); Mao et al. (1990)
C	-4 (fixed)	1.206 (fixed)	1.80(7)	This study
C	-5.1(7)	1.31(7)	2.0(2)	This study; Shibazaki et al. (2012); Mao et al. (1990); Antonangeli et al. (2012); Ohtani et al. (2013)
P	-4 (fixed)	1.206 (fixed)	1.73(9)	This study; Shibazaki et al. (2012); Mao et al. (1990)
P	-4 (fixed)	1.206 (fixed)	1.7(1)	This study
P	-4.9*)	1.30(7)	1.9(2)	This study; Shibazaki et al. (2012); Mao et al. (1990); Antonangeli et al. (2012); Ohtani et al. (2013)

estimates calculated using an *hcp* iron hydride alloy calculation to match PREM densities at the CMB and ICB (1.0–1.3 wt.% and 0.4–0.6 wt.%, respectively) are likely more accurate, as the *hcp* iron *P-V-T* relationship has been assessed up to inner core pressures.

Birch's law, effectively a linear extrapolation of the compressional wave velocity-density (V_P-ρ) relationship, has long been used to assess potential core constituent light elements (e.g., Badro et al. 2007). As hydrogen incorporation into the Earth's inner core is likely below 2 wt.%, our sound velocities of nonstoichiometric *fcc* FeH_X, as well as literature data for additional structures of FeH_X, were used to extrapolate the effect of hydrogen incorporation of FeH_X, using the relationship:

$$V_P = a + b\rho + cX \tag{6.5}$$

in which V_P is in units of $km \cdot s^{-1}$, density (ρ) is in units of $kg \cdot m^{-3}$, and stoichiometry (X) is in formula units. Two methods were used for this calculation. The first method fit experimental iron hydride data only (Thompson et al., 2018; Shibazaki et al., 2012; Mao

et al., 1990), holding the values of a and b fixed to -4000(11) $m \cdot s^{-1}$ and 1.206(11) $m^4 \cdot kg^{-1} \cdot s^{-1}$ respectively, adopting values reported by (Antonangeli and Ohtani, 2015) to describe the linear V_P-ρ relationship in pure iron which persists up to the pressure of Earth's inner core. In the second method, experimental iron hydride data (Thompson et al., 2018; Shibazaki et al., 2012; Mao et al., 1990), and *hcp* iron data (Antonangeli et al., 2012; Ohtani et al., 2013), were fitted together to the above equation, solving for all three parameters (a, b and c). Literature data for FeH_X were reassessed using the equations of state presented herein for self-consistency within these Birch's law parameterizations, including adjustments to stoichiometry, density, V_S and, in the case of NRIXS data, V_P. These two methods were repeated using NRIXS V_P results determined using both interstitial hydrogen equations of states reported in Table 1, and results of these Birch Law calculations are reported in Table 3 and Table S3.

An example of the first method is shown in Figure 6.4, in which the influence of hydrogen incorporation is added to the previously determined (V_P-ρ) relationship reported by Antonangeli et al. (2015), and only the new variable hydrogen stoichiometry parameter (c) is fit to 6.5. The resultant values of c reported herein reflect a significant influence of interstitial hydrogen on the V_P-ρ relationship of iron hydrides. The magnitude of this influence (i.e., values of c) are indistinguishable to those reported by Umemoto and Hirose (2015) based on molecular dynamics calculations. Similarly, the experimentally determined shear wave velocities (V_S) from this study were combined with literature values (Shibazaki et al., 2012; Mao et al., 1990, 1998; Lin et al., 2005b) to parameterize the influence of interstitial hydrogen on the shear wave velocity-density (V_S-ρ) relationship in iron hydrides (Equation S1, Table S4, Figure 6.5). The differences in V_S of FeH_X between studies are much higher than for V_P, and furthermore the unknown temperature effect on V_S is likewise greater than for V_P; consequently only the V_P-ρ parameterization is relied upon below to place limits on the inner core's hydrogen content.

Applying our Birch's Law parameterization (line 1 in Table 3) to ICB conditions suggests

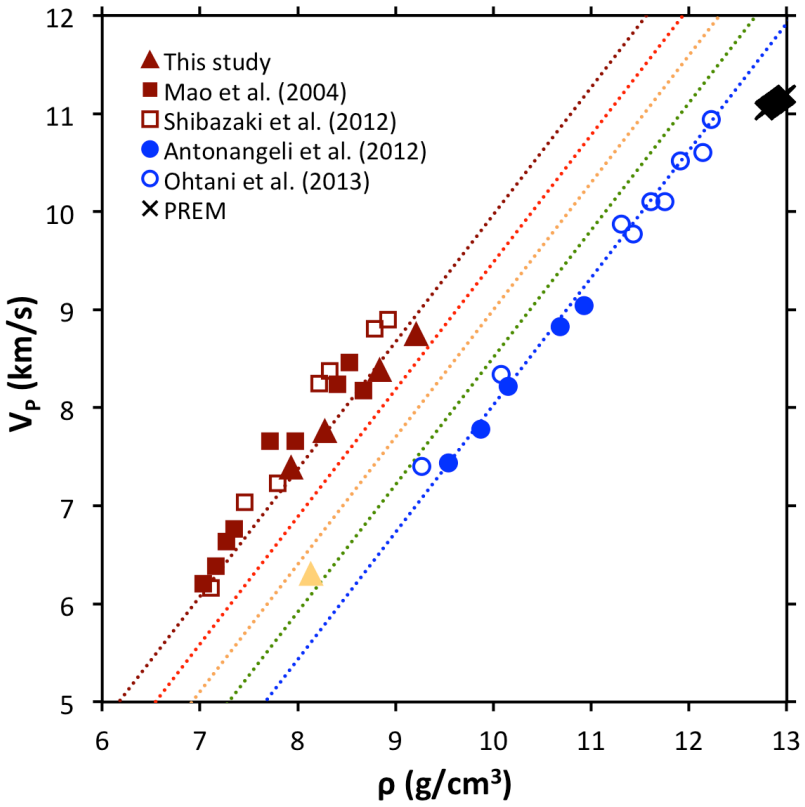

Figure 6.4: Birch's Law extrapolation of the influence of hydrogen stoichiometry on the velocity-density (V_P-ρ) relationship in iron hydrides. Dotted lines indicate Birch's law parameterization for varying FeH_X stoichiometries, including X=0 (blue), X=0.25 (green), X=0.5 (orange), X=0.75 (red), and X=1 (maroon). Experimental data includes *fcc* FeH_X (triangles), *dhcp* FeH_X (squares), and *hcp* iron (circles) and individual data points have been color coded to reflect the approximate sample stoichiometry. Error bars do not exceed the size of the symbol. This fit uses the hydrogen EoS based on Caracas (2015), sound velocities calculated using PHOENIX (Sturhahn, 2000), and Eq. 6.5. The PREM model for the inner core is represented by crosses and all non-PREM data reflects ambient temperatures.

hydrogen incorporation is irreconcilable with attempts to simultaneously match the density and compressional sound velocity of Earth's inner core, as hydrogen leads to increased values of V_P relative to pure iron at a given density (Figure 6.4). However, this is an incomplete view, as increased temperature has been shown to have the opposite effect - i.e., pure iron (X=0) at high temperatures has reduced sound velocities relative to 300 K iron at a fixed density (Decremps et al., 2014; Antonangeli et al., 2012; Lin et al., 2005b). Yet, although the literature reflects consensus on the general effect of temperature on the V_P-ρ relationship of iron, the magnitude and linearity of this effect remains contested (e.g., Antonangeli et al.

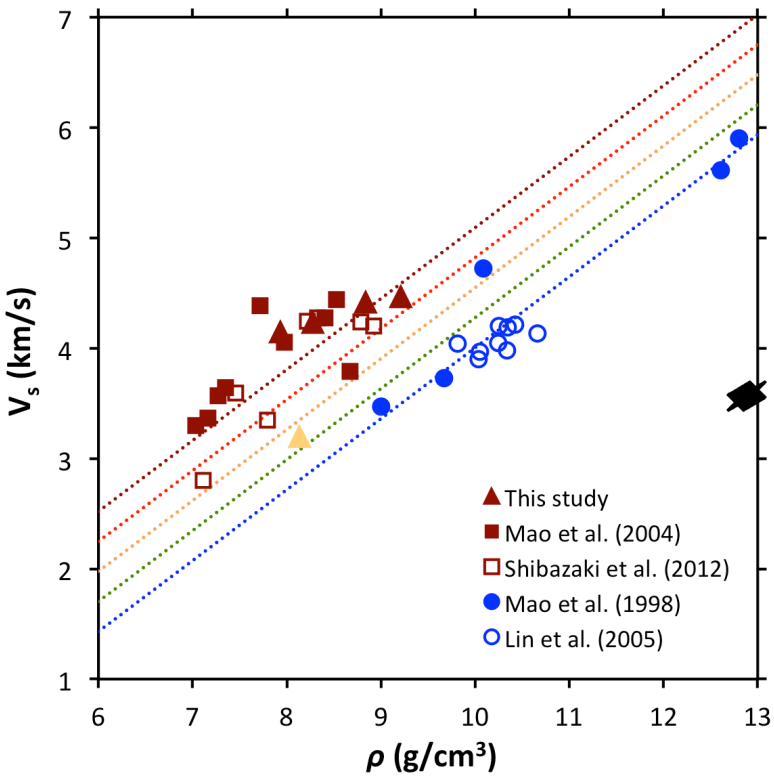

Figure 6.5: Birch's Law extrapolation of the influence of hydrogen stoichiometry on the V_S-ρ relationship in iron hydrides. Dotted lines indicate Birch's law parameterization for varying FeH_X stoichiometries, including X=0 (blue), X=0.25 (green), X=0.5 (orange), X=0.75 (red), and X=1 (maroon). Experimental data includes *fcc* FeH_X (triangles), *dhcp* FeH_X (squares), and *hcp* iron (circles), with data points color coded to their approximate stoichiometry. This fit uses the hydrogen EoS based on Caracas (2015), sound velocities calculated using PHOENIX (Sturhahn, 2000), and Eq. S1. The PREM model of the inner core at core temperature is represented by black crosses. Sample densities reflect minor isotopic variation (i.e., Fe^{57} enrichment) owing to different sample preparation methods and all experimental data reflect ambient temperatures.

2012; Lin et al. 2005b). Since there is no agreed upon temperature effect, here we evaluate the interplay between $\mathrm{d}V_P/\mathrm{d}T$ and the amount of hydrogen needed to satisfy PREM. To quantify this, a linear temperature effect (d), was added to the previously defined FeH_X V_P-ρ relationship (Eq. 6.5):

$$V_P = a + b\rho + cX + d(T - 300) \tag{6.6}$$

in which temperature (T) is in kelvin. The utility of adding a temperature-dependence

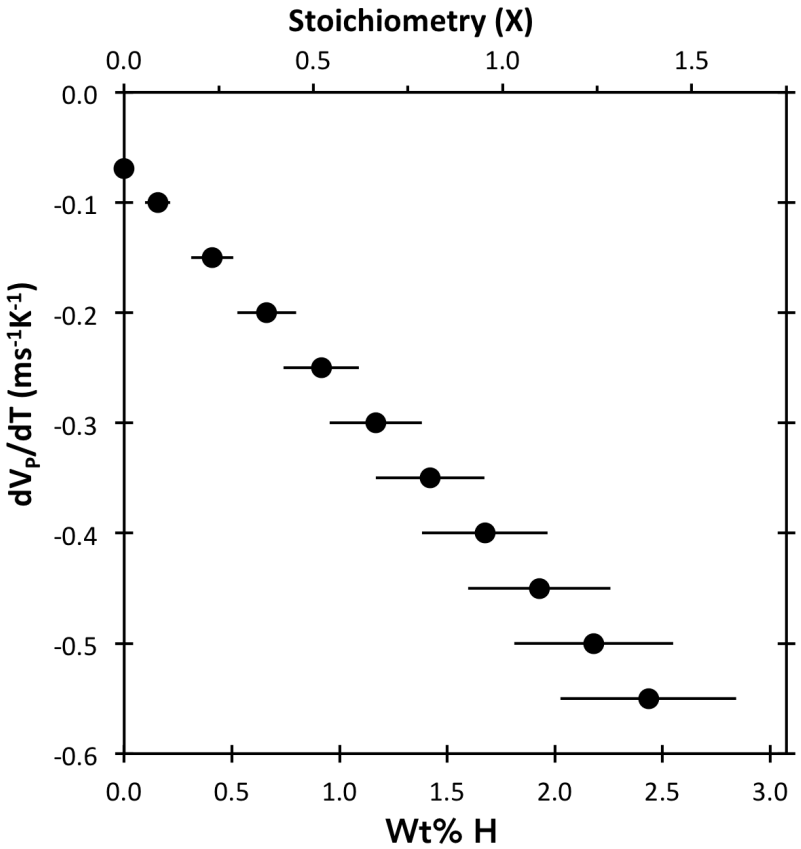

Figure 6.6: Trade-off between the influence of increased temperature on the compression wave velocity (V_P) of iron and the hydrogen content needed to match the V_P of the inner core boundary (ICB) based on Eq. 6.6. Modeled hydrogen contents are based on an ICB temperature of 5500 K with error bars reflecting ±500K.

term to a 300 K Birch's Law fitting has been previously demonstrated (e.g., Ohtani et al. 2013). Using Eq. 6.6, we evaluated the amount of hydrogen needed to reproduce PREM ICB density and compressional velocity at an ICB temperature of 5500±500 K (Figure 4). As shown in Figure 6.6, the greater the V_P reduction caused by high temperatures, the more hydrogen could be incorporated into the Earth's inner core while satisfying the density and velocity of PREM. It is unlikely that hydrogen could be the sole light element in Earth's core, because other candidate components (Si, O, S) are known to dissolve into the metal to varying degrees at high pressures and temperatures (e.g., Fischer et al. 2015). However, as shown in Figure 6.6, a hydrogen content of ∼0.8 to 1.3 wt.%, which satisfies the core density deficit as described above, also matches the V_P profile of the inner core if the mean

thermal reduction in velocity is -0.22 to -0.31 m $s^{-1} \cdot K^{-1}$ for the Fe-H iron alloy. This further illustrates that additional high temperature sound velocity measurements of solid iron and iron alloys are greatly needed to more accurately predict the light element content of Earth's core.

CHAPTER 7

IMPLICATIONS AND CONCLUSIONS

This thesis traces a hypothetical path of hydrogen transport through the Earth's lower mantle to the outer core, probing phase stability and determining the geophysical properties of these phases (e.g. density and sound velocities), with a goal of refining our understanding of the distribution of hydrous phases in the deep Earth. In Chapter 2, I described the influence of Al-substitution on the stability, hydrogen-bonding, and elasticity of Al-bearing phase D [$(Mg,Al)(Si,Al)_2O_4(OH)$]. Chapter 3 explores the geophysical properties (e.g. density, sound velocities) of ε-FeOOH determined using density functional theory-based calculations, as well the properties of the solid solution formed by ε-FeOOH, δ-AlOOH, and phase H [$MgSiO_4H_2$]–phase H being the high-pressure product of phase D. Building on this theoretical study, Chapter 4 provided an experimental approach to parsing the pressures at which pressure-induced hydrogen bond symmetrization and the spin transition occur in ε-FeOOH. At even higher pressures (>60 GPa, or mid-mantle pressures in Earth) ε-FeOOH transforms to pyrite type FeO_2H. Chapter 5 employs the computational methodology of Chapter 3 to probe this higher pressure structure, similarly probing the geophysical properties of the solid solution formed with pyrite-type AlO_2H. Pyrite-type FeO_2H is predicted to be stable to the pressure of the core-mantle boundary (CMB), and reactions of hydrous phases with iron have been previously shown to result in the formation of iron hydrides (Yagi and Hishinuma, 1995). Chapter 6 describes the properties of *fcc* FeH_X and the influence of interstitial hydrogen on the density and sound velocities iron at high pressures and temperatures. By probing the properties of idealized endmember compositions, but complementing these determinations with calculations of the properties of solid solutions, this thesis aims to contribute to a more realistic assessment of hydrogen accommodation in the Earth's interior.

Aluminum substitution has been shown to increase the thermodynamic stability of phase D (Sano et al., 2008; Ohira et al., 2014; Pamato et al., 2015), and aluminum-rich phase D is a likely precursor to the solid solution formed by Phase H and δ-AlOOH. However, while the

elasticity of the Mg-endmember composition of phase D [$MgSi_2O_4(OH)_2$] has been calculated (Tsuchiya et al., 2005), neither the elasticity of Al-endmember phase D [$Al_2SiO_4(OH)_2$] or intermediate solid solutions [$(Mg,Al)(Si,Al)_2O_4(OH)_2$] had been determined. My collaborators and I evaluated the elasticity of of the Al-endmember as well as two cation configurations of the intermediate solid solution with 50% Al-substitution. We also re-evaluated the elasticity of the Mg-endmember to enable direct comparison between compositions. Based on these calculations we determined that although both Mg- and Al-endmember compositions of phase D undergo pressure induced hydrogen bond symmetrization, neither of the evaluated configurations of the intermediate composition do. This is significant, as hydrogen bond symmetrization leads to an increase in the bulk modulus of 14% and 22% for the Al- and Mg-endmembers respectively. The elastic constants, moduli, and sound velocities of the intermediate compositions also differed substantially from what would have been obtained by interpolation between endmember compositions. This finding most likely generalizes to other phases, and indicates a need for caution when drawing conclusions about the properties of solid solutions based on studies of endmembers alone. Future high-temperature experiments or molecular dynamics calculations should explore the extent to which hydrogen bond symmetrization might dampen anharmonic effects, as this might further differentiate the behavior of intermediate solid solutions at elevated P-T conditions from the behavior expected based on the interpolation of the endmember compositions.

My coauthors and I calculated the structure and elasticity of low-spin ferromagnetic ε-FeOOH to 140 GPa using density functional theory calculations with a Coulombic self-interaction term (U) (Thompson et al., 2017). Using these data, the elastic moduli and sound velocities of ε-FeOOH were calculated across the pressure stability of the hydrogen bond symmeterized structure (30 to 140 GPa). The obtained values were compared with previously published values for δ-AlOOH and phase H [$MgSiO_4H_2$], which form a solid solution with ε-FeOOH. In contrast to these Mg and Al endmembers, ε-FeOOH has smaller diagonal and larger off-diagonal elastic constants, leading to an eventual negative pressure

dependence of its shear wave velocity. Because of this behavior, iron-enriched solid solutions from this system have smaller shear wave velocities than surrounding mantle and therefore are a plausible contributor to large low-shear velocity provinces (LLSVPs) which exhibit similar seismic properties. Additionally, ε-FeOOH has substantial shear wave polarization anisotropy. Consequently, if iron-rich solid solutions from the FeOOH–AlOOH–$MgSiO_4H_2$ system at the core-mantle boundary exhibit significant lattice-preferred orientation due to the strong shear stresses which occur there, it may help explain the $S_H > S_V$ anisotropy seismically observed in this region.

In the course of calculating the elasticity of ε-FeOOH, we determined that hydrogen bond symmetrization and the associated $P2_1nm \rightarrow Pnnm$ phase transition occurred at significantly lower pressures in low-spin ferromagnetic ε-FeOOH than had previously been reported (Gleason et al., 2013). In order to resolve this discrepancy, my collaborators and I embarked on an experimental study of the properties of ε-FeOOH at high pressure (0-70 GPa). Based on these experiments, we determined that there are two distinct phase transitions in ε-FeOOH in the pressure range we explored. First, at 17.5±1 GPa ε-FeOOH undergoes the $P2_1nm \rightarrow Pnnm$ symmetry transition, which we determined based on FTIR observations of a change in the OH-bending modes, a transient decrease in optical absorption, and a change in axial compressibility. At 45 GPa, *Pnnm* ε-FeOOH undergoes a second structural transition to an as-of-yet unidentified structure, identified by the appearance of new Bragg peaks as well as the disappearance of previously identified *Pnnm* peaks. This structural transition occurs at the same pressure as the previously observed spin transition in this phase (Gleason et al., 2013), as well as our own observations of a reduction in FTIR transmission and an increase in optical absorption. Based on these observations, it is unlikely that hydrogen bond symmetrization induces a spin transition in ε-FeOOH as has previously been reported (Gleason et al., 2013), as the $P2_1nm \rightarrow Pnnm$ symmetry transition associated with hydrogen bond symmetrization occurs ∼30 GPa below the spin transition pressure reported by Gleason et al. (2013).

Using density functional theory based computations, my collaborators and I determined the stability, structure, and elastic properties of pyrite-type FeO_2H. The structure, transition pressure, and equation of state of this phase was compared to that of pyrite-type AlO_2H, with which it forms a solid solution. Based on the substantial difference in the transition pressures of the Fe- and Al-endmembers (70 and 195 GPa, respectively), the stability field of this solid solution is expected to be strongly compositionally dependent. Two structures of (Al,Fe)OOH may coexist in the lower mantle: (1) pyrite-type $Al_XFe_{1-X}O_2H$ with X<0.5, and (2) $CaCl_2$-type $(Al_X,Fe_{1-X})OOH$ with X>0.5. These two structures have very different seismic signatures in terms of both shear wave velocity (V_S) and shear wave polarization. Pyrite-type $(Al,Fe)O_2H$ is characterized by moderately reduced shear wave velocities and a low degree of shear wave polarization, while $CaCl_2$-type (Al,Fe)OOH exhibits V_S reduced up to 11% compared to its pyrite counterpart and strongly horizontally polarized shear waves. Owing to the vastly different properties of this solid solution depending on its structure, which is compositionally driven at lower mantle pressures, interpretations concerning the contribution of pyrite-type FeO_2H to seismically observed features (e.g., ULVZs) must take into account complications arising from compositional variation to be considered robust. With this in mind, our 0K calculations of pyrite-structured $(Al_{0.4\text{-}0.5},Fe_{0.6\text{-}0.5})O_2H$ simultaneously reproduce the ∼10% V_P and 10-30% V_S reductions characteristic of ULVZs. Furthermore, Fe-rich pyrite-type $(Al,Fe)O_2H$ may contribute to observed ULVZs without any dehydrogenation needed to match seismic observations.

In order to probe the influence of interstitial hydrogen on the geophysical properties of iron at high pressure, my coauthors and I synthesized face centered cubic (*fcc*) FeH_X at pressures of 18 to 68 GPa and temperatures exceeding 1500 K (Thompson et al., 2018). Thermally quenched FeH_X samples were evaluated using synchrotron X-ray diffraction and nuclear resonant inelastic X-ray scattering to determine sample composition and sound velocities to 82 GPa. To aid in the interpretation of non-ideal (X≠1) stoichiometries, two equations of state for *fcc* FeH_X were developed, combining an empirical equation of state

for iron with two distinct synthetic compression curves for interstitial hydrogen. Matching the density deficit of the Earth's core using these equations of state requires 0.8-1.1 wt.% hydrogen at the core-mantle boundary and 0.2-0.3 wt.% hydrogen at the interface of the inner and outer cores. Furthermore, a comparison of Preliminary Reference Earth Model (PREM) (Dziewonski and Anderson, 1981) to a Birch's law extrapolation of our experimental results suggests that an iron alloy containing 0.8 to 1.3 wt.% hydrogen could reproduce both the density and compressional velocity (V_P) of the Earth's outer core. Additionally, if metallic iron exits within the Earth's lower mantle (e.g., Frost et al. 2004; Smith et al. 2016), the reaction of water or hydrogen-bearing phases with this iron may produce iron hydride. However, experiments probing these types of reactions remain limited (e.g., Yuan et al. 2018a), as is our understanding of the extent to which metallic iron exists in the lower mantle.

The quantity and distribution of hydrogen in the deep Earth remains incompletely understood, but mineral physics experiments and theoretical calculations are making strides in constraining these long outstanding unknowns. Some of the hydrogen-bearing phases discussed in this thesis were only identified in the past decade, including phase H (Tsuchiya, 2013; Nishi et al., 2014), pyrite-type FeO_2H (Hu et al., 2016), and pyrite-type AlO_2H (Tsuchiya and Tsuchiya, 2011). In other cases, a hydrogen-bearing deep Earth phase has been identified but new approaches are needed to evaluate the its stability and/or properties. Phase D was identified more than 30 years ago (Liu, 1987) and the Mg-endmember composition is relatively well studied, but the careful evaluation of the influence of cation substitution and solid solutions in high-pressure hydrous phases is a a relatively recent endeavor (e.g., Pamato et al. 2015; Panero and Caracas 2009). Iron hydrides including *fcc* FeH_X have been known to form from the high-pressure, high-temperature reaction of iron hydrous phases for over 20 years (Yagi and Hishinuma, 1995), but there remained a paucity of data with which to constrain the influence of interstitial hydrogen on the sound velocities of iron. In this case, the increased capabilities of nuclear resonant inelastic X-ray scattering are driving

this research forward, and I expect additional high-pressure and hopefully high-temperature data to continue to advance our understanding of hydrogen as a potential light element in the core. Lastly, there are times when it appears a system is already well understood, but in reevaluating the system with a different toolset it becomes evident the initial solution was incomplete–in essence, replication turns to reassessment. This is the case with ε-FeOOH, in which it had recently been established that hydrogen bond symmetrization induced a spin transition at high pressures (Gleason et al., 2013). But in the course of evaluating the elasticity of this phase using DFT calculations, we discovered that hydrogen bond symmetrization occurs at much lower pressures than that study indicated, and by following up experimentally confirmed that the hydrogen bond symmetrization and spin transition are not coupled, as had been previously reported (Yuan et al., 2018a). Looking forward, I expect minerals physics to continue to produce necessary constraints on the hydration of the Earth's deep interior by means of discovery, by making more nuanced analyses of complex systems, and by conscientiously validating the work of others who have come before.

APPENDIX A

ALUMINIUM SUBSTITUTION IN PHASE D

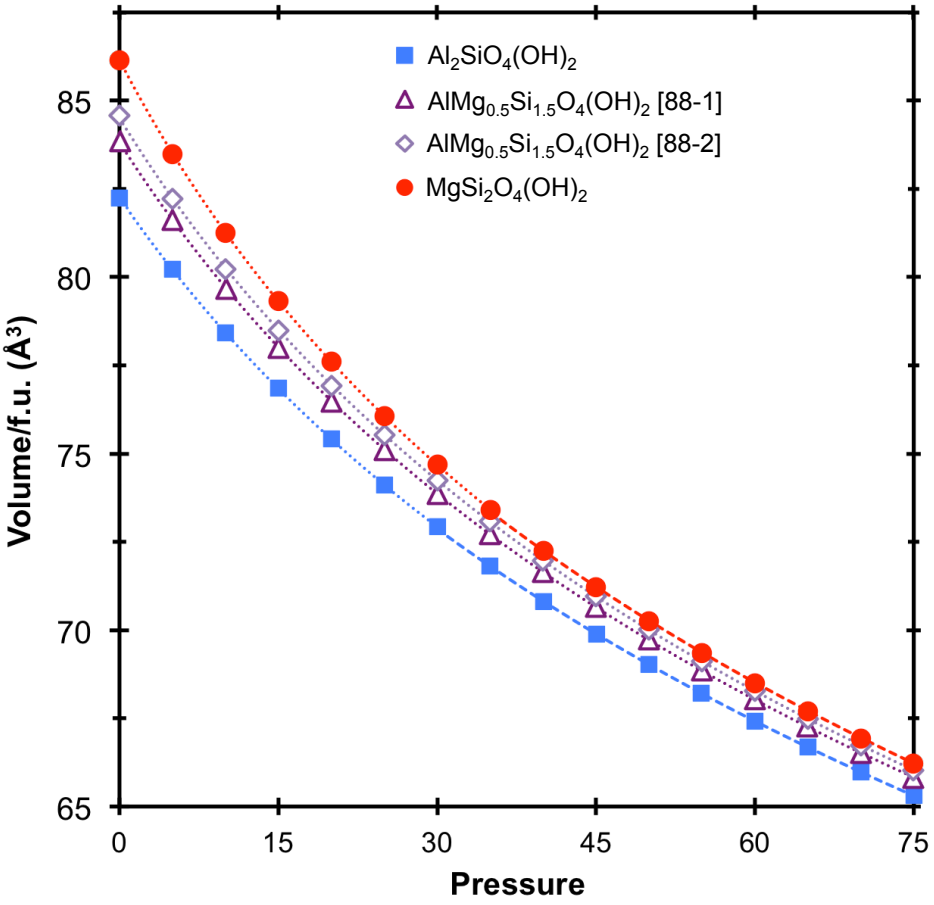

Figure A.1: Formula unit (f.u.) volumes of the optimized structures of $MgSi_2O_4(OH)_2$ (solid red circles), $Al_2SiO_4(OH)_2$ phase D (solid blue squares), $AlMg_{0.5}Si_{1.5}O_4(OH)_2$ in the 88-1 structure (open dark purple triangles), and $AlMg_{0.5}Si_{1.5}O_4(OH)_2$ in the 88-2 structure (open lavender diamonds). Dotted lines indicate equation of states (EOSs) fit to pre-hydrogen bond symmetrization structures (lines 3, 9, 13, and 15 of Table 2.1). Dashed lines are EOSs fit to post-hydrogen bond symmetrization structures (lines 5 and 11 of Table 2.1).

.

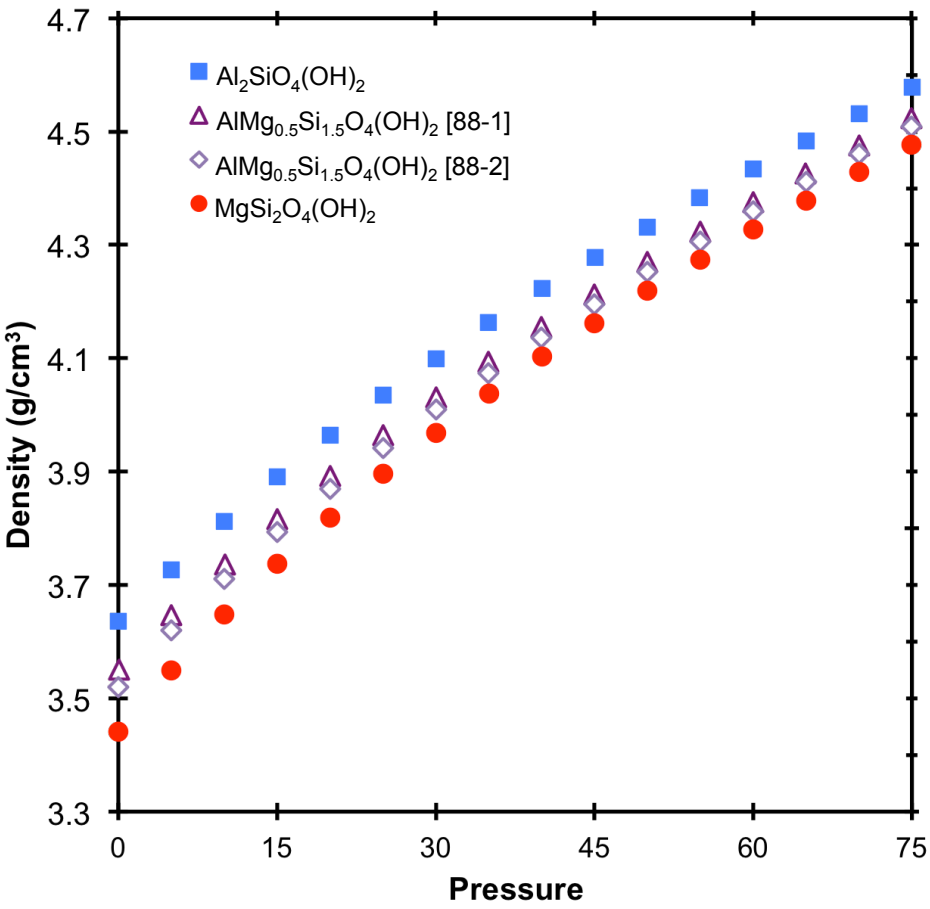

Figure A.2: Density of the optimized structures of $MgSi_2O_4(OH)_2$ (solid red circles), $Al_2SiO_4(OH)_2$ phase D (solid blue squares), $AlMg_{0.5}Si_{1.5}O_4(OH)_2$ in the 88-1 structure (open dark purple triangles), and $AlMg_{0.5}Si_{1.5}O_4(OH)_2$ in the 88-2 structure (open lavender diamonds).

.

Table A.1: Atomic positions in $MgSi_2O_4(OH)_2$ at 0 GPa. Atomic positions (X, Y, Z) are in units of fractional unit cells.

Atom	X	Y	Z
Mg	0.028620	0.023768	0.975729
Si	0.347702	0.658947	0.508795
Si	0.663789	0.342861	0.508793
O	0.638624	0.007447	0.255687
O	0.012286	0.633783	0.255686
O	0.364646	0.359806	0.283017
O	0.389340	0.003503	0.722073
O	0.008345	0.384497	0.722074
O	0.661872	0.657030	0.713433
H	0.528067	0.000198	0.049481
H	0.005037	0.523219	0.049482

Table A.2: Atomic positions in $Al_2SiO_4(OH)_2$ at 0 GPa. Atomic positions (X, Y, Z) are in units of fractional supercell, which has been doubled along the *c*-axis (i.e., the Z direction).

Atom	X	Y	Z
Al	0.026542	0.025246	0.488610
Al	0.348302	0.664052	0.252579
Si	0.664396	0.344483	0.255085
O	0.662522	0.020607	0.122531
O	-0.000753	0.646637	0.121026
O	0.352439	0.330242	0.134030
O	-0.005662	0.021132	0.372155
O	0.008345	0.353860	0.369841
O	0.694481	0.674300	0.361957
H	0.530647	0.006447	0.018271
H	0.000892	0.520245	0.018077
Al	0.029669	0.022128	0.988607
Si	0.348912	0.660008	0.755084
Al	0.668490	0.343930	0.752574
O	0.651055	-0.005148	0.621028
O	0.025027	0.658129	0.622522
O	0.334662	0.348048	0.634028
O	0.358290	-0.010052	0.869836
O	0.025561	0.690086	0.872153
O	0.678729	0.674300	0.861956
H	0.524663	-0.003512	0.518074
H	0.010857	0.526234	0.518265

Table A.3: Atomic positions in the 88-1 structure of $AlMg_{0.5}Si_{1.5}O_4(OH)_2$ at 0 GPa. Atomic positions (X, Y, Z) are in units of fractional supercell, which has been doubled along the *a*-, *b*-, and *c*-axis.

	X	Y	Z		X	Y	Z		X	Y	Z		X	Y	Z
Al	0.0167	0.0078	0.5008	Mg	0.0021	0.5114	0.5128	Mg	0.5021	0.0114	0.5128	Al	0.5167	0.5078	0.5008
Si	0.1753	0.3360	0.2484	Si	0.1641	0.8453	0.2500	Si	0.6641	0.3453	0.2500	Si	0.6753	0.8360	0.2484
Si	0.3311	0.1742	0.2539	Al	0.3409	0.6822	0.2493	Al	0.8409	0.1822	0.2493	Si	0.8311	0.6742	0.2539
O	0.3191	0.0093	0.1412	O	0.3274	0.5031	0.1190	O	0.8274	0.0031	0.1190	O	0.8191	0.5093	0.1412
O	0.0195	0.3355	0.1528	O	0.0001	0.8297	0.1260	O	0.5001	0.3297	0.1260	O	0.5195	0.8355	0.1528
O	0.1734	0.1782	0.1416	O	0.1851	0.6989	0.1355	O	0.6851	0.1989	0.1355	O	0.6734	0.6782	0.1416
O	0.1773	0.0090	0.3675	O	0.1933	0.5014	0.3744	O	0.6933	0.0014	0.3744	O	0.6773	0.5090	0.3675
O	0.0140	0.1844	0.3879	O	0.0017	0.6957	0.3652	O	0.5017	0.1957	0.3652	O	0.5140	0.6844	0.3879
O	0.3344	0.3380	0.3570	O	0.3151	0.8294	0.3817	O	0.8151	0.3294	0.3817	O	0.8344	0.8380	0.3570
H	0.2487	0.0138	-0.0099	H	0.2643	0.4990	0.0127	H	0.7643	-0.0010	0.0127	H	0.7487	0.5138	-0.0099
H	-0.2304	0.2602	-0.0144	H	0.0024	0.7499	-0.0212	H	0.5024	0.2499	-0.0212	H	0.2696	0.7602	-0.0144
Al	0.0089	0.0155	1.0008	Mg	0.0126	0.5009	1.0128	Mg	0.5126	0.0009	1.0128	Al	0.5089	0.5155	1.0008
Si	0.1754	0.3299	0.7539	Al	0.1834	0.8397	0.7493	Al	0.6834	0.3397	0.7493	Si	0.6754	0.8299	0.7539
Si	0.3372	0.1741	0.7484	Si	0.3465	0.6629	0.7500	Si	0.8465	0.1629	0.7500	Si	0.8372	0.6741	0.7484
O	0.3367	0.0183	0.6528	O	0.3309	0.4989	0.6260	O	0.8309	-0.0011	0.6260	O	0.8367	0.5183	0.6528
O	0.0105	0.3179	0.6412	O	0.0043	0.8262	0.6190	O	0.5043	0.3262	0.6190	O	0.5105	0.8179	0.6412
O	0.1793	0.1722	0.6416	O	0.1969	0.5005	0.8652	O	0.7001	0.1839	0.6355	O	0.6856	0.5128	0.8879
O	0.1856	0.0128	0.8879	O	0.0026	0.6921	0.8744	O	0.6969	0.0005	0.8652	O	0.5102	0.6761	0.8675
O	0.0102	0.1761	0.8675	O	0.3306	0.8139	0.8817	O	0.5026	0.1921	0.8744	O	0.8392	0.8332	0.8570
O	0.3392	0.3332	0.8570	O	0.2001	0.6839	0.6355	O	0.8306	0.3139	0.8817	O	0.6793	0.6722	0.6416
H	0.2614	0.7684	0.4856	H	0.2511	0.5012	0.4788	H	0.7511	1.0012	0.4788	H	0.7614	0.2684	0.4856
H	0.0150	0.2475	0.4901	H	0.0001	0.7631	0.5127	H	0.5001	0.2631	0.5127	H	0.5150	0.7475	0.4901

Table A.4: Atomic positions in the 88-2 structure of $AlMg_{0.5}Si_{1.5}O_4(OH)_2$ at 0 GPa. Atomic positions (X, Y, Z) are in units of fractional supercell, which has been doubled along the *a*-, *b*-, and *c*-axis.

	X	Y	Z		X	Y	Z		X	Y	Z		X	Y	Z
Al	0.0124	0.0007	0.5029	Al	0.0038	0.5037	0.5214	Al	0.5038	0.0037	0.5214	Al	0.5124	0.5007	0.5029
Al	0.1733	0.3366	0.2481	Si	0.1746	0.8521	0.2563	Si	0.6746	0.3521	0.2563	Al	0.6733	0.8366	0.2481
Si	0.3218	0.1724	0.2534	Al	0.3477	0.6795	0.2543	Al	0.8477	0.1795	0.2543	Si	0.8218	0.6724	0.2534
O	0.3223	0.0076	0.1463	O	0.3251	0.5104	0.1281	O	0.8251	0.0104	0.1281	O	0.8223	0.5076	0.1463
O	0.0077	0.3377	0.1511	O	0.0043	0.8163	0.1347	O	0.5043	0.3163	0.1347	O	0.5077	0.8377	0.1511
O	0.1839	0.1779	0.1402	O	0.1857	0.6981	0.1395	O	0.6857	0.1981	0.1395	O	0.6839	0.6779	0.1402
O	0.1780	0.0050	0.3699	O	0.1806	0.5113	0.3899	O	0.6806	0.0113	0.3899	O	0.6780	0.5050	0.3699
O	0.0065	0.1744	0.3896	O	0.0115	0.6871	0.3780	O	0.5115	0.1871	0.3780	O	0.5065	0.6744	0.3896
O	0.3468	0.3358	0.3663	O	0.3254	0.8380	0.3888	O	0.8254	0.3380	0.3888	O	0.8468	0.8358	0.3663
H	0.2521	0.0124	-0.0239	H	0.2664	0.5043	0.0277	H	0.7664	0.0043	0.0277	H	0.7521	0.5124	-0.0239
H	-0.2578	0.2492	0.0367	H	0.0035	0.7629	0.0280	H	0.5035	0.2629	0.0280	H	0.2422	0.7492	0.0367
Mg	0.0090	0.0247	0.9932	Mg	0.0065	0.4886	0.9983	Mg	0.5065	-0.0114	0.9983	Mg	0.5090	0.5247	0.9932
Si	0.1802	0.3350	0.7512	Si	0.1778	0.8361	0.7506	Si	0.6778	0.3361	0.7506	Si	0.6802	0.8350	0.7512
Si	0.3457	0.1800	0.7450	Si	0.3463	0.6705	0.7534	Si	0.8463	0.1705	0.7534	Si	0.8457	0.6800	0.7450
O	0.3364	0.0058	0.6432	O	0.3293	0.5024	0.6262	O	0.8293	0.0024	0.6262	O	0.8364	0.5058	0.6432
O	0.0030	0.3289	0.6287	O	0.0150	0.8291	0.6282	O	0.5150	0.3291	0.6282	O	0.5030	0.8289	0.6287
O	0.1816	0.1713	0.6366	O	0.1977	0.5061	0.8593	O	0.6819	0.1817	0.6305	O	0.6981	0.5076	0.8720
O	0.1981	0.0076	0.8720	O	0.0097	0.6971	0.8647	O	0.6977	0.0061	0.8593	O	0.5113	0.6951	0.8541
O	0.0113	0.1951	0.8541	O	0.3178	0.8148	0.8662	O	0.5097	0.1971	0.8647	O	0.8326	0.8278	0.8530
O	0.3326	0.3278	0.8530	O	0.1819	0.6817	0.6305	O	0.8178	0.3148	0.8662	O	0.6816	0.6713	0.6366
H	0.2603	0.7709	0.4846	H	0.2465	0.5080	0.4853	H	0.7465	1.0080	0.4853	H	0.5093	0.7408	0.4864
H	0.0093	0.2408	0.4864	H	0.0094	0.7484	0.4797	H	0.5094	0.2484	0.4797	H	0.7603	0.2709	0.4846

Table A.5: Average lattice parameters c and a of Mg-endmember phase D (Mg-phD), Al-endmember phase D (Al-phD), and tie-line composition in the 88-1 and 88-2 structures as a function of pressure from 0 to 75 GPa.

P (GPa)	Mg-phD		88-1		88-2		Al-phD	
	c	a	c	a	c	a	c	a
0	4.368	4.787	4.262	4.776	4.293	4.784	4.196	4.785
5	4.303	4.750	4.217	4.738	4.242	4.744	4.155	4.749
10	4.249	4.717	4.177	4.703	4.200	4.709	4.119	4.715
15	4.203	4.686	4.143	4.672	4.163	4.677	4.086	4.686
20	4.162	4.658	4.112	4.644	4.130	4.648	4.057	4.658
25	4.127	4.633	4.085	4.617	4.103	4.620	4.033	4.633
30	4.094	4.609	4.060	4.593	4.077	4.596	4.003	4.608
35	4.065	4.586	4.038	4.570	4.053	4.572	3.986	4.585
40	4.038	4.565	4.017	4.548	4.031	4.551	3.967	4.564
45	4.017	4.544	3.998	4.528	4.010	4.530	3.950	4.543
50	3.998	4.524	3.980	4.508	3.991	4.510	3.934	4.524
55	3.981	4.505	3.963	4.490	3.973	4.491	3.919	4.506
60	3.964	4.487	3.946	4.472	3.956	4.473	3.905	4.488
65	3.948	4.470	3.931	4.455	3.940	4.456	3.891	4.471
70	3.933	4.454	3.916	4.439	3.924	4.440	3.878	4.455
75	3.918	4.438	3.903	4.423	3.910	4.424	3.865	4.439

Table A.6: Difference between the hydroxyl bond length ($r_{O—H}$) and the hydrogen bond length ($r_{O\cdots H}$) in Mg-endmember phase D (Mg-phD), Al-endmember phase D (Al-phD), and tie-line composition in the 88-1 and 88-2 structures as a function of pressure from 0 to 75 GPa.

P (GPa)	Mg-phD	Al-phD		88-1				88-2			
0	0.542	0.406	0.409	0.424	0.407	0.426	0.338	0.501	0.598	0.593	0.579
5	0.475	0.357	0.365	0.395	0.368	0.373	0.292	0.445	0.533	0.527	0.538
10	0.416	0.310	0.323	0.369	0.334	0.324	0.251	0.400	0.476	0.475	0.507
15	0.363	0.263	0.283	0.348	0.305	0.280	0.219	0.364	0.422	0.431	0.482
20	0.313	0.215	0.241	0.330	0.278	0.237	0.193	0.334	0.371	0.396	0.461
25	0.263	0.184	0.211	0.314	0.254	0.198	0.174	0.315	0.333	0.370	0.453
30	0.210	0.124	0.162	0.300	0.231	0.163	0.159	0.292	0.300	0.342	0.437
35	0.151	0.038	0.095	0.287	0.211	0.134	0.147	0.274	0.271	0.319	0.423
40	0.063	0.000	0.001	0.276	0.193	0.111	0.136	0.256	0.240	0.296	0.410
45	0.002	0.000	0.000	0.266	0.177	0.094	0.127	0.242	0.213	0.278	0.399
50	0.001	0.000	0.000	0.257	0.164	0.082	0.119	0.228	0.185	0.260	0.388
55	0.000	0.000	0.000	0.249	0.152	0.073	0.111	0.217	0.161	0.245	0.379
60	0.000	0.000	0.000	0.242	0.141	0.066	0.104	0.207	0.138	0.232	0.370
65	0.000	0.000	0.000	0.235	0.132	0.061	0.098	0.198	0.120	0.220	0.363
70	0.000	0.000	0.000	0.228	0.124	0.056	0.093	0.190	0.104	0.209	0.355
75	0.000	0.000	0.000	0.223	0.117	0.053	0.088	0.183	0.093	0.200	0.349

Table A.7: Bond angle of H—O···H as a function of pressure in Mg-endmember phase D (Mg-phD), Al-endmember phase D (Al-phD), and tie-line composition in the 88-1 and 88-2 structures as a function of pressure from 0 to 75 GPa.

P (GPa)	Mg-phD	Al-phD		88-1				88-2			
0	175.0	175.7	177.8	179.3	173.5	174.8	174.1	175.6	175.0	174.6	172.3
5	176.0	176.5	178.2	179.4	174.1	175.5	174.5	176.0	175.8	174.9	172.8
10	176.8	177.2	178.5	179.4	174.6	176.1	174.7	176.3	176.3	175.0	173.2
15	177.5	177.7	178.8	179.3	174.9	176.6	174.9	176.6	176.7	175.0	173.5
20	178.0	178.3	179.0	179.2	175.2	177.0	175.0	176.7	176.9	174.2	173.7
25	178.5	178.9	179.7	179.1	175.4	177.3	175.0	177.0	174.8	174.2	174.7
30	178.9	179.2	179.7	179.1	175.6	177.6	175.0	177.1	174.9	174.2	174.7
35	179.3	179.8	179.8	179.0	175.8	177.7	175.0	177.2	175.0	174.2	174.6
40	179.7	180.0	180.0	178.9	175.9	177.8	175.0	177.2	175.1	174.2	174.6
45	180.0	180.0	180.0	178.9	176.0	177.9	175.0	177.2	175.2	174.1	174.5
50	180.0	180.0	180.0	178.8	176.0	177.9	175.0	177.2	175.2	174.0	174.5
55	180.0	180.0	180.0	178.8	176.1	177.9	174.9	177.2	175.2	173.9	174.4
60	180.0	180.0	180.0	178.8	176.1	177.8	174.9	177.2	175.3	173.8	174.3
65	180.0	180.0	180.0	178.8	176.1	177.8	174.8	177.1	175.2	173.7	174.2
70	180.0	180.0	180.0	178.7	176.2	177.8	174.8	177.1	175.2	173.6	174.1
75	180.0	180.0	180.0	178.7	176.2	177.7	174.8	177.1	175.2	173.4	174.0

Table A.8: Elastic constants of Mg-endmember phase D as a function of pressure, in units of GPa, Part 1 of 2

P (GPa)	C_{11}	C_{22}	C_{33}	C_{44}	C_{55}	C_{66}	C_{12}	C_{13}	C_{14}	C_{15}	C_{16}
0.01	384	376	265	96	93	108	114	48	3	-2	71
5.01	418	411	307	111	108	122	129	64	5	-4	79
10.01	450	444	344	125	120	129	143	81	5	-7	83
15.01	481	475	381	137	132	136	158	97	6	-9	87
19.99	511	504	417	149	144	142	173	113	7	-11	91
25.00	536	531	448	161	156	145	187	127	8	-11	94
30.00	567	561	486	171	165	153	203	151	9	-14	98
35.00	594	588	525	182	176	157	218	168	9	-16	101
40.01	621	615	632	193	186	162	233	184	10	-17	104
44.98	646	639	671	201	194	166	247	201	11	-19	107
50.00	671	664	697	209	201	170	261	217	12	-21	109
54.98	695	687	720	216	208	174	275	232	12	-22	112
60.00	719	710	744	224	215	177	289	248	13	-24	114
64.97	739	732	763	230	222	179	303	263	13	-26	117
70.01	765	756	791	238	229	184	317	278	14	-27	119
74.97	787	778	813	244	235	187	331	293	14	-29	121

Table A.9: Elastic constants of Mg-endmember phase D as a function of pressure, in units of GPa, Part 2 of 2

P (GPa)	C_{23}	C_{24}	C_{25}	C_{26}	C_{34}	C_{35}	C_{36}	C_{45}	C_{46}	C_{56}
0.01	50	10	11	-71	27	21	5	-25	21	15
5.01	67	8	14	-77	27	22	6	-30	25	16
10.01	84	7	16	-81	27	22	8	-33	27	17
15.01	101	6	17	-85	28	22	9	-37	29	17
19.99	119	6	19	-90	28	23	10	-40	31	18
25.00	132	6	21	-93	28	23	10	-43	32	19
30.00	155	4	23	-97	29	23	10	-46	34	19
35.00	173	4	24	-100	29	23	11	-49	36	19
40.01	192	3	26	-104	30	25	14	-51	38	20
44.98	209	3	27	-106	31	25	14	-54	40	21
50.00	224	2	29	-109	31	25	14	-56	42	22
54.98	240	1	31	-112	31	25	15	-58	43	23
60.00	255	0	32	-114	31	25	15	-60	45	23
64.97	270	0	35	-115	33	27	15	-61	48	25
70.01	286	-1	35	-119	31	26	15	-63	48	25
74.97	301	-2	37	-121	32	26	16	-65	50	26

Table A.10: Elastic constants of Al-endmember phase D as a function of pressure, in units of GPa, Part 1 of 2

P (GPa)	C_{11}	C_{22}	C_{33}	C_{44}	C_{55}	C_{66}	C_{12}	C_{13}	C_{14}	C_{15}	C_{16}
0.01	410	411	379	185	169	110	118	83	1	30	75
5.00	448	449	414	206	189	119	130	102	1	26	82
10.01	484	484	447	225	205	128	143	121	0	25	88
15.01	515	516	479	242	221	135	156	139	0	25	93
20.00	546	546	513	259	235	144	170	157	0	26	98
24.99	574	575	551	275	250	149	182	173	0	26	102
29.99	606	606	638	292	266	157	197	200	0	28	107
35.00	633	632	651	304	276	162	210	214	0	27	111
40.00	660	659	686	316	287	167	223	232	0	28	114
45.03	686	685	710	328	298	172	236	248	0	28	118
49.98	712	710	733	339	307	176	249	263	-1	28	121
54.96	737	734	755	350	317	180	262	278	-1	29	124
60.01	761	759	778	360	327	184	275	294	-1	29	126
64.99	786	783	801	371	336	189	288	309	-2	29	129
69.98	809	806	823	381	345	193	301	324	-2	29	132
74.99	833	829	845	391	354	197	314	339	-2	29	134

Table A.11: Elastic constants of Al-endmember phase D as a function of pressure, in units of GPa, Part 2 of 2

P (GPa)	C_{23}	C_{24}	C_{25}	C_{26}	C_{34}	C_{35}	C_{36}	C_{45}	C_{46}	C_{56}
0.01	86	32	-4	-76	47	39	5	-48	5	10
5.00	106	30	-2	-82	46	38	6	-54	7	12
10.01	125	30	-2	-88	45	38	8	-59	9	12
15.01	143	30	-2	-93	46	38	9	-63	9	13
20.00	162	30	-2	-98	46	38	9	-68	9	13
24.99	180	30	-3	-102	44	37	11	-72	9	13
29.99	206	32	-3	-107	49	41	11	-76	9	13
35.00	221	32	-3	-110	48	40	11	-79	9	13
40.00	238	33	-3	-114	50	41	12	-83	9	13
45.03	254	33	-4	-117	50	42	12	-86	9	13
49.98	270	33	-4	-120	50	42	13	-88	9	13
54.96	285	33	-4	-123	51	42	13	-91	9	13
60.01	301	33	-4	-126	51	42	13	-94	10	14
64.99	316	33	-5	-129	51	43	14	-97	10	14
69.98	332	33	-5	-132	51	43	14	-99	10	14
74.99	347	34	-5	-134	52	43	14	-102	10	14

Table A.12: Elastic constants of phase D with 50% Al-substitution, in which the aluminum atoms were distributed randomly across eight unit cells, also known as configuration 88-1. Elastic constants are presented as as a function of pressure, in units of GPa. Part 1 of 2

P (GPa)	C_{11}	C_{22}	C_{33}	C_{44}	C_{55}	C_{66}	C_{12}	C_{13}	C_{14}	C_{15}	C_{16}
0.01	409	409	335	121	120	125	94	62	2	-1	-1
4.98	445	445	376	136	136	136	107	81	4	-2	0
10.03	479	479	415	150	150	143	121	101	5	-4	-1
14.97	511	511	451	163	163	152	134	119	6	-4	0
20.00	542	541	487	175	174	160	148	138	8	-5	0
25.02	571	571	522	186	186	167	161	156	8	-6	0
30.00	600	600	563	196	196	173	174	172	10	-7	0
34.98	627	627	602	206	206	179	188	191	11	-8	0
40.00	654	654	634	215	215	185	201	207	12	-9	0
44.98	680	680	645	224	224	191	214	223	12	-10	0
50.00	707	706	672	233	233	196	228	240	13	-10	0
54.97	732	732	698	241	241	201	241	256	14	-11	0
60.01	757	757	724	249	249	206	254	272	15	-12	0
64.97	781	781	749	257	257	211	267	287	16	-13	0
70.00	806	806	773	265	265	218	281	303	17	-13	0
74.97	829	829	797	273	273	222	294	319	17	-14	0

Table A.13: Elastic constants of phase D with 50% Al-substitution, in which the aluminum atoms were distributed randomly across eight unit cells, also known as configuration 88-1. Elastic constants are presented as as a function of pressure, in units of GPa. Part 2 of 2

P (GPa)	C_{23}	C_{24}	C_{25}	C_{26}	C_{34}	C_{35}	C_{36}	C_{45}	C_{46}	C_{56}
0.01	62	-2	2	-1	1	3	1	0	5	4
4.98	81	-2	4	0	4	4	0	0	2	6
10.03	101	-4	5	0	4	4	0	0	8	8
14.97	119	-4	6	0	5	5	0	0	9	9
20.00	138	-5	7	0	6	6	0	0	10	10
25.02	156	-6	9	0	5	6	-1	0	11	11
30.00	172	-7	10	0	6	6	0	0	12	12
34.98	191	-8	11	0	6	6	0	0	13	13
40.00	207	-9	12	0	6	6	0	0	13	13
44.98	223	-10	12	0	7	7	0	0	14	14
50.00	240	-10	13	0	7	7	0	0	15	15
54.97	256	-11	14	0	8	8	0	0	14	16
60.01	272	-12	15	0	8	8	0	0	16	16
64.97	287	-13	16	0	8	8	0	0	17	17
70.00	303	-13	17	0	8	8	0	0	17	17
74.97	319	-14	17	0	9	9	0	0	18	18

Table A.14: Elastic constants of phase D with 50% Al-substitution, in which the eight unit cells were individually end member composition, also known as configuration 88-2. Elastic constants are presented as as a function of pressure, in units of GPa. Part 1 of 2

P (GPa)	C_{11}	C_{22}	C_{33}	C_{44}	C_{55}	C_{66}	C_{12}	C_{13}	C_{14}	C_{15}	C_{16}
0.01	358	394	286	107	103	113	107	50	4	-6	0
5.02	409	433	336	122	123	126	117	79	5	-8	0
10.02	449	462	373	133	139	137	131	96	5	-11	0
15.04	485	499	424	148	153	146	143	119	7	-12	0
20.02	517	531	458	161	165	156	156	137	8	-11	0
25.03	548	559	495	176	177	162	168	157	10	-12	0
30.00	578	587	526	189	186	169	180	174	11	-12	0
34.98	607	618	556	196	196	175	193	191	12	-12	0
40.00	635	646	586	206	206	182	206	208	13	-12	0
44.98	662	672	615	216	215	188	218	224	13	-13	0
50.01	689	699	645	227	224	193	231	241	14	-13	0
54.98	713	725	681	234	232	199	244	255	16	-14	0
60.01	736	750	709	243	241	203	256	270	16	-14	0
64.98	764	775	735	251	249	208	270	287	17	-15	0
70.01	788	800	771	259	257	212	282	305	18	-15	0
74.97	812	823	782	267	264	217	295	319	18	-16	0

Table A.15: Elastic constants of phase D with 50% Al-substitution, in which the eight unit cells were individually end member composition, also known as configuration 88-2. Elastic constants are presented as as a function of pressure, in units of GPa. Part 2 of 2

P (GPa)	C_{23}	C_{24}	C_{25}	C_{26}	C_{34}	C_{35}	C_{36}	C_{45}	C_{46}	C_{56}
0.01	67	4	7	-1	16	1	5	0	6	9
5.02	85	1	8	-1	13	6	3	0	8	11
10.02	103	2	9	0	12	2	3	1	9	12
15.04	122	-1	11	0	13	3	3	0	11	13
20.02	139	-2	12	0	13	5	3	0	12	12
25.03	156	-6	12	0	7	7	2	0	14	14
30.00	172	-6	13	-1	8	7	2	-1	15	15
34.98	189	-6	13	0	10	7	2	0	15	15
40.00	205	-6	14	0	10	7	2	0	16	16
44.98	221	-9	15	0	8	7	2	0	17	17
50.00	238	-9	15	0	9	7	3	0	17	17
54.97	253	-8	16	0	11	7	3	0	18	18
60.01	269	-9	16	0	11	7	3	0	19	18
64.97	284	-10	17	0	12	7	3	0	19	19
70.00	303	-10	18	0	10	7	3	0	20	20
74.97	317	-11	18	0	12	7	3	0	21	21

Table A.16: Bulk (κ) and shear (μ) moduli of Mg-endmember phase D [$MgSi_2O_4(OH)_2$], Al-endmember [$Al_2SiO_4(OH)_2$], and tie-line composition in the 88-1 and 88-2 structures as a function of pressure from 0 to 75 GPa.

P (GPa)	Bulk modulus (κ)				Shear modulus (μ)			
	Mg-PhD	Al-PhD	88-1	88-2	Mg-PhD	Al-PhD	88-1	88-2
0	152.9	191.5	175.1	161.9	94.8	132.7	134.4	117.3
5	177.3	216.2	199.6	191.2	106.3	145.0	147.1	132.7
10	200.6	239.5	223.5	214.3	115.9	155.5	157.8	144.2
15	222.9	261.5	245.9	240.7	124.4	165.0	167.9	156.8
20	244.9	283.5	268.0	262.4	132.1	174.5	177.4	167.0
25	263.4	305.2	289.6	284.4	139.2	183.4	186.2	176.6
30	289.2	336.7	310.9	304.6	146.3	195.0	194.9	185.2
35	311.1	353.5	332.6	324.8	153.1	200.8	202.9	192.8
40	341.4	374.0	352.7	344.6	162.6	208.1	210.4	200.6
45	361.9	392.4	369.6	363.9	168.0	214.5	216.2	208.2
50	380.5	410.3	388.6	383.3	172.8	220.2	222.9	215.7
55	398.3	428.1	407.2	402.3	177.0	226.0	229.3	222.7
60	416.3	446.1	425.8	420.4	181.2	231.7	235.5	229.1
65	433.0	463.6	443.8	439.3	183.6	237.2	241.4	235.5
70	451.5	481.1	461.9	459.8	188.9	242.6	247.7	241.7
75	468.7	498.5	479.6	475.4	192.6	248.0	253.4	246.7

Table A.17: Compressional (V_P) and shear (V_S) velocities of Mg-endmember phase D [$MgSi_2O_4(OH)_2$], Al-endmember [$Al_2SiO_4(OH)_2$], and phase D with 50% Al-substitution [$AlMg_{0.5}Si_{1.5}O_4(OH)_2$] in both the 88-1 and 88-2 structures.

P (GPa)	Compressional Velocity (V_P)				Shear Velocity (V_S)			
	Mg-PhD	Al-PhD	88-1	88-2	Mg-PhD	Al-PhD	88-1	88-2
0	9.01	9.60	10.21	9.60	5.25	5.54	6.24	5.83
5	9.48	10.02	10.54	10.16	5.47	5.73	6.42	6.10
10	9.87	10.37	10.88	10.53	5.64	5.86	6.56	6.27
15	10.20	10.67	11.19	10.95	5.77	5.97	6.69	6.46
20	10.50	10.96	11.47	11.24	5.88	6.09	6.80	6.60
25	10.73	11.22	11.72	11.53	5.98	6.18	6.90	6.72
30	11.05	11.60	11.97	11.76	6.07	6.32	6.99	6.82
35	11.30	11.76	12.20	11.98	6.16	6.36	7.07	6.90
40	11.66	11.96	12.40	12.19	6.30	6.43	7.15	6.98
45	11.87	12.13	12.54	12.39	6.35	6.49	7.19	7.06
50	12.03	12.28	12.72	12.58	6.40	6.52	7.25	7.13
55	12.18	12.43	12.89	12.76	6.44	6.57	7.31	7.20
60	12.33	12.58	13.05	12.92	6.47	6.61	7.36	7.26
65	12.44	12.72	13.20	13.09	6.48	6.65	7.41	7.32
70	12.60	12.86	13.35	13.26	6.53	6.69	7.46	7.37
75	12.73	12.99	13.48	13.37	6.56	6.73	7.51	7.41

Table A.18: Maximum shear wave polarization anisotropy (AV_S) of Mg-endmember phase D [$MgSi_2O_4(OH)_2$], Al-endmember [$Al_2SiO_4(OH)_2$], phase D with 50% Al-substitution [$AlMg_{0.5}Si_{1.5}O_4(OH)_2$].

P (GPa)	Mg-PhD	Al-PhD	88-1	88-2
0	21.86	10.65	13.48	14.87
5	15.79	10.16	11.43	13.27
10	12.96	9.70	9.72	11.30
15	11.62	11.49	8.74	10.4
20	10.32	13.02	8.01	9.43
25	9.37	14.59	7.26	8.51
30	8.88	16.23	6.89	7.74
35	6.56	17.08	6.59	7.77
40	9.95	17.74	6.38	7.44
45	9.08	18.04	6.27	7.15
50	9.36	18.36	6.25	6.71
55	8.03	18.84	6.31	7.04
60	8.04	19.14	6.83	6.98
65	7.91	19.36	7.32	7.37
70	6.92	19.84	7.68	7.57
75	6.24	20.12	8.11	8.5

APPENDIX B

STABILITY AND ELASTICITY OF ϵ-FeOOH

Three Born stability equations relevant to the symmetry of ε-FeOOH:

$$B_{1,ii} = C_{ii} > 0 (i = 1, 2, 3, ..., 6) \tag{B.1}$$

$$B_{2,ii} = det \begin{vmatrix} C_{ii} & C_{ij} \\ C_{ji} & C_{jj} \end{vmatrix} > 0 (i, j = 1, 2, 3, i \neq j) \tag{B.2}$$

$$B_3 = det \begin{vmatrix} C_{11} & C_{12} & C_{13} \\ C_{21} & C_{22} & C_{23} \\ C_{31} & C_{32} & C_{33} \end{vmatrix} > 0 \tag{B.3}$$

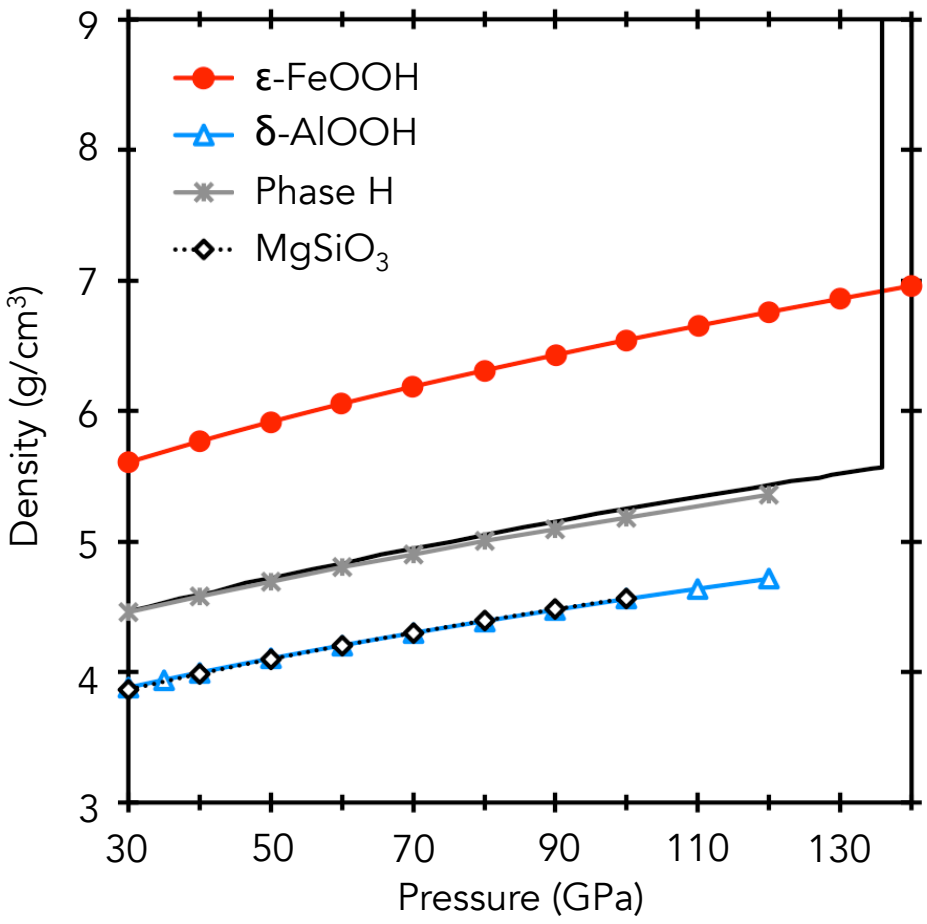

Figure B.1: Comparison of the density of the optimized structures of ε-FeOOH from this study (solid red circles), δ-AlOOH (Tsuchiya and Tsuchiya, 2009), phase H (Tsuchiya and Mookherjee, 2015), and $MgSiO_3$ bridgmanite (Wentzcovitch et al., 1996) as a function of pressure compared to the Preliminary Reference Earth Model (solid black line) (Dziewonski and Anderson, 1981). All values plotted are 0 K values excluding those of PREM.

.

Table B.1: Structural parameters of ε-FeOOH.

Pressure (GPa)	Unit cell vol. (Å^3)	FeO_6 vol. (Å^3)	$r_{O\cdots O}$ (Å)	$r_{O—H}$ (Å)	O—H···O (°)	a (Å)	b (Å)	c (Å)
0.01	59.88	10.18	2.44	1.35	179.37	4.83	4.24	2.91
4.98	58.19	9.92	2.41	1.29	179.55	4.79	4.22	2.88
10.00	56.76	9.69	2.38	1.19	179.99	4.75	4.18	2.86
15.00	55.64	9.50	2.37	1.19	179.99	4.72	4.16	2.84
20.01	54.35	9.25	2.37	1.18	180.00	4.67	4.08	2.85
30.01	52.64	8.96	2.35	1.18	180.00	4.63	4.04	2.82
40.00	51.17	8.71	2.34	1.17	180.00	4.59	4.00	2.79
49.99	49.88	8.49	2.32	1.16	180.00	4.55	3.98	2.76
59.97	48.73	8.30	2.31	1.16	180.00	4.52	3.95	2.73
69.98	47.70	8.12	2.30	1.15	180.00	4.50	3.93	2.70
80.03	46.76	7.97	2.29	1.14	179.99	4.47	3.91	2.68
90.00	45.90	7.83	2.28	1.14	179.99	4.45	3.89	2.65
100.00	45.10	7.70	2.27	1.13	179.99	4.44	3.87	2.63
110.03	44.36	7.58	2.26	1.13	179.98	4.42	3.86	2.60
120.01	43.67	7.46	2.25	1.12	179.98	4.40	3.85	2.58
130.01	43.02	7.36	2.24	1.12	179.98	4.39	3.83	2.56
139.99	42.40	7.26	2.23	1.12	179.99	4.38	3.82	2.53

Table B.2: Elastic constants of ε-FeOOH as a function of pressure from 30 to 140 GPa.

P (GPa)	C_{11}	C_{12}	C_{13}	C_{22}	C_{23}	C_{33}	C_{44}	C_{55}	C_{66}
30.01	528.3	258.8	230.4	487.6	269.3	446.9	127.3	104.7	220.8
40.00	581.4	301.5	268.5	529.2	310.3	480.5	126.3	107.2	238.7
49.99	629.8	343.6	305.7	569.1	349.9	512.5	124.6	109.3	255.4
59.97	676.2	386.9	342.7	607.4	385.8	542.5	120.0	110.3	271.4
69.98	719.2	429.4	379.5	643.3	421.7	571.4	114.5	110.7	287.5
80.03	765.0	471.5	414.4	682.0	458.0	597.8	109.6	110.8	301.3
90.01	808.6	512.9	448.6	717.6	491.6	624.6	101.1	109.5	314.9
99.90	852.5	555.4	481.8	754.4	524.6	652.1	93.8	109.0	329.0
110.03	896.7	599.7	516.5	792.1	558.5	681.0	90.4	109.1	343.1
120.01	944.1	641.6	549.4	829.5	591.6	711.7	81.4	107.9	356.8
130.01	982.7	682.8	579.7	867.0	623.8	742.2	71.7	106.0	370.6
139.99	1026.8	727.7	604.5	904.2	647.2	760.3	62.4	104.5	382.1

Table B.3: Geophysically relevant parameters of ε-FeOOH from 30 to 140 GPa, including density (ρ), bulk modulus (κ), shear modulus (μ), compressional velocity (V_P), and shear velocity (V_S).

P (GPa)	ρ (g/cm^3)	κ	μ	V_P	V_S
30.01	5.605	330.2	132.1	9.50	4.85
40.00	5.766	371.1	135.1	9.78	4.84
49.99	5.916	410.4	137.3	10.02	4.82
59.97	6.055	448.2	138.3	10.22	4.78
69.98	6.186	485.0	138.4	10.40	4.73
80.03	6.310	521.3	138.6	10.58	4.69
90.01	6.428	556.2	137.4	10.73	4.62
99.90	6.542	591.0	136.9	10.87	4.57
110.03	6.652	626.8	137.3	11.03	4.54
120.01	6.757	662.2	136.4	11.18	4.49
130.01	6.859	695.9	134.5	11.30	4.43
139.99	6.959	724.2	132.3	11.38	4.36

APPENDIX C

HIGH-PRESSURE EVOLUTION OF ϵ-FeOOH

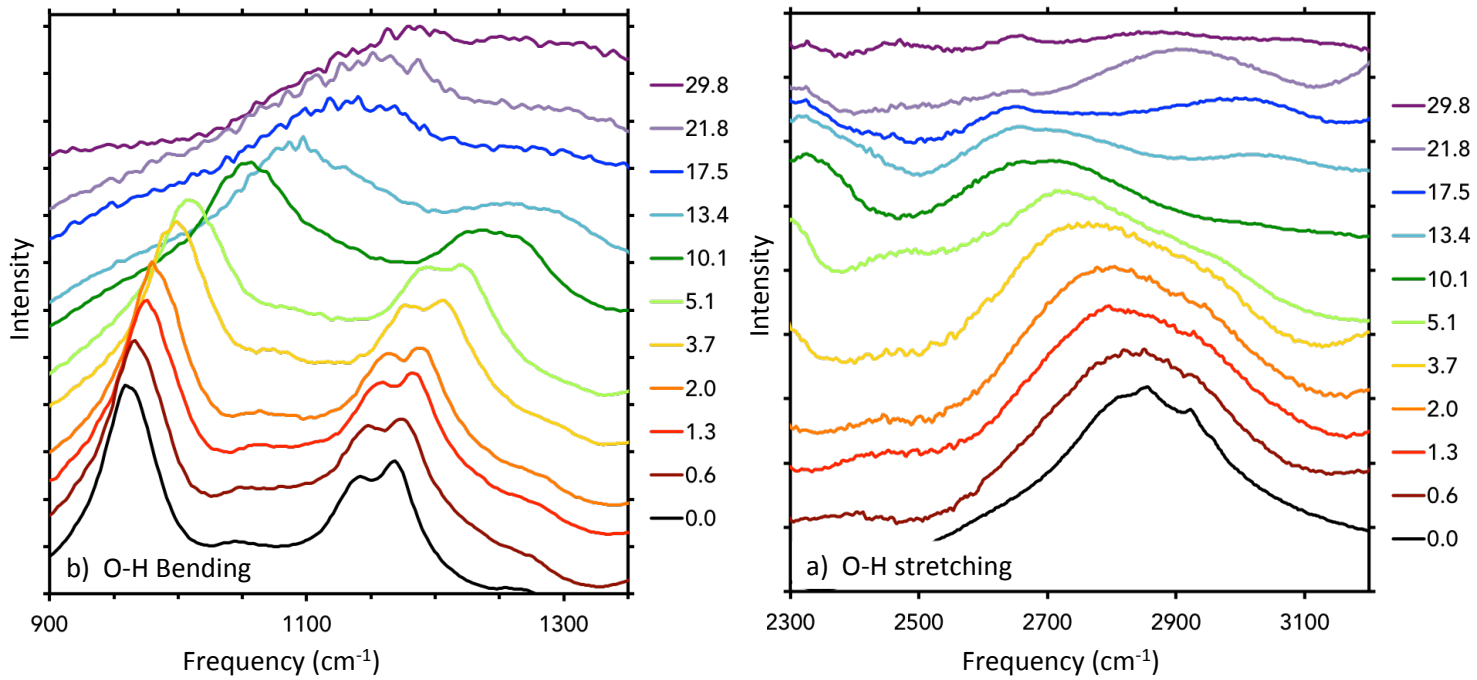

Figure C.1: Stacked high-pressure IR spectra of ε-FeOOH including (a) the O-H bending region and (b) the O-H stretching region.

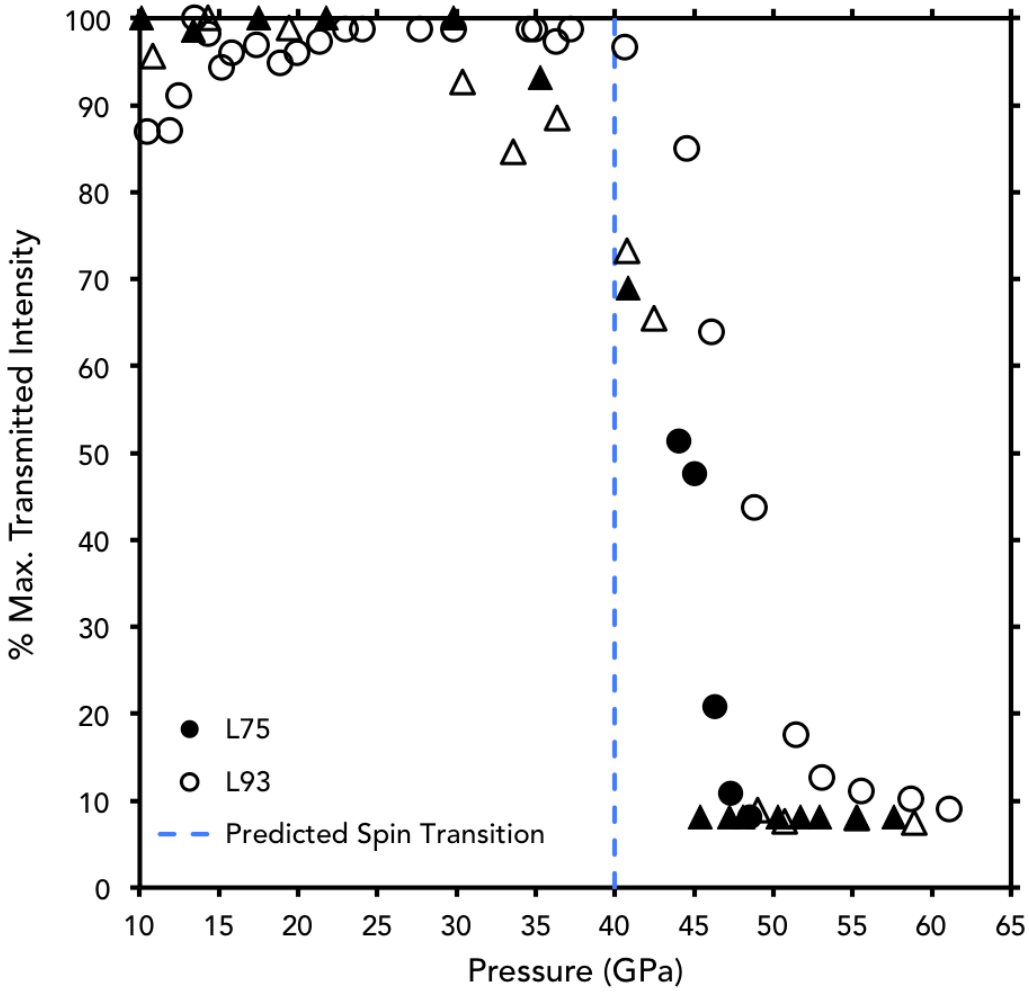

Figure C.2: Pressure-induced reduction of IR signal in ε-FeOOH.

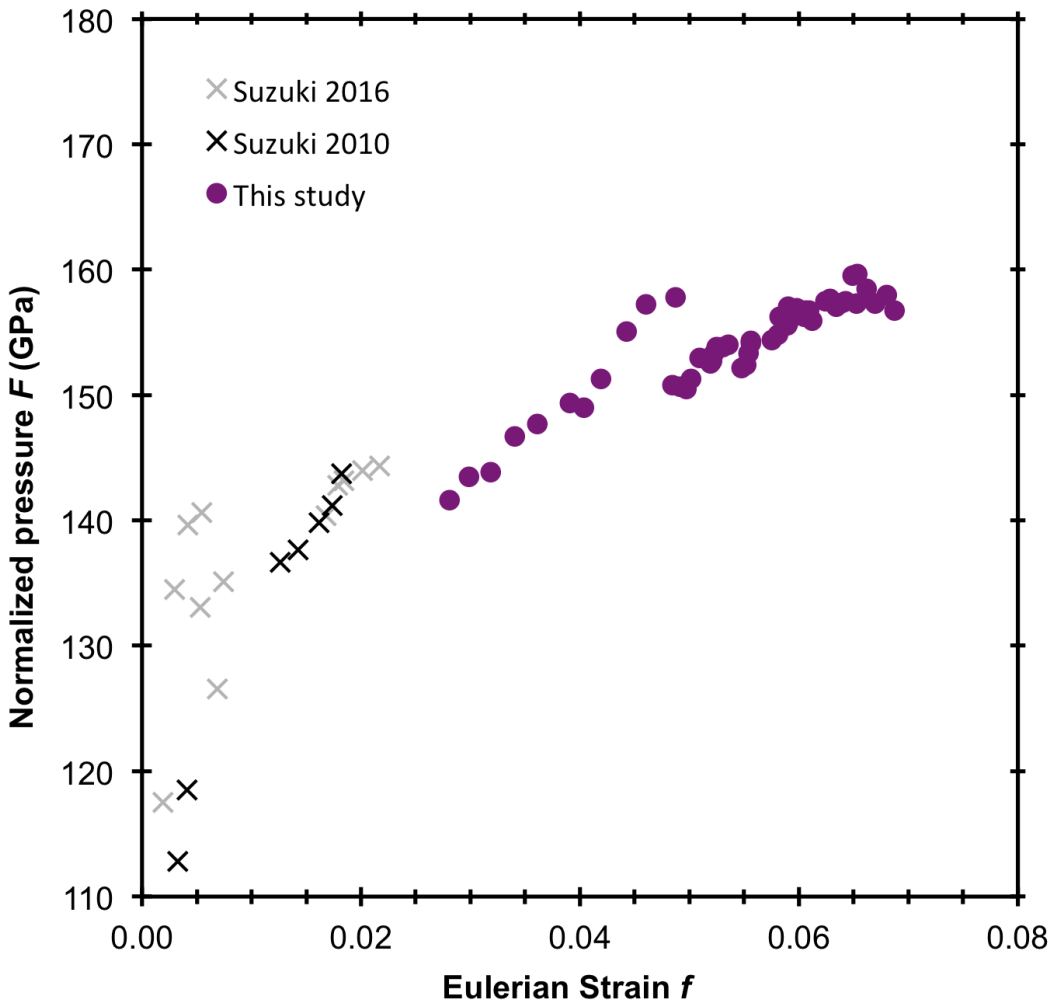

Figure C.3: Eulerian strain (f) versus the normalized pressure (F_E) of ε-FeOOH, including data from this study (filled purple circle symbols), data from Suzuki (2010) (grey X symbols), and data from Suzuki (2016) (black X symbols). This fit utilizes a V_0 of 66.278 Å^3 in agreement with Suzuki (2016) and the EoS fitting for this study also.

Table C.1: Raw optical absorption data for sample L96.

P (GPa)	1.45 nm	1.55 nm	1.65 nm	1.75 nm	1.85 nm	1.95 nm	2.05 nm
0.60(2)	0.310	0.299	0.277	0.204	0.164	0.140	0.102
2.60(8)	0.364	0.338	0.315	0.242	0.193	0.161	0.121
3.0(1)	0.387	0.373	0.339	0.254	0.211	0.172	0.131
3.7(1)	0.262	0.233	0.212	0.148	0.116	0.091	0.069
4.6(1)	0.215	0.201	0.181	0.131	0.103	0.088	0.060
5.9(2)	0.284	0.273	0.258	0.202	0.178	0.144	0.097
6.7(2)	0.222	0.211	0.199	0.154	0.126	0.104	0.065
8.2(2)	0.292	0.274	0.254	0.194	0.158	0.121	0.070
9.0(3)	0.353	0.322	0.294	0.217	0.173	0.124	0.061
9.8(3)	0.347	0.325	0.300	0.226	0.183	0.136	0.070
10.5(3)	0.180	0.168	0.154	0.120	0.096	0.066	0.033
11.7(4)	0.197	0.184	0.168	0.129	0.102	0.066	0.029
12.8(4)	0.172	0.158	0.144	0.109	0.084	0.050	0.021
14.3(4)	0.374	0.335	0.295	0.208	0.151	0.080	0.024
15.0(5)	0.231	0.200	0.181	0.129	0.090	0.046	0.021
17.8(5)	0.161	0.144	0.128	0.087	0.055	0.025	0.007
19.6(6)	0.165	0.148	0.130	0.082	0.045	0.016	0.004
20.5(6)	0.160	0.137	0.121	0.074	0.039	0.016	0.005
21.9(7)	0.175	0.151	0.134	0.085	0.050	0.026	0.013
23.4(7)	0.166	0.143	0.127	0.078	0.049	0.028	0.016
26.4(8)	0.110	0.093	0.082	0.049	0.032	0.020	0.012
28.1(8)	0.102	0.083	0.071	0.040	0.026	0.016	0.011
31.0(9)	0.081	0.064	0.053	0.028	0.017	0.011	0.006
33.8(10)	0.068	0.050	0.041	0.022	0.014	0.008	0.005
35.5(11)	0.108	0.075	0.061	0.032	0.020	0.012	0.005
36.6(11)	0.058	0.041	0.032	0.017	0.011	0.006	0.003
38.8(12)	0.039	0.027	0.022	0.013	0.008	0.005	0.003
41.2(12)	0.020	0.015	0.012	0.007	0.004	0.003	0.002
45.3(16)	0.006	0.004	0.004	0.003	0.003	0.002	0.002
45.3(14)	0.004	0.003	0.003	0.003	0.003	0.002	0.002
50.3(15)	0.002	0.002	0.001	0.001	0.001	0.001	0.001
50.6(15)	0.003	0.002	0.002	0.002	0.001	0.001	0.001
55.0(17)	0.004	0.003	0.002	0.002	0.002	0.001	0.001
58.6(18)	0.002	0.002	0.002	0.001	0.001	0.001	0.001
60.7(18)	0.005	0.004	0.004	0.004	0.003	0.003	0.003
63.4(19)	0.003	0.002	0.002	0.002	0.001	0.001	0.000
66.5(20)	0.003	0.002	0.002	0.002	0.002	0.002	0.001
71.6(21)	0.003	0.002	0.002	0.001	0.001	0.001	0.001

Table C.2: Raw optical absorption data for sample L97.

P (GPa)	1.45 nm	1.55 nm	1.65 nm	1.75 nm	1.85 nm	1.95 nm	2.05 nm
0.80(2)	0.299	0.259	0.208	0.154	0.117	0.085	0.095
1.20(4)	0.381	0.329	0.264	0.199	0.151	0.113	0.039
2.30(7)	0.368	0.328	0.273	0.212	0.176	0.132	0.073
2.70(8)	0.342	0.324	0.284	0.248	0.211	0.182	0.091
5.5(2)	0.458	0.392	0.322	0.258	0.207	0.154	0.073
6.8(2)	0.333	0.306	0.259	0.209	0.168	0.127	0.071
8.4(3)	0.396	0.342	0.283	0.222	0.180	0.143	0.079
9.5(3)	0.378	0.328	0.270	0.213	0.174	0.127	0.067
10.9(3)	0.396	0.330	0.261	0.205	0.158	0.114	0.061
11.6(4)	0.371	0.319	0.254	0.195	0.148	0.093	0.018
13.6(4)	0.369	0.321	0.259	0.200	0.148	0.087	0.060
14.5(4)	0.404	0.334	0.261	0.188	0.134	0.066	0.049
15.8(5)	0.399	0.330	0.260	0.201	0.143	0.077	0.041
16.2(5)	0.429	0.363	0.297	0.234	0.164	0.088	0.084
17.1(5)	0.387	0.331	0.274	0.212	0.152	0.092	0.079
19.6(6)	0.421	0.355	0.295	0.224	0.153	0.092	0.061
20.9(6)	0.408	0.340	0.277	0.206	0.136	0.083	0.025
22.1(7)	0.314	0.268	0.220	0.162	0.108	0.064	0.016
23.7(7)	0.350	0.307	0.252	0.188	0.127	0.078	0.074
24.8(7)	0.338	0.286	0.233	0.165	0.109	0.066	0.053
26.5(8)	0.328	0.279	0.222	0.162	0.106	0.066	0.014
28.2(9)	0.283	0.232	0.183	0.131	0.088	0.054	0.024
30.2(9)	0.275	0.222	0.168	0.117	0.077	0.047	0.047
31.9(10)	0.276	0.211	0.157	0.104	0.067	0.039	0.037
33.3(10)	0.252	0.188	0.138	0.094	0.061	0.033	0.061

Table C.3: Raw optical absorption data for sample L98.

P (GPa)	1.45 nm	1.55 nm	1.65 nm	1.75 nm	1.85 nm	1.95 nm	2.05 nm
2.30(7)	0.706	0.668	0.605	0.535	0.470	0.415	0.350
3.10(9)	0.537	0.505	0.461	0.398	0.357	0.308	0.251
4.8(1)	0.615	0.591	0.543	0.481	0.422	0.375	0.299
6.5(2)	0.733	0.706	0.648	0.580	0.522	0.452	0.348
9.3(3)	0.666	0.639	0.578	0.529	0.456	0.375	0.262
10.3(3)	0.586	0.546	0.488	0.440	0.372	0.298	0.194
11.4(3)	0.691	0.642	0.579	0.516	0.446	0.352	0.224
13.0(4)	0.699	0.653	0.587	0.521	0.441	0.337	0.207
14.8(4)	0.837	0.795	0.748	0.698	0.610	0.493	0.370

Table C.4: Raw optical absorption data for sample L100.

P (GPa)	1.45 nm	1.55 nm	1.65 nm	1.75 nm	1.85 nm	1.95 nm	2.05 nm
0.50(2)	0.086	0.063	0.045	0.027	0.017	0.014	0.012
1.30(4)	0.094	0.071	0.049	0.031	0.015	0.008	0.005
2.50(8)	0.118	0.091	0.063	0.037	0.023	0.015	0.009
6.6(2)	0.105	0.076	0.050	0.033	0.023	0.014	0.006
10.1(3)	0.106	0.079	0.056	0.036	0.022	0.011	0.005
11.6(4)	0.096	0.075	0.056	0.039	0.025	0.015	0.012
14.2(4)	0.086	0.063	0.042	0.023	0.010	0.002	0.000
17.8(5)	0.085	0.064	0.044	0.026	0.013	0.006	0.005
20.7(6)	0.117	0.096	0.073	0.052	0.034	0.023	0.017
23.6(7)	0.079	0.058	0.041	0.024	0.012	0.006	0.004
26.1(8)	0.126	0.089	0.058	0.031	0.015	0.006	0.002
29.7(9)	0.096	0.067	0.042	0.022	0.012	0.006	0.003
32.9(10)	0.084	0.053	0.030	0.016	0.008	0.003	0.001
37.3(11)	0.046	0.026	0.015	0.008	0.004	0.002	0.001
49.6(15)	0.001	0.002	0.002	0.002	0.001	0.001	0.001
54.6(16)	0.001	0.001	0.001	0.001	0.001	0.001	0.001
68.7(21)	0.002	0.001	0.001	0.001	0.001	0.001	0.001

Table C.5: Raw optical absorption data for sample L101.

P (GPa)	1.45 nm	1.55 nm	1.65 nm	1.75 nm	1.85 nm	1.95 nm	2.05 nm
1.60(5)	0.320	0.284	0.231	0.191	0.147	0.112	0.081
2.50(8)	0.243	0.198	0.155	0.124	0.097	0.074	0.056
4.4(1)	0.268	0.233	0.202	0.169	0.141	0.114	0.089
5.9(2)	0.317	0.259	0.207	0.176	0.145	0.115	0.089
9.0(3)	0.262	0.225	0.187	0.163	0.135	0.104	0.072
10.0(3)	0.310	0.263	0.218	0.182	0.150	0.110	0.072
11.5(4)	0.260	0.224	0.183	0.154	0.123	0.091	0.059
13.1(4)	0.237	0.192	0.155	0.120	0.092	0.060	0.034
15.0(5)	0.220	0.183	0.147	0.116	0.084	0.050	0.024
17.1(5)	0.240	0.197	0.164	0.134	0.106	0.076	0.051
18.1(5)	0.223	0.183	0.140	0.106	0.072	0.040	0.020
19.2(6)	0.284	0.217	0.168	0.129	0.090	0.056	0.037
21.9(7)	0.227	0.193	0.159	0.130	0.097	0.064	0.044
23.2(7)	0.224	0.178	0.135	0.103	0.067	0.039	0.026
27.3(8)	0.178	0.135	0.099	0.066	0.042	0.025	0.016
29.9(9)	0.264	0.218	0.174	0.132	0.096	0.067	0.044
31.9(10)	0.216	0.166	0.121	0.080	0.053	0.035	0.023
33.9(10)	0.226	0.164	0.114	0.071	0.044	0.026	0.013
37.3(11)	0.182	0.133	0.089	0.052	0.029	0.012	0.002
41.5(13)	0.138	0.100	0.071	0.047	0.030	0.016	0.008
44.0(13)	0.160	0.118	0.086	0.058	0.035	0.018	0.008
45.7(14)	0.039	0.028	0.019	0.013	0.009	0.005	0.003
49.2(15)	0.004	0.004	0.003	0.003	0.002	0.002	0.002
51.2(15)	0.001	0.001	0.001	0.001	0.000	0.000	0.000

Table C.6: Lattice parameters and unit cell volumes of ε-FeOOH based on XRD measurements, 1 of 2. Values in parentheses reflect uncertainties.

P (GPa)	a (A)	b (A)	c (A)	V (A3)
13.7(1)	4.839(5)	4.311(5)	2.927(3)	61.06(11)
14.9(2)	4.832(5)	4.302(5)	2.922(3)	60.75(11)
16.0(2)	4.824(6)	4.293(6)	2.918(3)	60.42(13)
17.7(2)	4.815(6)	4.283(6)	2.911(3)	60.04(13)
19.0(1)	4.810(7)	4.274(7)	2.903(8)	59.70(21)
21.1(4)	4.798(6)	4.263(6)	2.895(3)	59.21(13)
21.9(5)	4.791(6)	4.257(7)	2.893(3)	59.00(14)
23.3(6)	4.783(6)	4.254(7)	2.887(3)	58.73(13)
25.5(8)	4.778(6)	4.244(7)	2.878(3)	58.36(14)
27.1(5)	4.770(5)	4.238(6)	2.873(3)	58.08(12)
27.6(7)	4.763(4)	4.226(7)	2.866(2)	57.69(12)
28.1(3)	4.752(5)	4.232(6)	2.864(2)	57.59(11)
28.4(2)	4.753(4)	4.227(4)	2.862(2)	57.50(8)
28.9(2)	4.752(4)	4.226(4)	2.860(2)	57.43(8)
29.1(8)	4.757(6)	4.229(6)	2.866(2)	57.65(12)
29.8(3)	4.751(4)	4.222(5)	2.857(2)	57.31(9)
30.4(3)	4.742(3)	4.221(4)	2.855(1)	57.15(7)
30.6(3)	4.743(3)	4.220(4)	2.854(1)	57.13(7)
30.8(3)	4.744(3)	4.221(4)	2.852(1)	57.11(7)
31.1(3)	4.740(4)	4.218(5)	2.854(2)	57.06(9)
31.5(3)	4.740(6)	4.214(6)	2.852(1)	56.97(9)
31.9(3)	4.740(6)	4.214(6)	2.849(1)	56.90(12)
32.0(9)	4.749(6)	4.216(7)	2.856(2)	57.19(13)
32.4(3)	4.732(3)	4.212(3)	2.844(1)	56.71(6)
32.8(4)	4.730(3)	4.211(3)	2.841(1)	56.65(5)
33.1(3)	4.732(3)	4.212(3)	2.843(1)	56.62(5)
33.5(3)	4.728(3)	4.209(3)	2.842(1)	56.58(6)

Table C.7: Lattice parameters and unit cell volumes of ε-FeOOH based on XRD measurements, 2 of 2. Values in parentheses reflect uncertainties.

P (GPa)	a (A)	b (A)	c (A)	V (A3)
33.5(3)	4.729(3)	4.210(3)	2.842(1)	56.58(6)
35.0(4)	4.721(3)	4.203(3)	2.837(1)	56.29(6)
35.5(4)	4.720(3)	4.201(3)	2.834(1)	56.20(6)
35.9(4)	4.720(3)	4.200(4)	2.834(1)	56.18(7)
36.2(4)	4.718(3)	4.200(3)	2.834(1)	56.13(5)
36.3(4)	4.715(2)	4.199(3)	2.832(1)	56.08(5)
36.5(4)	4.717(2)	4.198(3)	2.830(1)	56.05(5)
36.8(2)	4.717(3)	4.198(3)	2.831(1)	56.06(6)
37.0(4)	4.714(3)	4.197(3)	2.831(1)	56.00(5)
37.2(3)	4.715(3)	4.195(3)	2.829(1)	55.95(5)
37.3(4)	4.716(3)	4.195(4)	2.828(1)	55.95(7)
37.7(5)	4.709(3)	4.195(3)	2.827(1)	55.84(5)
37.9(5)	4.711(3)	4.192(3)	2.827(1)	55.83(6)
38.2(5)	4.710(3)	4.189(3)	2.827(1)	55.77(6)
38.2(5)	4.710(4)	4.187(4)	2.826(1)	55.74(7)
39.6(6)	4.704(2)	4.184(2)	2.823(1)	55.55(4)
40.0(5)	4.701(2)	4.184(2)	2.821(1)	55.49(4)
40.3(6)	4.669(2)	4.183(2)	2.819(1)	55.41(4)
40.8(8)	4.667(2)	4.180(2)	2.818(1)	55.32(4)
41.1(6)	4.668(1)	4.179(2)	2.815(1)	55.28(3)
41.8(5)	4.697(4)	4.175(5)	2.812(2)	55.14(9)
42.2(6)	4.693(5)	4.177(6)	2.815(2)	55.19(11)
42.5(3)	4.692(8)	4.178(9)	2.812(3)	55.13(17)
42.9(3)	4.692(2)	4.175(2)	2.808(1)	55.01(4)
43.3(8)	4.690(1)	4.168(1)	2.807(1)	54.89(3)
43.3(7)	4.687(2)	4.166(2)	2.803(1)	54.74(5)
44.6(7)	4.685(2)	4.160(2)	2.803(1)	54.64(4)

APPENDIX D

STABILITY AND PROPERTIES OF PYRITE-TYPE $(Fe,Al)O_2H$

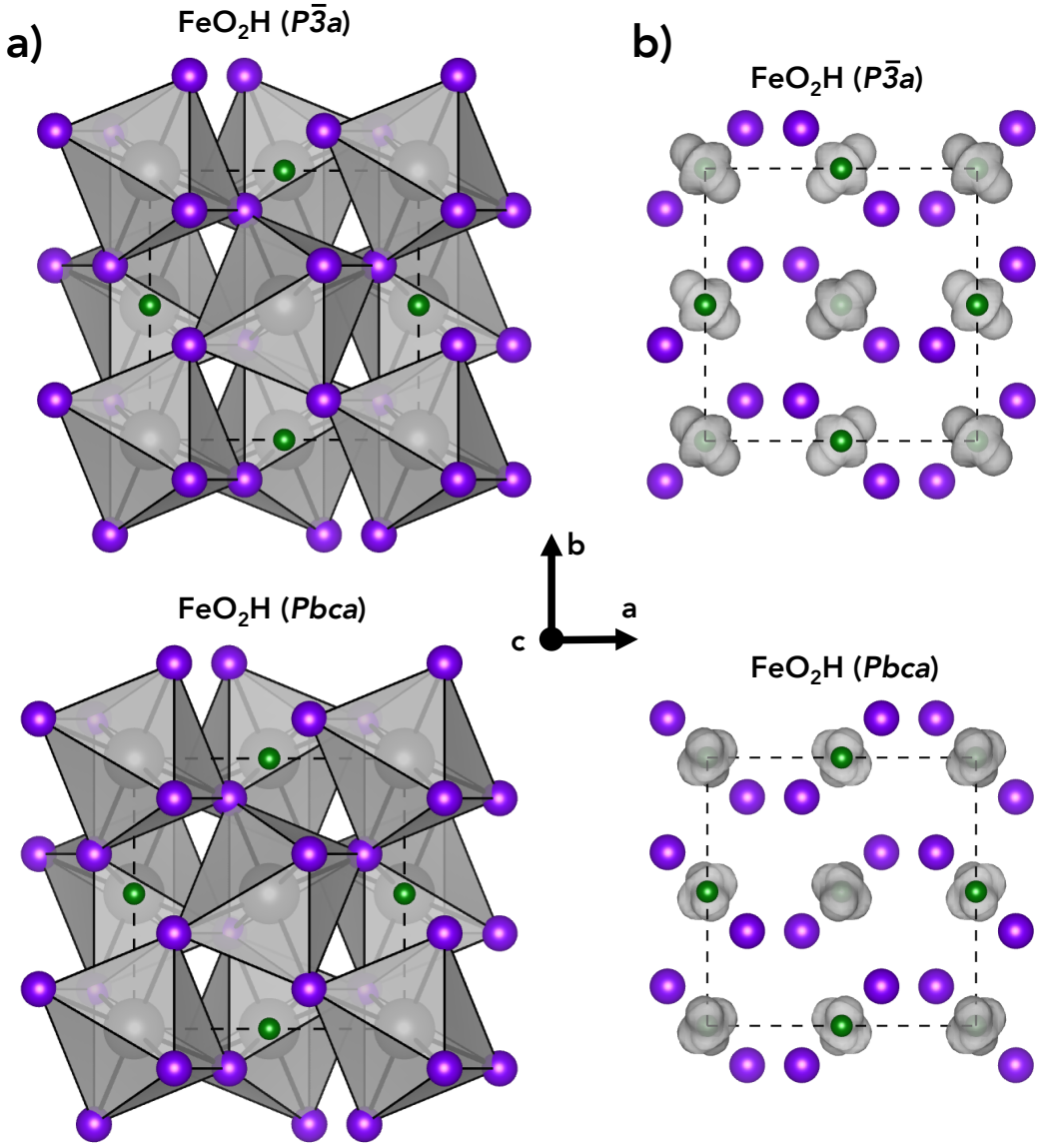

Figure D.1: Spin polarization density maps of FeO_2H at 70 GPa, including (a) crystal structures of the cubic ($Pa\bar{3}$) (top) and orthorhombic ($Pbca$) (bottom) crystal structures with grey FeO_6 polyhedra, and (b) the same crystal structures with iron atoms removed and grey isosurfaces indicating a value of 0.080 $e^-/a.u.^3$ on the right. Large grey spheres are Fe atoms, medium purple spheres are oxygen atoms, and small green spheres are H atoms. Images were generated in VESTA (Momma and Izumi, 2008).

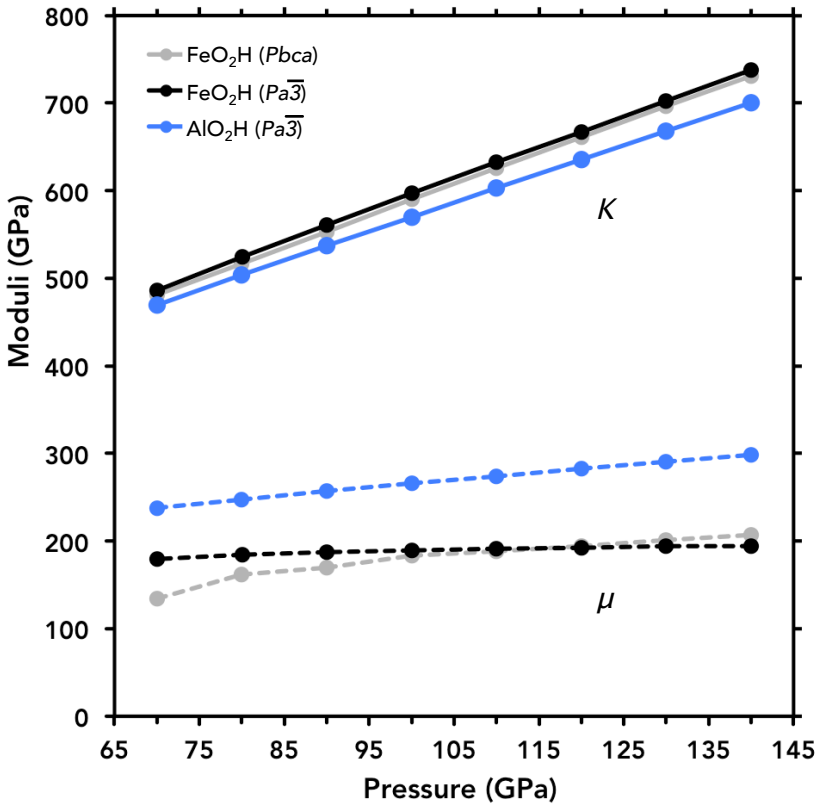

Figure D.2: Bulk (solid lines) and shear (dashed lines) moduli (b) of orthorhombic (*Pbca*) FeO_2H (grey symbols), cubic ($Pa\bar{3}$) FeO_2H (black symbols), and cubic ($Pa\bar{3}$) AlO_2H (blue symbols) as a function of pressure from 70 to 150 GPa. All values plotted are 0 K values excluding those of PREM.

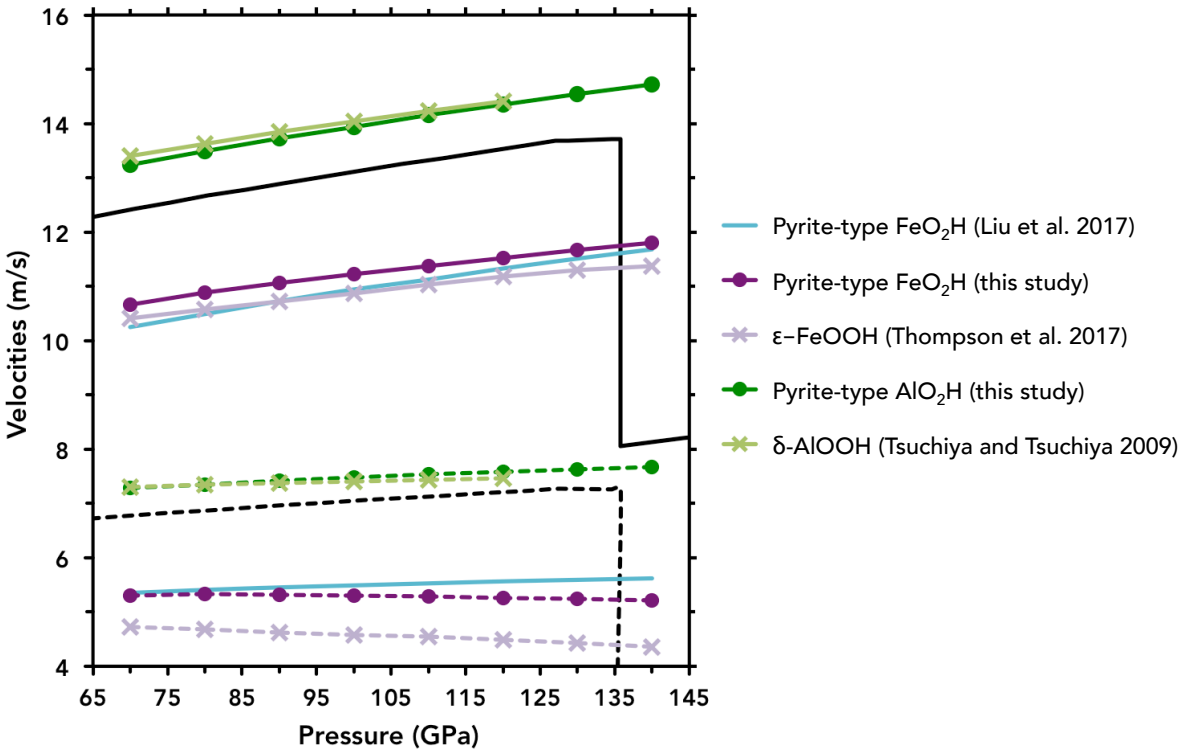

Figure D.3: Sound velocities of pyrite-type FeO_2H from Liu et al. (2017) (aqua) and this study (dark purple), $CaCl_2$-type ε-FeOOH from Thompson et al. (2017) (light purple), pyrite-type AlO_2H from this study (dark green), $CaCl_2$-type δ-AlOOH from Tsuchiya and Tsuchiya (2009) (light green), and the Preliminary Reference Earth Model (PREM) (Dziewonski and Anderson, 1981) (black). Compressional Velocities (V_P) are indicated by solid lines and shear velocities (V_S) are indicated by dashed lines. All data reflects 0K calculations with the exception of PREM, and the velocities of Liu et al. (2017), which reflect 300K calculations.

Table D.1: Lattice parameters (a, b, c) and unit cell volumes in pyrite-type FeO_2H and AlO_2H from 70 to 140 GPa.

P	*Pbca* FeO_2H				*Pa*$\bar{3}$ FeO_2H		*Pa*$\bar{3}$ AlO_2H	
(GPa)	a (Å)	b (Å)	c (Å)	V (Å^3)	a (Å)	V (Å^3)	a (Å)	V (Å^3)
70	4.537	4.549	4.530	92.20	4.522	92.46	4.461	88.78
80	4.505	4.489	4.499	90.38	4.493	90.66	4.431	86.98
90	4.476	4.462	4.469	88.71	4.465	89.01	4.402	85.32
100	4.448	4.438	4.441	87.19	4.440	87.49	4.376	83.79
110	4.422	4.415	4.417	85.77	4.416	86.08	4.351	82.38
120	4.399	4.392	4.393	84.46	4.393	84.77	4.328	81.05
130	4.376	4.372	4.350	83.23	4.372	83.55	4.306	79.82
140	4.355	4.352	4.331	82.08	4.351	82.40	4.285	78.66

Table D.2: Distortion index of FeO_6 octahedral units in *Pbca* and $Pa\bar{3}$ pyrite-type FeO_2H. Formula for distortion index from Baur (1974) and values calculated in VESTA (Momma and Izumi, 2008).

P (GPa)	*Pbca*	$Pa\bar{3}$
60	—	0.00001
70	0.00124	0.00000
80	0.00298	0.00001
90	0.00107	0.00001
100	0.00097	0.00001
110	0.00108	0.00001
120	0.00122	0.00002
130	0.00140	0.00002
140	0.00155	0.00002

Table D.3: Equation of state parameters for FeO_6 and AlO_6 octahedra in pyrite-type FeO_2H and AlO_2H respectively. Values in parentheses are uncertainties on the last digit.

Phase	V_0	K_0	K_0'
FeO_6 (*Pbca*)	10.155(6)	218.9(7)	4 (fixed)
FeO_6 (*Pbca*)	10.25(2)	202(3)	4.20(4)
FeO_6 ($Pa\bar{3}$)	10.167(5)	220.5(6)	4 (fixed)
FeO_6 ($Pa\bar{3}$)	10.25(1)	205(2)	4.19(3)
AlO_6 ($Pa\bar{3}$)	9.912(3)	195.8(3)	4 (fixed)
AlO_6 ($Pa\bar{3}$)	9.872(6)	203(1)	3.92(1)

Table D.4: Elastic constants of cubic pyrite-type FeO_2H and AlO_2H from 60 to 140 GPa.

P (GPa)	AlO_2H			FeO_2H		
	C_{11}	C_{12}	C_{44}	C_{11}	C_{12}	C_{44}
60	804.9	250.1	201.3	700.4	323.3	165.0
70	857.2	469.5	208.0	741.4	358.1	171.8
80	907.0	503.8	216.5	785.4	394.5	177.8
90	956.1	536.9	224.3	822.6	430.0	181.7
100	1003.9	569.7	231.9	858.9	466.5	185.1
110	1051.0	602.9	239.4	893.6	502.3	188.4
120	1097.3	635.4	246.7	926.6	537.9	191.4
130	1141.3	668.4	253.9	962.7	573.0	194.2
140	1185.9	700.6	261.0	992.2	610.2	196.8

Table D.5: Elastic constants of orthorhombic (*Pbca*) FeO_2H from 70 to 140 GPa.

P (GPa)	C11	C12	C13	C22	C23	C33	C44	C55	C66
70	708.8	364.8	344.0	739.9	368.8	727.5	175.8	80.3	92.5
80	750.2	390.8	384.6	796.1	388.1	782.5	184.6	123.0	128.5
90	790.4	423.5	421.3	836.6	418.5	823.3	192.2	127.6	148.8
100	831.1	461.1	456.5	879.1	448.2	873.5	203.8	150.3	164.7
110	865.2	495.6	491.7	917.6	480.5	917.7	210.5	159.3	168.5
120	898.6	530.9	526.4	955.6	513.3	959.8	216.7	163.3	180.9
130	929.8	566.4	560.5	992.8	546.5	1001.3	222.6	177.5	191.6
140	962.6	601.4	594.3	1029.6	579.9	1041.1	228.0	190.4	200.9

APPENDIX E

GEOPHYSICAL PROPERTIES OF *fcc* IRON HYDRIDE

Table E.1: Pre-synthesis details of FeH_X samples including pre-heating pressure, primary pressure standard, percent isotopic enrichment, gasket material, and *hcp* iron unit-cell volume. In some instances pre-synthesis pressures or *hcp* iron unit volumes are unavailable, in which case they are denoted as 'unknown'.

Pre-synthesis P (GPa)	Pressure standard	% ^{57}Fe	Gasket material	*hcp* Fe V (Å^3)
19.3(1)	ruby	95	Be/CBN	unknown
19.3(1)	ruby	0	Re	20.47(1)
22.6(1)	MgO	0	Re	20.22(1)
24.4(2)	ruby	0	Re	unknown
25.7(1)	ruby	0	Re	20.00(1)
27.0(1)	MgO	0	Re	19.91(1)
unknown	ruby	95	Be/CBN	unknown
30.6(1)	MgO	0	Re	19.67(1)
30.9(1)	ruby	0	Re	19.65(1)
32.1(1)	MgO	0	Re	19.57(1)
33.6(1)	ruby	0	Re	19.48(1)
40.0(2)	ruby	20	Be/CBN	unknown
40.4(1)	ruby	0	Re	19.09(1)
unknown	ruby	95	Be/CBN	unknown
41.8(1)	ruby	0	Re	19.01(1)
42.7(1)	ruby	0	Re	18.96(1)
44.0(1)	ruby	0	Re	18.90(1)
47.8(1)	ruby	0	Re	18.70(1)
48.4(1)	MgO	0	Re	18.67(1)
49.2(1)	ruby	0	Re	18.63(1)
50.5(2)	ruby	0	Re	18.57(1)
50.7(2)	ruby	0	Re	18.57(1)
53.1(2)	MgO	0	Re	18.45(1)
55.3(2)	MgO	0	Re	18.35(1)
55.6(2)	ruby	0	Re	18.34(1)
60.0(2)	MgO	0	Re	18.15(1)
60.3(3)	ruby	0	Re	18.14(1)
60.5(3)	ruby	0	Re	18.13(1)
60.6(3)	ruby	0	Re	18.13(1)
62.2(3)	ruby	0	Re	18.07(1)
65(1)	ruby	95	Be/CBN	unknown
66.2(3)	ruby	0	Re	17.91(1)
68.4(3)	ruby	0	Re	17.81(1)
unknown	ruby	95	Be/CBN	unknown

Table E.2: Details of FeH_X sample including pre-heating pressure, peak temperature, and total duration of laser heating. Samples primarily laser heated at the University of Chicago are denoted with a (*) symbol. Values in parentheses reflect uncertainties. In some instances pre-synthesis pressures or *hcp* iron unit volumes are unavailable, in which case they are denoted as 'unknown'.

Pre-synthesis P (GPa)	Peak synthesis T (K)	Heating duration (mins)
19.3(1)	*1800(400)	8
19.3(1)	1810(101)	3
22.6(1)	2070(103)	20
24.4(2)	*1800(400)	10
25.7(1)	1550(106)	15
27.0(1)	2004(100)	21
unknown	*1800(400)	8
30.6(1)	2000(101)	16
30.9(1)	1500(100)	4
32.1(1)	1730(146)	13
33.6(1)	1700(103)	16
40.0(2)	*1800(400)	10
40.4(1)	1540(101)	4
unknown	*1800(400)	8
41.8(1)	1570(105)	6
42.7(1)	1500(100)	4
44.0(1)	1650(124)	2
47.8(1)	1590(100)	3
48.4(1)	1890(138)	18
49.2(1)	1590(108)	3
50.5(2)	1520(101)	3
50.7(2)	1520(109)	3
53.1(2)	1860(111)	18
55.3(2)	1948(103)	28
55.6(2)	1590(108)	4
60.0(2)	1660(101)	7
60.3(3)	1560(101)	2
60.5(3)	1740(140)	3
60.6(3)	1570(100)	4
62.2(3)	1750(124)	4
65(1)	*1880(100)	9
66.2(3)	1560(100)	3
68.4(3)	1700(121)	3
unknown	*1800(400)	9

Table E.3: Details of FeH_X sample including pre-heating pressure, quench pressure (300 K), lattice parameter of the resultant *fcc* FeH_X, and observed quenched phases. Values in parentheses reflect uncertainties in final digit. In some instances pre-synthesis pressures or *hcp* iron unit volumes are unavailable, in which case they are denoted as 'unknown'.

Pre-synthesis P (GPa)	Post-synthesis P (GPa)	*fcc* Fe *a* (Å)	Quenched phases
19.3(1)	18.4(2)	3.607(2)	Iron hydride
19.3(1)	18.7(3)	3.691(9)	Iron hydride, diamond
22.6(1)	22.3(1)	3.666(1)	Iron hydride, MgO
24.4(2)	24.0(3)	3.602 (1)	Iron hydride
25.7(1)	25.0(4)	3.673(3)	Iron hydride, diamond
27.0(1)	26.4(1)	3.651(6)	Iron hydride, MgO
unknown	29.0(4)	3.628(1)	Iron hydride
30.6(1)	29.8(2)	3.628(1)	Iron hydride, MgO
30.9(1)	30.4(5)	3.579(3)	Iron hydride, diamond
32.1(1)	31.2(2)	3.580(2)	Iron hydride, MgO
33.6(1)	33.1(5)	3.618 (1)	Iron hydride, diamond
40.0(2)	39.5(6)	3.577(2)	Iron hydride
40.4(1)	40.1(6)	3.587(7)	Iron hydride, diamond
unknown	41.0(6)	3.577(2)	Iron hydride
41.8(1)	41.5(6)	3.613 (1)	Iron hydride, diamond
42.7(1)	41.9(6)	3.602(3)	Iron hydride, diamond
44.0(1)	43.7(7)	3.602(2)	Iron hydride
47.8(1)	47.3(7)	3.562(1)	Iron hydride, diamond
48.4(1)	47.9(2)	3.553(1)	Iron hydride, MgO
49.2(1)	48.5(7)	3.577(4)	Iron hydride
50.5(2)	50.1(8)	3.578 (2)	Iron hydride
50.7(2)	50.2(8)	3.551(3)	Iron hydride
53.1(2)	52.7(2)	3.552(1)	Iron hydride, MgO
55.3(2)	55.1(3)	3.532(2)	Iron hydride, MgO
55.6(2)	55.2(8)	3.533(1)	Iron hydride
60.0(2)	59.7(2)	3.541(1)	Iron hydride, MgO
60.3(3)	60.0(9)	3.554(1)	Iron hydride
60.5(3)	60.0(9)	3.540(2)	Iron hydride
60.6(3)	60.3(9)	3.543(3)	Iron hydride
62.2(3)	62(1)	3.530(4)	Iron hydride
65(1)	64(1)	3.519(4)	Iron hydride
66.2(3)	66 (1)	3.499(1)	Iron hydride, diamond
68.4(3)	68(1)	3.531(4)	Iron hydride, diamond
unknown	82(1)	3.470(5)	Iron hydride

REFERENCES

Adam, J., Green, T., and Sie, S. (1993). Proton microprobe determined partitioning of Rb, Sr, Ba, Y, Nb and Ta between experimentally produced amphiboles and silicate melts with variable F content. *Chemical Geology*, 109(1):29–49.

Ahrens, T. (1989). Water storage in the mantle. *Nature*, 342(1):122–123.

Akahama, Y. and Kawamura, H. (2007). Diamond anvil Raman gauge in multi-megabar pressure range. *High Pressure Research*, 27(4):473–482.

Anderson, O. (2003). *The three-dimensional phase diagram of iron*. American Geophysical Union, Washington, DC.

Anderson, O. and Isaak, D. (2000). Calculated melting curves for phases of iron. *American Mineralogist*, 85(1):376–385.

Anderson, O. and Isaak, D. (2002). Another look at the core density deficit of Earth's outer core. *Physics of the Earth and Planetary Interiors*, 131(1):19–27.

Antonangeli, D., Komabayashi, T., Occelli, F., Borissenko, E., Walters, A., Fiquet, G., and Fei, Y. (2012). Simultaneous sound velocity and density measurements of hcp iron up to 93 GPa and 1100 K: An experimental test of Birch's law at high temperatures. *Earth and Planetary Science Letters*, 331–332(1):210–214.

Antonangeli, D., Morard, G., Schmerr, N., Komayashi, T., Krisch, M., Fiquet, G., and Fei, Y. (2015). Toward a mineral physics reference model for the Moon's core. *Proceedings of the National Academy of Science*, 112(13):3916–3919.

Antonangeli, D. and Ohtani, E. (2015). Sound velocity of *hcp*-Fe at high pressure: Experimental constrains, extrapolations and comparison with seismic models. *Progress in Earth and Planetary Science*, 2(1):3.

Antonov, V., Cornell, K., Fedotov, V., Kolesnikov, A., Ponyatovsky, E., Shiryaev, V., and Wipf, H. (1998). Neutron diffraction investigation of the *dhcp* and *hcp* iron hydrides and deuterides. *Journal of Alloys and Compounds*, 264(1):214–222.

Badding, J., Hemley, R., and Mao, H.-K. (1991). High-pressure chemistry of hydrogen in metals: In situ study of iron hydride. *Science*, 80(253):421–424.

Badro, J., Fiquet, G., Guyot, F., Gregoryanz, E., Occelli, F., Antonangeli, D., and d'Astuto, M. (2007). Effect of light elements on the sound velocities in solid iron: Implications for the composition of Earth's core. *Earth and Planetary Science Letters*, 254(1):233–238.

Baur, W. (1974). The geometry of polyhedral distortions. Predictive relationships for the phosphate group. *Acta Crystallographica Section B*, 30:1195–1215.

Bendeliani, N. A., Baneyeva, M. I., and Poryvkin, D. S. (1972). Synthesis of a new modification of FeO(OH) stable at high pressures. *Geokhimiya*, 7(1):871–873.

Bengtson, A., Li, J., and Morgan, D. (2009). Mössbauer modeling to interpret the spin state of iron in (Mg,Fe)SiO_3 perovskite. *Geokhimiya*, 36(1):L15301.

Bindi, L., Nishi, M., Tsuchiya, J., and Irifune, T. (2014). Crystal chemistry of dense hydrous magnesium silicates: The structure of phase H, $MgSiH_2O_4$, synthesized at 45 GPa and 1000°C. *American Mineralogist*, 99(1):871–873.

Birch, F. (1947). Finite elastic strain of cubic crystals. *Physics Review*, 71(1):809.

Birch, F. (1952). Elasticity and constitution of the Earth's interior. *Journal of Geophysical Research*, 57(1):227–286.

Birch, F. (1978). Finite strain isotherm and velocities for single crystal and polycrystalline NaCl at high-pressures and 300 K. *Journal of Geophysical Research*, 83(1):1257–1268.

Boffa Ballaran, T., Frost, D., Miyajima, N., and Heidelbach, F. (2003). The structure of a super-aluminous version of the dense hydrous-magnesium silicate phase D. *American Mineralogist*, 95(1):1113–1116.

Bolfan-Casanova, N., Keppler, H., and Rubie, D. (2003). Water partitioning at 660 km depth and evidence for very low water solubility in magnesium silicate perovskite. *Geophysical Research Letters*, 30(1):1905.

Bolotina, N., Molchanov, V., Dyuzheva, T., Lityagina, L., and Bendeliani, N. (2008). Single-crystal structures of high-pressure phases FeOOH, FeOOD, and GaOOH. *Chrystallography Reports*, 53(1):960.

Born, M. and Huang, K. (1954). *Dynamical Theory of Crystal Lattices*. Oxford University Press, London, UK.

Campbell, A. (2008). Measurement of temperature distributions across laser-heated samples by multispectral imaging rediometry. *Review of Scientific Instruments*, 79.

Caracas, R. (2015). The influence of hydrogen on the seismic properties of solid iron. *Geophysical Research Letters*, 42.

Catalli, K., Shim, S.-H., Dera, P., Prakapenka, V., Zhao, J., Sturhahn, W., Chow, P., Xiao, Y., Cynn, H., and Evans, W. (2011). Effects of the Fe^{3+} spin transition on the properties of aluminous perovskite—New insights for lower-mantle seismic heterogeneities. *Chrystallography Reports*, 53(1):960.

Chi, H., Dasgupta, R., Duncan, M., and Shimizu, N. (2014). Partitioning of carbon between Fe-rich alloy melt and silicate melt in magma ocean - Implications for the abundance and origin of volatiles in Earth, Mars, and the Moon. *Geochimica et Cosmochimica Acta*, 139(1):447–471.

Cococcioni, M. and de Gironcoli, S. (2005). Linear response approach to the calculation of the effective interaction parameters in the LDA+U method. *Physics Review B*, 71(1):035105.

Dauphas, N., Roskosz, M., Alp, E., Neuville, D., Hu, M., Sio, C., Tissot, F., Zhao, J., Tissandier, L., Mdard, E., and Cordier, C. (2014). Magma redox and structural controls on iron isotope variations in Earth's mantle and crust. *Earth Planetary Science Letters*, 398(1):127–140.

Davies, G. (1995). Penetration of plates and plumes through the mantle transition zone. *Earth Planetary Science Letters*, 133(1):507–516.

Decremps, F., Antonangeli, D., Gauthier, M., Ayrinhac, S., Morard, M., le Marchand, G., Bergame, F., and Philippe, J. (2014). Sound velocity of iron up to 152 GPa by picosecond acoustics in diamond anvil cell. *Physics of the Earth and Planetary Interiors*, 41(1).

Dewaele, A., Loubeyre, P., Occelli, F., Mezouar, M., Dorogokupets, P., and Torrent, M. (2006). Quasihydrostatic equation of state of iron above 2 Mbar. *Physics Review Letters*, 97(1):29–32.

Dziewonski, A. and Anderson, D. (1981). Preliminary reference Earth model. *Physics of the Earth and Planetary Interiors*, 25(1):297–356.

Fischer, R., Nakajima, Y., Campbell, A., Frost, D., Harries, D., Langenhorst, F., Miyajima, N., Pollok, K., and Rubie, D. (2015). High pressure metal–silicate partitioning of Ni, Co, V, Cr, Si, and O. *Geochimica et Cosmochimica Acta*, 167(1):177–194.

Frost, D. (2006). The Stability of Hydrous Mantle Phases. *Reviews in Mineralogy and Geochemistry*, 62(1):243–271.

Frost, D. and Fei, Y. (1998). Stability of phase D at high pressure and high temperature. *Journal of Geophysical Research*, 103(1):7463–7474.

Frost, D. and Fei, Y. (1999). Static compression of the hydrous magnesium silicate phase D to 30 GPa at room temperature. *Physics and Chemistry of Minerals*, 26(5):415–418.

Frost, D., Liebske, C., Langenhorst, F., McCammon, C., Trønnes, R., and Rubie, R. (2004). Experimental evidence for the existence of iron-rich metal in the Earth's lower mantle. *Nature*, 428(1):409–412.

Fukai, Y. (2005). *The Metal–Hydrogen System: Basic Bulk Properties, Second Ed.* Springer, Berlin.

Fukai, Y. and Akimoto, S. (1983). Hydrogen in the Earth's Core. *Proceedings of the Japan Academy*, 59(1):158–162.

Fukai, Y., Mori, K., and Shinomiya, H. (2003). The phase diagram and superabundant vacancy formation in Fe-H allows under high hydrogen pressures. *Journal of Alloys and Compounds*, 348(1):105–109.

Ganero, E. and Helmberger, D. (1996). Seismic detection of a thin laterally varying boundary layer at the base of the mantle beneath the central-Pacific. *Geophysical research Letters*, 23(1):977–980.

Ganero, E. and McNamara, A. (2008). Structure and dynamics of Earth's lower mantle. *Science*, 320(1):626.

Ganero, E., McNamara, A., and Shim, S.-H. (2016). Continent-sized anomalous zones with low seismic velocity at the base of the Earth's mantle. *Nature Geosciencet*, 9(1):481–489.

Giannozzi, P., Baroni, S., Bonini, N., Calandra, M., Car, R., Cavazzoni, C., Ceresoli, D., Chiarotti, G., Cococcioni, M., Dabo, I., Dal Corso, A., de Gironcoli, S., Fabris, S., Fratesi, G., Gebauer, R., Gerstmann, U., Gougoussis, C., Kokalj, A., Lazzeri, M., Martin-Samos, L., Marzari, N., Mauri, F., Mazzarello, R., Paolini, S., Pasquarello, A., Paulatto, L., Sbraccia, C., Scandolo, S., Sclauzero, G., Seitsonen, A., Smogunov, A., Umari, P., and Wentzcovitch, R. (2009). Quantum ESPRESSO: a modular and open-source software project for quantum simulations of materials. *Journal of Physics: Condensed Matter*, 21(1):395502.

Gleason, A., Jeanloz, R., and Kunz, M. (2008). Pressure-temperature stability studies of FeOOH using X-ray diffraction. *American Mineralogist*, 93(1):11–12.

Gleason, A., Quiroga, C., Suzuki, A., Pentcheva, R., and Mao, W. (2013). Symmetrization driven spin transition in ε-FeOOH at high pressure. *Earth and Planetary Science Letters*, 379(1):49–55.

Gu, T., Li, M., McCammon, C., and Lee, K. (2016). Redox-induced lower mantle density contrast and effect on mantle structure and primitive oxygen. *Nature Geoscience*, 9(1):723–728.

Hamann, D. (1997). H_2O hydrogen bonding in density-functional theory. *Physics Review B*, 55(1):R10157.

Hill, R. (1952). The elastic behavior of a crystalline aggregate. *Proceedings of the Physical Society A*, 65(1):349–354.

Hirao, N. (2004). Compression of iron hydride to 80 GPa and hydrogen in the Earth's inner core. *Geophysical Research Letters*, 31(1):L06616.

Hirschmann, M. (2006). Water, Melting, and the Deep Earth H_2O Cycle. *Annual Review of Earth and Planetary Sciences*, 34(1):629–653.

Hirschmann, M. and Kohlstedt, D. (2012). Water in Earth's mantle. *Physics Today*, 65(1):40.

Hsu, H., Umemoto, K., Blaha, P., and Wentzcovich, R. (2010). Spin states and hyperfine interactions of iron in (Mg,Fe)SiO_3 perovskite under pressure. *Physics Review Letters*, 106(1):118501.

Hu, Q., Kim, D., Liu, J., Meng, Y., and Mao, H.-K. (2016). FeO_2 and FeOOH under deep lower-mantle conditions and Earth's oxygen-hydrogen cycles. *Nature*, 534(7):241–245.

Hu, Q., Kim, D., Liu, J., Meng, Y., Yang, L., Zhang, D., Mao, W., and Mao, H.-K. (2017). Dehydrogenation of goethite in Earth's deep lower mantle. *Proceedings of the National Academy*, 114(7):1498–1501.

Hushur, A., Manghnani, M., Smyth, J., Williams, Q., Hellebrand, E., Lonappan, D., Ye, Y., Dera, P., and Frost, D. (2011). Hydrogen bond symmetrization and equation of state of phase D. *Journal of Geophysical Research*, 116(1):B06203.

Ichikawa, I., Tsuchiya, T., and Tange, Y. (2014). The *P-V-T* equation of state and thermodynamic properties of liquid iron. *Journal of Geophysical Research*, 119(1):240–252.

Inoue, T. (1994). Effect of water on melting phase relations and melt composition in the system Mg_2SiO_4-$MgSiO_3$-H_2O up to 15 GPa. *Physics of the Earth and Planetary Interiors*, 85(1):237–263.

Ionov, D. and Hofmann, A. (1995). Nb-Ta-rich mantle amphiboles and micas: implications for subduction-related metasomatic trace element fractionations. *Earth and Planetary Science Letters*, 131(1):341–356.

Iwamori, H. (2004). Phase relations of peridotites under H_2O saturated conditions and ability of subducting plates for transportation of H_2O. *Earth and Planetary Science Letters*, 227(1):57–71.

Jahn, S., Wunder, B., Kock-Müller, M., Tarrieu, L., Pühle, M., Watenphul, A., and Taran, M. (2012). Pressure-induced hydrogen bond symmetrization in guyanaite, β-CrOOH: evidence from spectroscopy and *ab initio* simulations. *European Journal of Mineralogy*, 24(1):839–850.

Jambon, A. and Zimmerman, J. (1990). Water in oceanic basalts: Evidence for dehydration of recycled crust. *Earth and Planetary Science Letters*, 101(1):323–331.

Jang, B., Kim, D., and Shim, J. (1994). Metal-insulator transition and the role of electron correlation in FeO_2. *Physics Review B*, 95(1):075144.

Jeanloz, R. (1979). Properties of iron at high pressures and the state of the core. *Journal of Geophysical Research*, 84(B11):6059–6069.

Jephcoat, A. and Olson, P. (1987). Is the inner Core of the Earth pure iron? *Nature*, 325(1):332–335.

Kagi, H., Ushijima, D., Iizuka, R., Nakano, S., and Nagai, T. (2008). Micro-pellet method for infrared absorption spectroscopy using a diamond anvil cell under a quasi-hydrostatic condition. *High Pressure Research*, 28(3):299–306.

Kanzaki, M. (1991). Stability of hydrous magnesium silicates in the mantle transition zone. *Physics of the Earth and Planetary Science*, 66(1):307–312.

Karato, S. (1990). The role of hydrogen in the electrical conductivity of the upper mantle. *Nature*, 347(1):272–273.

Karato, S., Paterson, M. S., and Fitzgerald, J. D. (1986). Rheology of synthetic olivine aggregates: Influence of grain-size and water. *Journal of Geophysical Research*, 91(1):8151–8176.

Karki, B. B., Stixrude, L., and Wentzcovitch, R. M. (2001). High-pressure elastic properties of major materials of Earth's mantle from first principles. *Reviews of Geophysics*, 39(1):507–534.

Keppler, H., Kantor, I., and Dubrovisnky, L. (2007). Optical absorption spectra of ferropericlase to 84 GPa. *American Mineralogist*, 92(1):433–436.

Komabayashi, T. and Omori, S. (2006). Internally consistent thermodynamic data set for dense hydrous magnesium silicates up to 35GPa, 1600°C: Implications for water circulation in the Earth's deep mantle. *Physics of the Earth and Planetary Interiors*, 156(1):89–107.

Kulik, H., Cococcioni, M., Sherli, D., and Marzari, N. (2006). Density functional theory in transition-metal chemistry: A self-consistent Hubbard U Approach. *Physics and Review Letters*, 97(1):103001.

Kuribayashi, T., Sano-Furukawa, A., and Nagase, T. (2014). Observation of pressure-induced phase transition of δ-AlOOH by using single crystal synchrotron X-ray diffraction method. *Physics and Chemistry of Minerals*, 41(1):303–312.

Kushiro, I. (1987). A petrological model of the mantle wedge and lower crust in the Japanese island arcs. *Magmatic Processes: Physiochemical Principles*, 1(1):165–181.

Lambert, I. and Wyllie, P. (1968). Stability of hornblende and a model for the low velocity zone. *Nature*, 219(1):1240–1241.

LaTourrette, T., Hervig, R., and Holloway, J. (1995). Trace element partitioning between amphibole, phlogopite and basanite melt. *Earth and Planetary Science Letters*, 135(1):13–50.

Lekic, V., Cottaar, S., Dziewonski, A., and Romanowicz, B. (2012). Cluster analysis of global lower mantle tomography: A new class of structure and implications for chemical heterogeneity. *Earth and Planetary Science Letters*, 357–358(1):68–77.

Li, J., Sturhahn, W., Jackson, J., Struzhkin, V., Lin, J., Zhao, J., Mao, H., and Shen, G. (2006). Pressure effect on the electronic structure of iron in (Mg,Fe)(Si,Al)O_3 perovskite: A combined synchrotron Mössbauer and X-ray emission spectroscopy study up to 100 GPa. *Physics and Chemistry of Minerals*, 33(1):575–585.

Li, M., McNamara, A., Ganero, E., and Yu, S. (2017). Compositionally-distinct ultra-low velocity zones in Earth's core-mantle boundary. *Nature Communications*, 8(177).

Lin, J.-F., Struzhkin, V., Jacobsen, S., Hu, M., Chow, P., Kung, J., Liu, H., Mao, H.-K., and Hemley, R. (2005a). Spin transition of iron in magnesiowüstite in the Earth's lower mantle. *Nature*, 436(7049):377–380.

Lin, J.-F., Sturhahn, W., Zhao, J., Shen, G., Mao, H.-K., and Hemley, R. (2005b). Sound velocities of hot dense iron: Birch's Law revisited. *Science*, 308(1):1892–1894.

Litasov, K., Ohtani, E., Nishihara, Y., Suzuki, A., and Funakoshi, K. (2008). Thermal equation of state of Al- and Fe-bearing phase D. *Journal of Geophysical Research*, 113(1):B08205.

Litasov, K., Ohtani, E., Suzuki, A., and Funakoshi, K. (2007). The compressibility of Fe- and Al-bearing phase D to 30 GPa. *Physics and Chemistry of Minerals*, 34(1):159–167.

Liu, J., Hu, Q.and Kim, D., Wu, Z., Wang, W., Xiao, Y., Chow, P., Meng, Y., Prakapenka, V., Mao, H.-K., and Mao, W. (2017). Hydrogen-bearing iron peroxide and the origin of ultralow-velocity zones. *Nature*, 551(1):494–497.

Liu, L. (1987). Effects of H_2O on the phase behavior of the forsterite-enstatite system at high pressures and temperatures and implications for the Earth. *Physics of the Earth and Planetary Interiors*, 49(1):142–167.

Lobanov, S., Zhu, Q., Holtgrewe, N., Prescher, C., Prakapenka, V., Oganov, A., and Goncharov, A. (2015). Stable magnesium peroxide at high pressure. *Scientific Reports*, 5(1):13582.

Mackwell, S. and Kohlstedt, D. (1990). Diffusion of hydrogen in olivine: Implications for water in the mantle. *Journal of Geophysical Research*, 95(1):5079–5088.

Mainprice, D. (1990). An efficient FORTRAN program to calculate seismic anisotropy from the lattice preferred orientation of minerals. *Computational Geoscience*, 41(1):383–393.

Mainprice, D., Hielscher, R., and Schaeben, H. (2011). *Calculating anisotropic physical properties from texture data using MTEX open source package*, volume 360. Geological Society, London.

Mainprice, D., Le Page, Y., Rodgers, J., and Jouanna, P. (2007). Predicted elastic properties of the hydrous D phase at mantle pressures: Implications for the anisotropy of subducted slabs near 670 km discontinuity and in the lower mantle. *Earth and Planetary Science Letters*, 259(1):283–296.

Mao, H.-K., Bell, P., Shaner, J., and Steinberg, D. (1978). Specific volume measurements of Cu, Mo, Pd, and Ag and calibration of the ruby R_1 fluorescence pressure gauge from 0.06 to 1 Mbar. *Journal of Applied Physics*, 49(1):3276.

Mao, H.-K., Shu, J., Shen, G., Hemley, R., Li, B., and Singh, A. (1998). Elasticity and rheology of iron above 220 GPa and the nature of the Earth's iron core. *Nature*, 396(1):741–743.

Mao, H.-K., Xu, J., and Bell, P. (1986). Calibration of the ruby pressure gauge to 800-Kbar under quasi-hydrostatic conditions. *Journal of Geophysical Research*, B91(B5):4673–4676.

Mao, H.-K., Xu, J., Stuzhkin, V., Shu, J., Hemley, R., Sturhahn, W., Hu, M., Alp, E., Vocadlo, L., Alfe, D., Price, G., Gillian, M., Schwoerer-Bhning, Hausermann, D., Eng, P., Shen, G., Giefers, H., Lubbers, R., and Wortmann, G. (2001). Phonon density of states of iron up to 153 gigapascals. *Science*, 292(1):914–916.

Mao, W., Sturhahn, W., Heinz, D., Mao, H.-K., Shu, J., and Hemley, R. (1990). Nuclear resonant X-ray scattering of iron hydride at high pressure. *Geophysical Research Letters*, 31(1):L15618.

Mashino, I., Murakami, M., and Ohtani, E. (2016). Sound velocities of δ-AlOOH up to core-mantle boundary pressures with implications for the seismic anomalies in the deep mantle. *Journal of Geophysical Research: Solid Earth*, 121:595–609.

Matsui, M., Parker, S., and Leslie, M. (2000). The MD simulation of the equation of state of MgO: Application as pressure calibration standard at high temperature and high pressure. *American Mineralogist*, 85(1):312–316.

McGovern, P. and Schubert, G. (1989). Thermal evolution of the Earth: effects of volatile exchange between atmosphere and interior. *Earth and Planetary Science Letters*, 96(1):27–37.

McNamara, A., Ganero, E., and Rost, S. (2010). Tracking deep mantle reservoirs with ultra-low velocity zones. *Earth and Planetary Science Letters*, 299(1):1–9.

Momma, K. and Izumi, F. (2008). VESTA: a three-dimensional visualization system for electronic and structural analysis. *Journal of Applied Crystallography*, 41(1):653–658.

Monkhorst, H. and Pack, J. (1976). Special points for Brillouin-zone integrations. *Physics Review B*, 13(1):5188–5192.

Mysen, B. and Boettcher, A. (1975). Melting of a hydrous mantle: Phase relations of natural peridotite at high pressures and temperatures with controlled activities of water, carbon dioxide, and hydrogen. *Journal of Petrology*, 16(1):520–548.

Narygina, O., Dubrovinsky, L., McCammon, C. A., Kurnosov, A., Kantor, I., Prakapenka, V., and Dubrovinskaia, N. (2011). X-ray diffraction and Mössbauer spectroscopy study of *fcc* iron hydride FeH at high pressures and implications for the composition of the Earth's core. *Earth and Planetary Science Letters*, 307(1):409–414.

Nishi, M., Irifune, T., Gréaux, S., Tange, Y., and Higo, Y. (2015). Phase transitions of serpentine in the lower mantle. *Physics of the Earth and Planetary Interiors*, 245(1):52–58.

Nishi, M., Irifune, T., Tsuchiya, J., Tange, Y., Nishihara, Y., Fujino, K., and Higo, Y. (2014). Stability of hydrous silicate at high pressures and water transport to the deep lower mantle. *Nature Geoscience*, 7(1):224–227.

Nishi, M., Kuwayama, Y., Tsuchiya, J., and Tsuchiya, T. (2017). The pyrite-type high-pressure form of FeOOH. *Nature*, 547(1):205–208.

Novella, D., Jacobsen, B., Weber, P., Tyburczy, J., Ryerson, F., and Du Frane, W. (2017). Hydrogen self-diffusion in single crystal olivine and electrical conductivity of the Earth's mantle. *Scientific Reports*, 7(1):5344.

Ohira, I., Ohtani, E., Sakai, T., Miyahara, M., Hirao, N., Ohishi, Y., and Nishijima, M. (2014). Stability of a hydrous δ-phase, AlOOH-$MgSiO_2(OH)_2$, and a mechanism for water transport into the base of the lower mantle. *Earth and Planetary Science Letters*, 401(1):12–17.

Ohtani, E., Hirao, N., Kondo, T., Ito, M., and Kikegawa, T. (2005). Iron-water reaction at high pressure and temperature, and hydrogen transport into the core. *Physics and Chemistry of Minerals*, 32(1):77–82.

Ohtani, E., Shibazaki, Y., Sakai, T., Mibe, K., Fukui, H., Kamada, S., Sakamaki, T., Seto, Y., Tsutsui, S., and Baron, A. (2013). Sound velocity of hexagonal close-packed iron up to core pressures. *Geophysical Review Letters*, 40(1):5089–5094.

Ohtani, E., Toma, M., Litasov, K., Kubo, T., and Suzuki, A. (2001). Stability of dense hydrous magnesium silicates and water storage capacity in the transition zone and lower mantle. *Physics of the Earth and Planetary Interiors*, 124(1):105–117.

Omori, S., Komabayashi, T., and Maruyama, S. (2004). Dehydration and earthquakes in the subducting slab: empirical link in intermediate and deep seismic zones. *Physics of the Earth and Planetary Interiors*, 146(1):297–311.

Otte, K., Pentcheva, R., Schmahl, W., and Rustad, J. (2009). Pressure-induced structural and electronic transitions in FeOOH from first principles. *Physics Reviews B*, 80(1):1–9.

Pamato, M., Myhill, R., Boffa Ballaran, T., Frost, D., Heidelbach, F., and Miyajima, N. (2015). Lower-mantle water reservoir implied by the extreme stability of a hydrous aluminosilicate. *Nature Geoscience*, 8(1):75–79.

Panero, W. and Caracas, R. (2009). Stability of phase H in the $MgSiO_4H_2$-AlOOH-SiO_2 system. *Earth and Planetary Science Letters*, 463(1):171–177.

Pépin, C., Dewaele, A., and Geneste, G. (2014). New iron hydrides under high pressure. *Physics Review Letters*, 265504(1):1–5.

Perdew, J. P., Burke, K., and Ernzerhof, M. (1996). Generalized gradient approximation made simple. *Physics Review Letters*, 77(1):3865–3868.

Pernet, M., Joubert, J., and Berthet-Colominas, C. (1975). Etude par diffraction neutronique de la forme haute pression de FeOOH. *Solid State Communications*, 17(1):1505–1510.

Pinney, N. and Morgan, D. (2013). *Ab initio* study of structurally bound water at cation vacancy sites in Fe- and Al-oxyhydroxide materials. *Geochimica et Cosmochimica Acta*, 114:94–111.

Poirier, J. P. (1994). Light elements in the Earth's outer core: A critical review. *Physics of the Earth and Planetary Interiors*, 85(1):319–337.

Poli, S. and Schmidt, M. (2002). Petrology of subducted slabs. *Annual Reviews in Earth and Planetary Sciences*, 30(1):207–235.

Prakapenka, V., Kuba, A., Kuznetsov, A., Laskin, A., Shkurikhin, O., Dera, P., Rivers, M., and Sutton, S. (2008). Advanced flat top laser heating system for high pressure research at GSECARS: application to the melting behavior of germanium. *High Pressure Research*, 28(1):225–235.

Prescher, C. and Prakapenka, V. (2015). DIOPTAS: a program for reduction of two-dimensional X-ray diffraction data and data exploration. *High Pressure Research*, 35(1):223–230.

Ringwood, A. (1975). *Composition and Petrology of the Earth's Mantle*. McGraw-Hill, New York.

Rivers, M., Prakapenka, V., Kubo, A., Pullins, C., Holl, C., and Jacobsen, S. (2008). The COMPRES/GSECARS gas-loading system for diamond anvil cells at the Advanced Photon Source. *High Pressure Research*, 28(1):273–292.

Romanowicz, B. and Wenk, H.-R. (2017). Anisotropy in the deep Earth. *Physics of the Earth and Planetary Interiors*, 269:58–90.

Rosa, A., Mezouar, M., Garbarino, G., Bouvier, P., Ghosh, S., Rohrbach, A., and Sanchez-Valle, C. (2013a). Single-crystal equation of state of phase D to lower mantle pressures and the effect of hydration on the buoyancy of deep subducted slabs. *Journal of Geophysical Research: Solid Earth*, 118:6124–6133.

Rosa, A., Sanchez-Valle, C., and Ghosh, S. (2012). Elasticity of phase D and implications for the degree of hydration of deep subducted slabs. *Geophysical research Letters*, 39(6):L06304.

Rosa, A., Sanchez-Valle, C., Nisr, C., Evans, S., Debord, R., and Merkel, S. (2013b). Shear wave anisotropy in textured phase D and constraints on deep water recycling in subduction zones. *Earth and Planetary Science Letters*, 377–378:13–22.

Rüpke, L., Morgan, J., Hort, M., and Connolly, J. (2004). Serpentine and the subduction zone water cycle. *Earth and Planetary Science Letters*, 223(1):17–34.

Sakamaki, K., Takahashi, E., Nakajima, Y., Nishihara, Y., Funakoshi, K., Suzuki, T., and Fukai, Y. (2009). Melting phase relation of FeH_X up to 20 GPa: Implications for the temperature of the Earth's core. *Physics of the Earth and Planetary Interiors*, 174(1):192–201.

Sano, A., Ohtani, E., Kondo, T., Hirao, N., Sakai, T., Sata, N., Ohishi, Y., and Kikegawa, T. (2008). Aluminous hydrous mineral δ-AlOOH as a carrier of hydrogen into the core-mantle boundary. *Geophysical Research Letters*, 35(1):L03303.

Sano-Furukawa, A., Kagi, H., Nagai, T., Nakano, S., Fukura, S., Ushijim, D., Iizuka, E., and Yagi, T. (2009). Change in compressibility of δ-AlOOD and δ-AlOOH at high pressure: A study of isotope effect and hydrogen-bond symmetrization. *American Mineralogist*, 94(1):1255–1261.

Shaw, A. M., Hauri, E., Fischer, T., Hilton, D., and Kelley, K. A. (2008). Hydrogen isotopes in Mariana arc melt inclusions: Implications for subduction dehydration and the deep-Earth water cycle. *Earth and Planetary Science Letters*, 275(1):138–145.

Shibazaki, Y., Ohtani, E., Fukui, H., T., S., Kamasa, S., Ishikaa, D., Tsutsui, S., Baron, A., Nishitani, N., Hirao, N., and Takemura, K. (2012). Sound velocity measurements in *dhcp*-FeH up to 70 GPa with inelastic X-raw scattering: Implications for the composition of the Earth's core. *Earth and Planetary Science Letters*, 313–314(1):79–85.

Shieh, S., Mao, H.-K., Hemley, R., and Ming, L. (1998). Decomposition of phase D in the lower mantle and the fate of dense hydrous silicates in subducting slabs. *Earth and Planetary Science Letters*, 159(1):13–23.

Shinmei, T., Irifune, T., Tsuchiya, J., and Funakoshi, K.-I. (2008). Phase transition and compression behavior of phase Dup to 46 GPa using multi-anvil apparatus with sintered diamond anvils. *High Pressure Research*, 28(3):13–23.

Smith, E., Shirey, S., Nestola, F., Bullock, E., Wang, J., Richardson, S., and Wang, W. (2016). Large gem diamonds from metallic liquid in Earth's deep mantle. *Science*, 354(6318):1403–1405.

Smyth, R. (2006). Hydrogen in High Pressure Silicate and Oxide Mineral Structures. *Reviews in Mineralogy and Geochemistry*, 62(1):85–115.

Speziale, S., Milner, A., Lee, V., Clark, S., Pasternak, M., and Jeanloz, R. (2005). Iron spin transition in Earth's mantle. *Proceedings of the National Academy of Science*, 102(50):17918–17922.

Stern, R. (2002). Subduction zones. *Reviews of Geophysics*, 40(1):1012.

Stevenson, D. (1977). Hydrogen in the Earth's core. *Science*, 268(1):130–131.

Stevenson, D. (1981). Models of the Earth's core. *Science*, 214(1):611–619.

Stixrude, L., Wasserman, E., and Cohen, R. (1997). Composition and temperature of the Earth's inner core. *Journal of Geophysical Research*, 102(1):4729–4739.

Sturhahn, W. (2000). CONUSS and PHOENIX: Evaluation of nuclear resonant scattering data. *Journal of Physics: Condensed Matter*, 16(1):149–172.

Suzuki, A. (2010). High-pressure X-ray diffraction study of ε-FeOOH. *Physics and Chemistry of Minerals*, 37(1):153–157.

Suzuki, A. (2016). Pressure-volume-temperature equation of state of ε-FeOOH to 11 GPa and 700 K. *Journal of Mineralogical and Petrological Sciences*, 111(1):420–424.

Tatsumi, Y., Hamilton, D., and Nesbitt, R. (1986). Chemical characteristics of fluid phase released from a subducted lithosphere and origin of arc magmas: evidence from high pressure experiments and natural rocks. *Volcanology and Geothermal Research*, 29(1):293–310.

Thompson, E., Campbell, A., and Tsuchiya, J. (2017). Elasticity of ε-FeOOH: Seismic implications for Earth's lower mantle. *Journal of Geophysical Research Solid Earth*, 122(7):5038–5047.

Thompson, E., Campbell, A., and Zhenxian, L. (2016a). In-situ infrared spectroscopic studies of hydroxyl in amphiboles at high pressure. *American Mineralogist*, 101:706–712.

Thompson, E., Chidester, B., Fischer, R., Myers, G., Heinz, D., Prakapenka, V., and Campbell, A. (2016b). Equation of state of pyrite to 80 GPa and 2400 K. *American Mineralogist*, 101:1046–1051.

Thompson, E., Davis, A., Bi, W., Zhao, J., Alp, E., Zhang, D., Greenberg, E., Prakapenka, V., and Campbell, A. (2018). High-pressure geophysical properties of *fcc* phase FeH_X. *Geochemistry, Geophysics, and Geosystems*, 19(1):305–314.

Thompson, P. and Tackley, P. (1998). Generation of mega-plumes from the core-mantle boundary in compressible mantle with temperature-dependent viscosity. *Geophysical Research Letters*, 25(1):1999–2002.

Thorne, M. and Ganero, E. (2004). Inferences on ultralow-velocity zone structure from a global analysis of *SPdKS* waves. *Journal of Geophysical Research*, 109:2156–2202.

Tiepolo, M., Vannucci, R., Oberti, R., Foley, S., Bottazzi, P., and Zanetti, A. (2000). Nb and Ta incorportation and fractionation in titanian pargasite and kaersutite: crystal-chemical constraints and implications for natural systems. *Science*, 176(1):185–201.

Troullier, N. and Martins, J. (1991). Efficient pseudopotential for planewave calculations. *Physics Review B*, 43(1):1993–2006.

Tsuchiya, J. (2013). First principles prediction of a new high-pressure phase of dense hydrous magnesium silicates in the lower mantle. *Geophysical Research Letters*, 40(1).

Tsuchiya, J. and Mookherjee, M. (2015). Crystal structure, equation of state, and elasticity of phase H ($MgSiO_4H_2$) at Earth's lower mantle pressures. *Scientific Reports*, 5(1):15534.

Tsuchiya, J. and Tsuchiya, T. (2009). Elastic properties of δ-AlOOH under pressure: First principles investigation. *Physics of the Earth and Planetary Materials*, 174(1):122–127.

Tsuchiya, J. and Tsuchiya, T. (2011). First principles prediction of a high-pressure hydrous phase of AlOOH. *Physics Review B*, 83(1):054115.

Tsuchiya, J., Tsuchiya, T., and Tsuneyuki, S. (2005). First-principles study of hydrogen bond symmetrization of phase D under high pressure. *American Mineralogist*, 90(1):44–49.

Tsuchiya, J., Tsuchiya, T., Tsuneyuki, S., and Yamanaka, T. (2002). First principles calculation of a high-pressure hydrous phase δ-AlOOH. *Geophysics Research Letters*, 19(1):1909.

Tsuchiya, J., Tsuchiya, T., and Wentzcovitch, R. (2008). Vibrational properties of δ-AlOOH under pressure. *American Mineralogist*, 93(1):477–482.

Tsuchiya, T., Wentzcovitch, R., da Silva, C., and de Gironcoli, S. (2006). Spin transition in magnesiowüstite in Earth's lower mantle. *Physics Review Letters*, 96(1):198501.

Tsujino, N., Nishihara, Y., Nakajima, Y., Takahashi, E., Funakoshi, K., and Higo, Y. (2013). Equation of state of γ-Fe: Reference density for planetary cores. *Earth and Planetary Science Letters*, 375(1):244–253.

Tsumuraya, T., Matsuura, Y., Shishidou, T., and Oguchi, T. (2012). First-principles study on the structural and magnetic properties of iron hydride. *Journal of the Physical Society of Japan*, 81(1):064707.

Ulmer, P. (2001). Partial melting in the mantle wedge–the role of H_2O in the genesis of mantle-derived 'arc- related' magmas. *Physics of the Earth and Planetary Interiors*, 127(1):215–232.

Umemoto, K. and Hirose, K. (2015). Liquid iron-hydrogen alloys at outer core conditions by first-principles calculations. *Geophysical Research Letters*, 325(1):332–335.

Umemoto, K. and Wentzcovitch, R. (1991). Theoretical study of the isostructural transformation in ice VIII. *Physics Review B*, 43(1):1993–2006.

van der Hilst, R. D., Widiyantoro, S., and Engdahl, E. R. (1997). Evidence for deep mantle circulation from global tomography. *Nature*, 386(1):578–584.

Vanderbilt, D. (1990). Soft self-consistent pseudopotentials in a generalized eigenvalue formalism. *Physics Review B*, 41(1):7892–7895.

Wang, D., Mookherjee, M., Xu, Y., and Karato, S. (1991). The effect of water on the electrical conductivity of olivine. *Nature*, 443(26):977–980.

Wentzcovitch, R. (1991). Invariant molecular dynamics approach to structural phase transitions. *Physics Review B*, 44(1):2358–2362.

Wentzcovitch, R., Karki, B., Cococcioni, M., and de Gironcoli, S. (1996). Thermoelastic properties of $MgSiO_3$-perovskite: Insights on the nature of the Earth's lower mantle. *Physical Review Letters*, 92(1):018501–018504.

Williams, Q. and Garnero, E. (1996). Seismic evidence for partial melt at the base of Earth's mantle. *Science*, 273(1):1528–1530.

Williams, Q. and Hemley, R. (2001). Hydrogen in the deep Earth. *Annual Review of Earth and Planetary Science*, 29(1):365–418.

Xu, W., Greenberg, E., Rozenberg, G., Pasternak, M., Bykova, E., Boffa-Ballaran, T., Dubrovinsky, L., Prakapenka, V., Hanfland, M., Vekilova, O., Simak, S., and Abrikosov, I. (2013). Pressure-induced hydrogen bond symmetrization in iron oxyhydroxide. *Physical Review Letters*, 111(17):1–5.

Yagi, T. and Hishinuma, T. (1995). Iron hydride formed by the reaction of iron, silicate, and water: Implications for the light element of the Earth's core. *Geophysical Research Letters*, 22(14):1933–1936.

Yang, H., Prewitt, C., and Frost, D. (1997). Crystal structure of the dense hydrous magnesium silicate, phase D. *American Mineralogist*, 82(1):651–654.

Yu, S. and Ganero, E. (2018). Ultralow velocity zone locations: A global assessment. *Geochemistry, Geophysics, Geosystems*, 19(2):396–414.

Yuan, L., Ohtani, E., Ikuta, D., Kamada, S., Tsuchiya, J., Naohisa, H., Ohishi, Y., and Suzuki, A. (2018a). Chemical reactions between Fe and H_2O up to megabar pressures and implications for water storage in Earth's mantle and core. *Geophysical Research Letters*, 45:1330–1338.

Yuan, L., Ohtani, E., Ikuta, D., Kamada, S., Tsuchya, J., Naohisa, H., Ohishi, Y., and Suzuki, A. (2018b). Chemical reactions between fe and H_2O up to megabar pressures and implications for water storage in the Earth's mantle and core. *Geophysical Research Letters*, 45:1330–1338.

Zeng, Z., Yang, L., Zeng, Q., Lou, H., Sheng, H., Wen, J., Miller, D., Meng, Y., Yang, W., Mao, W., and Mao, H.-K. (2017). Synthesis of quenchable amorphous diamond. *Nature Communications*, 8:322.

Zhang, Z., Dorfman, S., Labidi, J., Zhang, S., Li, M., Manga, M., Stixrude, L., McDonough, W., , and Williams, Q. (2016). Primordial metallic melt in the deep mantle. *Geophysical Research Letters*, 43(1):3693–3699.